

# Toward a systematic discovery of artificial functional ferromagnets and their applications

Von der Fakultät für Physik und Geowissenschaften

der Universität Leipzig

genehmigte

DISSERTATION

zur Erlangung des akademischen Grades

*Doctor rerum naturalium*

*Dr. rer. nat.*

vorgelegt

von M. Sc. Lukas Botsch

geboren am 02.04.1988 in Freiburg i. Br.

Gutachter Prof. Dr. Pablo D. Esquinazi  
Prof. Dr. Carsten Ronning

Tag der Verleihung 19.07.2021



# Selbständigkeitserklärung

Hiermit versichere ich,

- dass die vorliegende Arbeit ohne unzulässige Hilfe und ohne Benutzung anderer als der angegebenen Hilfsmittel angefertigt wurde, und dass die aus fremden Quellen direkt oder indirekt übernommenen Gedanken in der Arbeit als solche kenntlich gemacht wurden;
- dass alle Personen in der Dissertation genannt wurden, von denen ich bei der Auswahl und Auswertung des Materials sowie bei der Herstellung des Manuskripts Unterstützungsleistung erhalten habe;
- dass die vorgelegte Arbeit weder im Inland noch im Ausland in gleicher oder inähnlicher Form einer anderen Prüfungsbehörde zum Zwecke einer Promotion oder eines anderen Prüfungsverfahrens vorgelegt und in ihrer Gesamtheit noch nicht veröffentlicht wurde;
- dass keine früheren erfolglosen Promotionsversuche stattgefunden haben;
- dass keine weiteren Personen bei der geistigen Herstellung der vorliegenden Arbeit beteiligt waren;
- dass dritte Personen weder unmittelbar noch mittelbar geldwerte Leistungen für Arbeiten erhielten, die im Zusammenhang mit dem Inhalt der vorgelegten Dissertation stehen;

Mit meiner Unterschrift erkläre ich, dass ich die Promotionsordnung der Fakultät für Physik und Geowissenschaften der Universität Leipzig, in der Fassung vom 24. August 2016, und die obengenannte Selbständigkeitserklärung anerkenne.

Datum:

---

Unterschrift:

---





# Bibliographic Data:

Botsch, Lukas

Toward a systematic discovery of artificial functional ferromagnets and their applications

Universität Leipzig, Dissertation

147+xx p., 145 ref., 60 fig., 7 tab.

## Abstract:

Although ferromagnets are found in all kinds of technological applications, their natural occurrence is rather unusual because only few substances are known to be intrinsically ferromagnetic at room temperature. In the past twenty years, a plethora of new artificial ferromagnetic materials has been found by introducing defects into non-magnetic host materials. In contrast to the intrinsic ferromagnetic materials, they offer an outstanding degree of material engineering freedom, provided one finds a type of defect to functionalize every possible host material to add magnetism to its intrinsic properties. Still, some controversial questions remain: What are the mechanisms behind these ferromagnetic materials? Why are their magnetization values reported in the literature so low? Are these materials really technologically relevant ferromagnets?

In this work, we aim to provide a systematic investigation of the phenomenon. We propose a universal scheme for the computational discovery of new artificial functional magnetic materials, which is guided by experimental constraints and based on first principles. The obtained predictions explain very well the experimental data found in the literature. The potential of the method is further demonstrated by the experimental realization of a truly 2D ferromagnetic phase at room temperature, created in nominally non-magnetic  $\text{TiO}_2$  films by ion irradiation, which follows a characteristic 2D magnetic percolation transition and exhibits a tunable magnetic anisotropy.

Furthermore, the technological relevance of these artificial ferromagnetic materials, which comes to shine when one combines the engineered magnetic with some of the intrinsic properties of the host material, is demonstrated by creating a spin filter device in a ZnO host that generates highly spin-polarized currents even at room temperature.



# Bibliographische Beschreibung:

Botsch, Lukas

Toward a systematic discovery of artificial functional ferromagnets and their applications

Universität Leipzig, Dissertation

147+xx S., 145 Lit., 60 Abb., 7 Tab.

## Referat:

Obwohl Ferromagnete in allen möglichen technischen Anwendungen zu finden sind, ist ihr natürliches Vorkommen eher ungewöhnlich, da nur wenige Stoffe bekannt sind, die bei Raumtemperatur intrinsisch ferromagnetisch sind. In den letzten zwanzig Jahren wurde eine Fülle neuer künstlicher ferromagnetischer Materialien durch das Einbringen von Defekten in nichtmagnetische Wirtsmaterialien entdeckt. Im Gegensatz zu den intrinsischen ferromagnetischen Materialien bieten sie einen herausragenden Grad an materialtechnischer Freiheit, vorausgesetzt man findet zu jedem möglichen Wirtsmaterial einen passenden Typus von Defekten, um dessen intrinsische Eigenschaften um Magnetismus zu ergänzen. Dennoch bleiben einige kontroverse Fragen bislang unbeantwortet: Welche Mechanismen stehen hinter diesen ferromagnetischen Materialien? Warum werden ihre Magnetisierungswerte in der Literatur meist so niedrig angegeben? Sind diese Materialien wirklich technologisch relevante Ferromagneten?

In dieser Arbeit wollen wir eine systematische Untersuchung des Phänomens durchführen. Wir schlagen ein universelles ab-initio Protokoll für die computergestützte Entdeckung von neuen künstlichen funktionalen magnetischen Materialien vor, das sich an experimentellen Bedingungen orientiert. Die erhaltenen Vorhersagen erklären die in der Literatur gefundenen experimentellen Daten sehr gut. Wir demonstrieren die Wirksamkeit der Methode durch die experimentelle Realisierung einer echten 2D-ferromagnetischen Phase bei Raumtemperatur, die in nominell nicht-magnetischen  $\text{TiO}_2$ -Filmen durch Ionenbestrahlung erzeugt wird. Die so entstehende ferromagnetische Phase folgt einem charakteristischen zweidimensionalen magnetischen Perkulationsprozess und weist eine steuerbare magnetische Anisotropie auf.

Weiterhin wird die technologische Relevanz dieser künstlichen ferromagnetischen Materialien gezeigt, welche besonders zum Vorschein kommt, wenn man die künstlichen magnetischen mit einigen der intrinsischen Eigenschaften des Wirtsmaterials kombiniert, und zwar indem ein Spin-Filter Element auf Basis eines  $\text{ZnO}$ -Wirts gebaut wird, das selbst bei Raumtemperatur hoch spin-polarisierte Ströme erzeugt.



## Acknowledgements

First, I would like to thank my supervisor, Prof. Dr. Pablo D. Esquinazi, for giving me the opportunity to conduct the research that led to this thesis, for his guidance and motivation.

I am very grateful to my family, who always supported and encouraged me and gave me the strength to complete this great task.

Further, I would like to especially thank and acknowledge:

- Dr. Israel Lorite and Dr. Yogesh Kumar for guiding me on my very first steps as an experimental physicist, for the great discussions and their friendship.
- Dr. Bogdan Semenenko and Christian Precker, with whom I shared an office and had a great time. They both helped me out in the daily lab work more times than I can count and were always there to refill on coffee when it got late.
- Dr. Séverine Diziain, with whom I had the pleasure to work with, who taught me more than she might realize and who gave me the great opportunity to refresh my French.
- Annette Setzer for fruitful discussions and her help with the SQUID magnetometers I used over the years.
- Prof. Dr. Michael Ziese for fruitful discussions on magnetism and his direct and constructive criticism.
- Prof. Dr. Wolfram Hergert, Dr. Waheed Adeagbo and Hichem Ben Hamed for fruitful collaboration and discussions on computational methods.
- Dr. Daniel Spemann and Dr. Carsten Bundesmann for the fruitful collaboration and for providing me with the TiO<sub>2</sub> thin film samples.
- Dr. Rüdiger Schmidt-Grund and Dr. Tom Michalsky for discussions and help on the ZnO photoluminescence measurements
- All the students I had the pleasure to work with in the SUM group at Leipzig University and had the opportunity to help as a supervisor.
- Sandy Ehlers for her support in all bureaucratic matters.
- The Deutsche Forschungsgemeinschaft (DFG) for providing funding for part of this research under the Collaborative Research Center (SFB762) "Functionality of Oxide Interfaces".
- The Leipzig University Computing Center for providing me access to the computational resources on which part of this work was performed.



# Contents

<b>Selbständigkeitserklärung</b>	<b>iii</b>
<b>Abstract</b>	<b>v</b>
<b>Zusammenfassung</b>	<b>vii</b>
<b>Acknowledgements</b>	<b>ix</b>
<b>Contents</b>	<b>xi</b>
<b>List of Figures</b>	<b>xiii</b>
<b>List of Tables</b>	<b>xv</b>
<b>Glossary</b>	<b>xvii</b>
<b>1 Introduction</b>	<b>1</b>
<b>2 Computational discovery of artificial ferromagnets</b>	<b>5</b>
2.1 Ferromagnetism in solids . . . . .	6
2.1.1 Exchange interaction and magnetic order . . . . .	6
2.1.2 Artificial magnetism due to defects . . . . .	10
2.2 Predicting defect structures from collision cascades . . . . .	13
2.3 Finding magnetic defect candidates . . . . .	15
2.4 Magnetic percolation . . . . .	18
2.5 Magnetic phase diagram of anatase TiO <sub>2</sub> artificial ferromagnet	22
2.5.1 Defect creation in anatase TiO <sub>2</sub> . . . . .	22
2.5.2 Magnetic properties of dFP defects in anatase TiO <sub>2</sub> . . . . .	23
2.5.3 Constructing a magnetic phase diagram . . . . .	28
2.6 Revisiting prior experimental results . . . . .	32
<b>3 Artificial ferromagnetism in TiO<sub>2</sub> hosts</b>	<b>37</b>
3.1 Low energy ion irradiation . . . . .	39
3.2 SQUID magnetometry . . . . .	47
3.3 Experimental realization of an artificial ferromagnet in TiO <sub>2</sub>	57
<b>4 Artificial magnetic monolayers and surface effects</b>	<b>69</b>
4.1 Critical behavior and 2D magnetism . . . . .	70
4.2 Magnetic anisotropy . . . . .	75
4.2.1 Demagnetizing field and magnetic shape anisotropy	75
4.2.2 Magnetocrystalline anisotropy . . . . .	77
4.3 Artificial ferromagnetic monolayer at TiO <sub>2</sub> surface with per-	
pendicular magnetic anisotropy . . . . .	78
4.4 DFT calculations of the defective anatase TiO <sub>2</sub> [001] surface .	81

<b>5 Spin transport through artificial ferromagnet interfaces</b>	<b>85</b>
5.1 Artificial ferromagnetism in ZnO hosts . . . . .	87
5.2 Spin filter effect at magnetic/non-magnetic interfaces in ZnO	90
5.2.1 The spin filter effect . . . . .	90
5.2.2 Lithium and hydrogen doping in ZnO . . . . .	91
5.2.3 Magneto-transport in artificial ferromagnetic Li:ZnO microwires . . . . .	98
5.2.4 Spin transport through magnetic/non-magnetic inter- faces . . . . .	98
5.2.5 Minority spin filter effect . . . . .	107
<b>6 Conclusions and Outlook</b>	<b>115</b>
<b>Bibliography</b>	<b>119</b>
<b>A List of publications</b>	<b>131</b>
<b>B Computation inputs and codes</b>	<b>133</b>
B.1 DFT electronic structure calculations - Fleur input files . . . .	134
B.2 Magnetic Percolation simulations . . . . .	145
B.3 SQUID raw data analysis code . . . . .	146
B.4 SRIM Monte Carlo binary collision code automation . . . . .	147



# List of Figures

2.1	Sketch of the H <sub>2</sub> molecule position vectors . . . . .	6
2.2	Computational scheme for the discovery of artificial ferromagnets . . . . .	11
2.3	Magnetic percolation model . . . . .	19
2.4	Sketch of the dFP defect in TiO <sub>2</sub> . . . . .	23
2.5	Defect probabilities in TiO <sub>2</sub> from MD simulations . . . . .	24
2.6	Muffin-tin decomposition . . . . .	25
2.7	Magnetization of the dFP defect supercell . . . . .	27
2.8	Magnetization in the XZ-plane through the Ti interstitials . . . . .	28
2.9	Anatase TiO <sub>2</sub> with dFP DOS . . . . .	29
2.10	Magnetic phase diagram of TiO <sub>2</sub> . . . . .	30
2.11	Magnetization measurements in SiC and CeO <sub>2</sub> . . . . .	33
2.12	Magnetic phase diagram of defective SiC . . . . .	34
3.1	Sketch of the irradiation setup . . . . .	39
3.2	Plasma ion density simulation . . . . .	41
3.3	Plasma electric potential simulation . . . . .	42
3.4	Simulated ion trajectories . . . . .	43
3.5	Ion energy distribution function at 300 V . . . . .	44
3.6	Ion energy distribution function at 500 V . . . . .	45
3.7	Ion energy distribution function at 1000 V . . . . .	46
3.8	Sketch of MPMS SQUID detection system . . . . .	47
3.9	Sketch of the SQUID sample holder . . . . .	49
3.10	Raw SQUID voltage measurements . . . . .	50
3.11	Sample geometry corrections to the SQUID voltage fitting procedure . . . . .	52
3.12	Coordinate system for geometry correction factor calculation . . . . .	53
3.13	Finite sample size effect on the magnetic flux through pickup coils . . . . .	55
3.14	Magnetization reset sequence . . . . .	58
3.15	Magnetic hysteresis loops of TiO <sub>2</sub> artificial ferromagnet . . . . .	59
3.16	Temperature dependence of the TiO <sub>2</sub> magnetic moment . . . . .	60
3.17	Evolution of isolated paramagnetic defects . . . . .	62
3.18	Ferromagnetic hysteresis parameters . . . . .	63
3.19	Experimental observation of magnetic percolation . . . . .	64
3.20	Magnetic percolation in CeO <sub>2</sub> and SiC . . . . .	65
4.1	Critical behavior of the emerging artificial FM phase in TiO <sub>2</sub> . . . . .	73
4.2	Critical behavior of the emerging artificial FM phase in CeO <sub>2</sub> . . . . .	74
4.3	Magnetization loops showing magnetic anisotropy . . . . .	79
4.4	Magnetic anisotropy energy as a function of irradiation fluence . . . . .	80
4.5	Surface spin density . . . . .	82
4.6	Surface density of states . . . . .	83

5.1	Tunneling spin filter . . . . .	90
5.2	N-P-N Diode Current-Voltage characteristics . . . . .	92
5.3	$H(I)/n$ plot to determine potential barrier as a function of temperature . . . . .	95
5.4	$H(I)/n$ plot to determine potential barrier as a function of applied magnetic field . . . . .	95
5.5	Series resistance as a function of temperature . . . . .	96
5.6	Photoluminescence spectra of $H^+$ -implanted Li:ZnO . . . . .	97
5.7	Photoluminescence map of magnetic interfaces along ZnO microwire . . . . .	98
5.8	Magnetoresistance of magnetic ZnO . . . . .	99
5.9	Sketch of masked ZnO mirowire . . . . .	100
5.10	Magnetoresistance of Li:ZnO microwire spin filter . . . . .	101
5.11	Spin-filter magnetoresistance as a function of temperature . . . . .	102
5.12	Spin-filter magnetoresistance at different ion fluences and number of junctions . . . . .	103
5.13	Spin-filter magnetoresistance as a function of bias voltage . . . . .	104
5.14	Spin-filter magnetoresistance as a function of temperature at different bias voltages . . . . .	105
5.15	Spin-filter magnetoresistance at reversed bias voltage polarity . . . . .	106
5.16	Potential barrier height as a function of temperature . . . . .	107
5.17	Potential barrier height as a function of applied magnetic field . . . . .	108
5.18	Sketch of the energy landscape of the spin-filtering potential barrier . . . . .	108
5.19	Weight of the spin-splitting energy $E_s$ as a function of temperature . . . . .	110
5.20	Spin polarization $\alpha$ on the magnetic side of the spin-filter . . . . .	111
5.21	Minority spin depopulation due to an applied magnetic field as a function of temperature . . . . .	112
5.22	Spin filter efficiency $P_{sf}$ . . . . .	112

# List of Tables

2.1	Critical exponent $\beta$ of the magnetic percolation transition. . . . .	20
3.1	Finite sample size SQUID correction factors . . . . .	56
3.2	Ion irradiation parameters . . . . .	57
3.3	Magnetization of artificial ferromagnets . . . . .	66
4.1	Experimental percolation parameters . . . . .	71
4.2	Contributions to the magnetic anisotropy energy . . . . .	84
5.1	Spin filter efficiencies measured in tunnel junctions made of different oxide tunneling barriers. . . . .	91



# Glossary

- dFP** di-Frenkel Pair 18, 19, 23, 25–31, 64, 66, 70, 77, 80–83
- DFT** Density Functional Theory 2, 12, 15, 16, 25, 28, 31, 33, 72, 77, 81, 82, 87, 88, 117
- DOS** density of states 27, 29, 83
- FLAPW** Full-potential Linearized Augmented Planewave 16, 25, 80–82, 88, 89
- FM** ferromagnetic 2, 11, 23, 30, 31, 34, 38, 64, 66, 67, 70, 74, 78, 80, 84, 108, 109, 113
- KS** Kohn-Sham 16, 27, 77, 81
- MAE** Magnetic Anisotropy Energy 75–78, 80, 81, 84
- MC** Monte Carlo 12–14, 28, 29
- MCA** Magnetocrystalline Anisotropy 75, 77, 78, 83, 84
- MD** Molecular Dynamics 12, 13, 15, 16, 22–24, 28, 29, 33, 35, 116
- NM** non-magnetic 90, 108, 109, 113
- PKA** primary knock-on atom 13, 14, 22–24, 28, 29, 35
- SOI** Spin-Orbit Interaction 77, 83
- XMCD** X-ray magnetic circular dichroism 3, 33, 89, 98



*To Zoe*





# Chapter 1

## Introduction

Magnetic materials play a major role in many spintronic and other technological applications [1], such as magnetic storage [2], logic devices [3], magnetic field sensors, and magnetic random access memory [4–6]. Materials with strong intrinsic ferromagnetic (FM) order above room temperature, such as the transition metals Fe, Ni or Co and their alloys, are rather unusual among the magnetic materials known today and there is still the need for new functional materials with magnetic order above room temperature. In the past two decades, a method of creating artificial ferromagnetic materials has emerged and a multitude of so-called defect-induced ferromagnets was reported [7–9].

Since the first prediction of an artificial ferromagnetic material with transition temperature above 300 K, based on Mn-doped ZnO appeared twenty years ago [10], the field has substantially evolved. First, it was realized that doping with magnetic impurities, such as Mn, was not at all necessary in order to induce a robust FM order in the non-magnetic host matrix, rather all kinds of lattice defects were at the origin of the measured magnetic signals [11–14]. This realization promised great possibilities to construct new functional magnetic materials, as any non-magnetic material could potentially host a certain kind of defect, turning it into an artificial ferromagnet. The hunt was on and the result was a plethora of reports ranging from oxide, nitride, carbon-based, 2D van der Waals and many more materials showing signals of ferromagnetism upon introducing all kinds of nominally non-magnetic defects [7–9]. One of the most promising and versatile methods for introducing these defects is the irradiation with non-magnetic ions [15], owing to the availability of ion sources ranging over the whole periodic table and energies from a few eV to hundreds of MeV.

Although many experiments were accompanied by theoretical studies, such as electronic structure calculations based on Density Functional Theory (DFT), the search was mostly guided by blind trial and error and a brute force approach. It is therefore not very surprising that most of the reported materials only showed very tiny magnetic signals, which soon led to debates about the nature of the effect [16, 17] and raised the question of whether this route could eventually lead to a robust magnetic order above room temperature, comparable with intrinsic ferromagnets. Furthermore, the measurement of the magnetization of such artificial ferromagnetic samples turns out to be quite difficult due to the inherent uncertainty of the magnetic volume, leading to largely underestimated values in the literature. Considering the enormous amount of host material candidates and lattice defects, a more systematic search method and better selection criteria are highly needed.

On the experimental side, an enormous amount of research effort has been dedicated to finding new artificial ferromagnets, understanding the origin of and improving the measurement sensitivity of their mostly tiny magnetic signals. The seminal paper by Dietl et al. [10] alone has almost 7000 citations and is still referred to on a regular basis today. Most of these experimental reports show magnetization loops, usually measured using SQUID magnetometry, appearing in various samples upon changing the growth conditions, such as background gas pressure during oxide thin film growth [12] or doping with non-magnetic elements [18–24], post-growth annealing [25] or particle irradiation [15, 26–31]. Relating the emerging artificial ferromagnetic phase and its evolution to the creation of certain defects

remains quite difficult. Element specific methods such as X-ray magnetic circular dichroism (XMCD) have proven very useful to identify potential defect candidates experimentally [16, 32–35]. But systematic investigations of the emerging ferromagnetic phase and its evolution depending on the actual defect concentrations in the samples are not commonly performed.

The most direct method allowing to control the creation of certain defects in a host material uses particle irradiation techniques [15]. By irradiating samples with, e.g., energetic ions, it is possible to control the amount and position of defects created within the host material. One sample can be irradiated multiple times, allowing to measure its magnetic properties as a function of the total irradiation fluence [28, 29]. If one can relate the amount of certain defects created during the irradiation to the ion fluence, the evolution of the artificial ferromagnetic phase can be observed in a systematic way. This requires a good understanding of the defect creation processes and methods to calculate the creation probabilities, that can vary depending on experimental conditions.

The potential to turn any non-magnetic host material into an artificial ferromagnet by introducing a certain kind of defect in a controlled way is not only interesting from a fundamental physics perspective. For technological applications, it presents a powerful material engineering tool, whose value has been recognized early on in the development of the field [36, 37]. The vision of spintronic applications, which aim to use the spin degree of freedom of electrons to enhance conventional electronics or develop completely new devices has pushed the field of artificial ferromagnetism, but it appears that we are just starting to see its full potential: Combining intrinsic properties of the host with the emerging magnetic properties of the artificial ferromagnet could be a driver for new technologies. In recent years, the spin properties of some of the defects have gained major interest in their isolated paramagnetic state, due to their potential use as quantum bits able to operate at room temperature and their favorable optical properties, allowing coherent control over the spin states and their use as exceptionally precise quantum sensors. The most famous examples are the NV center in diamond and the di-vacancy in SiC. The coupling of these isolated quantum systems to their environment and between each other through, e.g., magnetic interactions could be key to the development of quantum information technology.

This work treats the specific set of artificial ferromagnetic materials, that can be created in a controlled way by introducing certain defects in non-magnetic host materials using ion irradiation techniques. We first aim to understand the fundamental physical processes involved in the emergence of an artificial ferromagnetic phase due to the creation of certain defects. In Chapter 2, we introduce the physical principles underlying the emerging magnetically ordered phase, discuss theoretical models and computational methods that can explain and predict these materials and propose a scheme for the efficient discovery of artificial ferromagnetic materials that can be realized experimentally by ion irradiation. To test the power of the developed methods, the predictions of this scheme are used to interpret systematic measurements of the magnetic properties of prototypical artificial ferromagnets as a function of ion fluence reported in the literature, proving an accurate description of the defect creation processes. We apply the predictive scheme to find experimental parameters for the realization

of a robust artificial ferromagnetic phase in a non-magnetic semiconducting host material,  $\text{TiO}_2$ , by low energy ion irradiation.

In Chapter 3, we describe the experimental methods used to realize and observe the emerging ferromagnetic phase in  $\text{TiO}_2$  thin film hosts. Its magnetic properties are investigated in a systematic way as a function of the irradiation fluence and ion energy and compared to the computational predictions. Depending on the irradiation energy and fluence, the thickness of the emerging ordered phase varies from a few layers of the host lattice down to the monolayer limit. In Chapter 4, we investigate the implications of the reduced dimensionality, discuss the emergence of a 2D artificial ferromagnetic phase and the role of the sample surface in its stability. The concepts of magnetic anisotropy are introduced theoretically and its role is shown experimentally in the artificial ferromagnetic  $\text{TiO}_2$  samples.

Finally, in Chapter 5, we take a look at another prominent artificial ferromagnetic system realized experimentally in  $\text{ZnO}$  hosts. Combining the electrical properties of the host system and the spin properties of the emerging ordered phase, we create an efficient spin filter device that operates at room temperature and generates spin-polarized currents, demonstrating the applicability of the discussed methods not only to engineer material properties for tailored magnetostatics but also for spin dynamics applications and future spintronics developments.

The work is concluded in Chapter 6 and an outlook into future challenges and research opportunities is provided.

## Chapter 2

# Computational discovery of artificial ferromagnets

## 2.1 Ferromagnetism in solids

Microscopically, ferromagnetism originates in an interaction that is purely quantum mechanical in nature. There is no interaction or force that could explain the coupling between magnetic moments seen in ferromagnets in any classical theory, as we can see using a simple calculation. We know that electrons carry a magnetic moment, which can couple classically through the magnetic dipole interaction. If this dipole-dipole interaction was at the origin of magnetic order in ferromagnets, we would expect the critical temperature  $T_c$  to be of the order of the interaction strength. But even the nearest neighbor dipolar interaction in a bcc iron lattice (with lattice constant  $a = 2.49 \text{ \AA}$  and coordination number  $z = 8$ ) yields a temperature  $V_{\text{dipolar}}/k_B \sim z \frac{\mu_0}{4\pi} \frac{(1/2g\mu_B)^2}{k_B a^3} \approx 0.3 \text{ K}$ , which is orders of magnitude smaller than the observed  $T_c = 1043 \text{ K}$ .

The so-called exchange interaction, which is the quantum mechanical origin of magnetic order, will be a central object throughout this work. In order to get an understanding of the underlying physical principles, we shall introduce the exchange interaction in the context of a simple quantum mechanical system, namely the hydrogen molecule. The concepts will then help to understand the long-ranged magnetic order in ferromagnetic phases, specifically those emerging from the percolation of defects in non-magnetic host lattices.

### 2.1.1 Exchange interaction and magnetic order

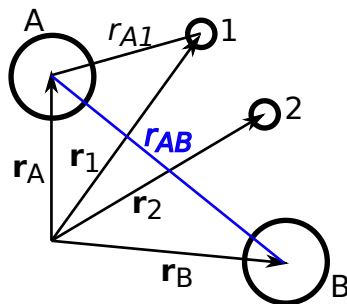


FIGURE 2.1: Sketch of the position vectors used in the calculation of the electronic ground state of the H<sub>2</sub> molecule.

The H<sub>2</sub> molecule consists of two protons and two electrons, which we label  $A, B$  and  $1, 2$ , respectively. Within the spirit of the Born-Oppenheimer approximation, we assume a fixed distance  $R_{AB}$  between the protons. Finally, we call  $r_{A1} = |\mathbf{r}_1 - \mathbf{r}_A|, \dots, r_{B2}$  the distance between the electrons and protons and  $r_{12}$  the distance between the two electrons (see the sketch in Figure 2.1). We can write the Hamiltonian of the two-electron system, taking into account the Coulomb interaction between the charged particles:

$$H = \frac{\hbar^2}{2m} (\nabla_1^2 + \nabla_2^2) + \frac{e^2}{R_{AB}} + \frac{e^2}{r_{12}} - \frac{e^2}{r_{A1}} - \frac{e^2}{r_{A2}} - \frac{e^2}{r_{B1}} - \frac{e^2}{r_{B2}}. \quad (2.1)$$

We note that in the limit  $R_{AB} \rightarrow \infty$ , assuming each electron is associated with only one of the protons, the system dissociates into two non-interacting neutral hydrogen atoms. Treating the interaction as a perturbation, we are interested in those solutions of the Schrödinger equation

$$H\Psi - E\Psi = 0, \quad (2.2)$$

which correspond to the perturbation of two hydrogen atoms in their respective ground state. Therefore, we will express the electronic wave function of the  $H_2$  molecule ground state in the basis of the known hydrogenic 1s wave functions, and write

$$\begin{aligned} \psi_1 &= \frac{1}{\pi} a_0^{-3/2} e^{-\frac{r_{A1}}{a_0}}, \psi_2 = \frac{1}{\pi} a_0^{-3/2} e^{-\frac{r_{A2}}{a_0}}, \\ \varphi_1 &= \frac{1}{\pi} a_0^{-3/2} e^{-\frac{r_{B1}}{a_0}}, \varphi_2 = \frac{1}{\pi} a_0^{-3/2} e^{-\frac{r_{B2}}{a_0}}, \end{aligned} \quad (2.3)$$

meaning that electron 1, 2 is associated with proton A, B respectively. The total wave functions of the unperturbed system are those which describe each electron as being associated with one of the protons, which can be realized in two ways:  $\psi_1\varphi_2$  and  $\psi_2\varphi_1$ . Both configurations have the same energy, twice the hydrogen ground state energy  $E^{(0)}$ . Therefore, the ground state of the unperturbed system is twice degenerate and we find its normalized eigenfunctions

$$\begin{aligned} \Psi_A^{(0)} &= \frac{1}{\sqrt{2+2S}} (\psi_1\varphi_2 + \psi_2\varphi_1), \\ \Psi_B^{(0)} &= \frac{1}{\sqrt{2-2S}} (\psi_1\varphi_2 - \psi_2\varphi_1) \end{aligned} \quad (2.4)$$

(where  $S = \int \psi_1\varphi_1\psi_2\varphi_2 d\mathbf{r}_1 d\mathbf{r}_2$ )<sup>1</sup>.

For the perturbed eigenfunctions, we make the Ansatz

$$\begin{aligned} \Psi_A &= \Psi_A^{(0)} + v_A, \\ \Psi_B &= \Psi_B^{(0)} + v_B, \end{aligned} \quad (2.5)$$

<sup>1</sup>As a side note, we labeled the two orbitals with indices A and B referring to the “anti-bonding” and “bonding” electronic configurations of the  $H_2$  molecule.

and write for the energy of the perturbation  $E^{(1)} = E - 2E^{(0)}$  which we substitute into the Schrödinger equation (2.2):

$$\begin{aligned}
& H \left( \Psi_A^{(0)} + v_A \right) - \left( 2E^{(0)} + E_A^{(1)} \right) \left( \Psi_A^{(0)} + v_A \right) \\
&= \left\{ \frac{\hbar^2}{2m} (\nabla_1^2 + \nabla_2^2) + \frac{e^2}{R_{AB}} + \frac{e^2}{r_{12}} - \frac{e^2}{r_{A1}} - \frac{e^2}{r_{A2}} - \frac{e^2}{r_{B1}} - \frac{e^2}{r_{B2}} \right. \\
&\quad \left. - 2E^{(0)} - E^{(1)} \right\} \left[ \frac{1}{\sqrt{2+2S}} (\psi_1\varphi_2 + \psi_2\varphi_1) + v_A \right] \\
&= \left( H - 2E^{(0)} - E^{(1)} \right) v_A - \left( 2E^{(0)} + E^{(1)} \right) \frac{1}{\sqrt{2+2S}} (\psi_1\varphi_2 + \psi_2\varphi_1) \\
&\quad + \left\{ \left( \frac{\hbar^2}{2m} (\nabla_1^2 + \nabla_2^2) - \frac{e^2}{r_{A1}} - \frac{e^2}{r_{B2}} - \frac{e^2}{r_{A2}} - \frac{e^2}{r_{B1}} \right) \psi_1\varphi_2 \right. \\
&\quad + \left( \frac{\hbar^2}{2m} (\nabla_1^2 + \nabla_2^2) - \frac{e^2}{r_{A1}} - \frac{e^2}{r_{B2}} - \frac{e^2}{r_{A2}} - \frac{e^2}{r_{B1}} \right) \psi_2\varphi_1 \\
&\quad \left. + \left( \frac{e^2}{r_{AB}} + \frac{e^2}{r_{12}} \right) (\psi_1\varphi_2 + \psi_2\varphi_1) \right\} \frac{1}{\sqrt{2+2S}} \\
&= \left( H - 2E^{(0)} - E^{(1)} \right) v_A - E^{(1)} \frac{1}{\sqrt{2+2S}} (\psi_1\varphi_2 + \psi_2\varphi_1) \\
&\quad + \left\{ - \left( \frac{e^2}{r_{A2}} + \frac{e^2}{r_{B1}} \right) \psi_1\varphi_2 - \left( \frac{e^2}{r_{A1}} + \frac{e^2}{r_{B2}} \right) \psi_2\varphi_1 \right. \\
&\quad \left. + \left( \frac{e^2}{r_{AB}} + \frac{e^2}{r_{12}} \right) (\psi_1\varphi_2 + \psi_2\varphi_1) \right\} \frac{1}{\sqrt{2+2S}} \\
&= 0
\end{aligned} \tag{2.6}$$

and similarly for  $\Psi_B$ . This leads us to two inhomogeneous differential equations for the perturbations  $v_A$  and  $v_B$ :

$$\begin{aligned}
\sqrt{2+2S} (H - E) v_A &= \left( E^{(1)} - \frac{e^2}{R_{AB}} - \frac{e^2}{r_{12}} \right) (\psi_1\varphi_2 + \psi_2\varphi_1) \\
&\quad + \left( \frac{e^2}{r_{A2}} + \frac{e^2}{r_{B1}} \right) \psi_1\varphi_2 + \left( \frac{e^2}{r_{A1}} + \frac{e^2}{r_{B2}} \right) \psi_2\varphi_1 \\
\sqrt{2-2S} (H - E) v_B &= \left( E^{(1)} - \frac{e^2}{R_{AB}} - \frac{e^2}{r_{12}} \right) (\psi_1\varphi_2 - \psi_2\varphi_1) \\
&\quad + \left( \frac{e^2}{r_{A2}} + \frac{e^2}{r_{B1}} \right) \psi_1\varphi_2 - \left( \frac{e^2}{r_{A1}} + \frac{e^2}{r_{B2}} \right) \psi_2\varphi_1
\end{aligned} \tag{2.7}$$

The orthogonality requirement for the solutions  $\Psi$  require the right-hand sides of equations (2.7) to be orthogonal to the unperturbed wave functions  $\Psi^{(0)}$ , which allows us to determine the energy perturbations:

$$\begin{aligned}
E_A^{(1)} &= \frac{C+J}{1+S} = \frac{C-JS}{1-S^2} - \frac{CS-J}{1-S^2} \equiv E_C - E_{ex} \\
E_B^{(1)} &= \frac{C-J}{1-S} = \frac{C-JS}{1-S^2} + \frac{CS-J}{1-S^2} \equiv E_C + E_{ex}
\end{aligned} \tag{2.8}$$



where  $E_A^{(1)}$  corresponds to the energy correction for  $\Psi_A$  and  $E_B^{(1)}$  for  $\Psi_B$  and we call

$$\begin{aligned}
C &= \int \left[ \left( \frac{e^2}{r_{12}} + \frac{e^2}{R_{AB}} \right) \frac{\psi_1^2 \varphi_2^2 + \psi_2^2 \varphi_1^2}{2} - \left( \frac{e^2}{r_{A1}} + \frac{e^2}{r_{B2}} \right) \frac{\psi_2^2 \varphi_1^2}{2} \right. \\
&\quad \left. - \left( \frac{e^2}{r_{A2}} + \frac{e^2}{r_{B1}} \right) \frac{\psi_1^2 \varphi_2^2}{2} \right] d\mathbf{r}_1 d\mathbf{r}_2, \\
J &= \int \left( \frac{2e^2}{r_{12}} + \frac{2e^2}{R_{AB}} - \frac{e^2}{r_{A1}} - \frac{e^2}{r_{A2}} - \frac{e^2}{r_{B1}} - \frac{e^2}{r_{B2}} \right) \frac{\psi_1 \varphi_1 \psi_2 \varphi_2}{2} d\mathbf{r}_1 d\mathbf{r}_2, \\
S &= \int \psi_1 \varphi_1 \psi_2 \varphi_2 d\mathbf{r}_1 d\mathbf{r}_2
\end{aligned} \tag{2.9}$$

the Coulomb, exchange and overlap integrals, respectively. We see that the energy correction has a common additive contribution  $E_C$  and an “exchange energy” contribution  $E_{ex}$ , whose sign changes depending on the orbital  $\Psi$ . The integrals C and S have been evaluated by Heitler and London [38] and later Sugiura [39] evaluated the integral J for the H<sub>2</sub> molecule. The exact form of the integrals is quite complicated, but we are mostly interested in their dependence on the distance  $R$  between the two nuclei. For large enough  $R$ , the dominant term in all three integrals is  $\propto e^{-2R/a_0}$ . We can express the Bohr radius  $a_0 = \hbar/\sqrt{2m|E_0|}$  in terms of the hydrogen ground state energy  $E_0$  and find a general relation for the exchange energy

$$E_{ex} \sim e^{-R(\sqrt{2m|E_1|} + \sqrt{2m|E_2|})/\hbar} \tag{2.10}$$

of two electrons that are localized at two distant sites, where they occupy a certain energy level  $E_i$ . This shows that the exchange interaction strength between two electrons vanishes exponentially, the further they are apart. This generally limits the length scale of the exchange interaction to a few Å.

In our description of the problem, we have completely ignored the spin of the electrons, which we have to take into account now. Writing the single spin functions  $\chi_{\pm}$  (where  $\chi_+$  refers to a “spin up” state,  $\chi_-$  to “spin down”), we can find four orthogonal ways to assign them to the two electrons labeled 1 and 2:

$$\begin{aligned}
\chi_1 &= \chi_+(1)\chi_+(2) \\
\chi_2 &= \chi_-(1)\chi_-(2) \\
\chi_3 &= \frac{1}{\sqrt{2}} (\chi_+(1)\chi_-(2) + \chi_+(2)\chi_-(1)) \\
\chi_4 &= \frac{1}{\sqrt{2}} (\chi_+(1)\chi_-(2) - \chi_+(2)\chi_-(1)).
\end{aligned} \tag{2.11}$$

$\chi_1, \chi_2, \chi_3$  describe spin triplet states and  $\chi_4$  the spin singlet.

To satisfy fermion statistics, the total combined wavefunction of the two electron system must be antisymmetric under electron exchange. This requirement restricts the allowed combinations of orbital and spin functions. We find that for the orbital  $\Psi_A$ , only the spin singlet is allowed and for the orbital  $\Psi_B$  only the three spin triplets are allowed. The sign of the exchange interaction  $E_{ex}$  therefore determines the spin configuration in the ground state.

Following the distinction between the singlet and triplet spin states in

the  $H_2$  molecule, the exchange interaction between electrons at neighboring sites in a solid can lower the energy of parallel (ferromagnetic) or antiparallel (antiferromagnetic) arrangement of their spins. If the on-site spin magnetic moment is non-zero, i.e. there exist unpaired spins at a lattice site, and the exchange interaction between neighboring spins favors their parallel arrangement, the solid is said to be ferromagnetic. We should note that this magnetic ordering of spins actually originates from the electrostatic Coulomb interaction between the electrons. Due to translational symmetry, the interaction between neighboring electrons leads to a long-ranged magnetic order and a spontaneous macroscopic magnetization. At finite temperature, the magnetic order is disturbed by thermal fluctuations, which leads to a phase transition at a critical temperature of the order of  $T_c \sim |E_{ex}|/k_B$  ( $k_B$  is the Boltzmann constant).

The emergence of a ferromagnetic phase therefore requires a very specific electronic structure in a solid and it turns out that materials with intrinsic ferromagnetic order above room temperature are rather uncommon among the magnetic compounds known today.

### 2.1.2 Artificial magnetism due to defects

In reality, perfect translational symmetry is usually broken due to imperfections in a material, such as point defects. These defects are randomly distributed in the host lattice and can affect the intrinsic properties of the material. Most notably, some defects can carry non-zero magnetic moment even in non-magnetic hosts. Due to the lifted restriction of translational symmetry, the possibility of a ferromagnetic phase to emerge in a defective material, so-called defect-induced magnetism (DIM), is much larger than in a perfect crystal. On the other hand, we saw that the exchange interaction, which is the microscopic origin of the long-ranged magnetic order, is limited on a length scale of a few Å. Therefore, the defect density must be high enough to allow a sizable interaction between their local magnetic moments. Conceptually, this requirement appears rather challenging, as high amounts of defects also affect the stability of the host lattice and eventually leads to its amorphization. The process leading to an emerging ferromagnetic phase by increasing the defect concentration is called magnetic percolation and is described in detail in section 2.4.

Experimentally, one of the most versatile methods to create such defects is by particle irradiation. The impact of energetic particles, such as ions, on a host lattice leads to a collision cascade between the incoming particles and the host atoms. Nowadays, ion sources ranging over the whole periodic table and kinetic energies of a few eV up to hundreds of MeV are widely available and allow to systematically produce defects while controlling their resulting density.

In the past twenty years, a large number of such artificial ferromagnets have been found experimentally in non-magnetic host materials, such as oxides, nitrides, carbon-based and 2D van der Waals materials, by introducing all kinds of defects [7–9]. But due to the huge number of possible host material and defect combinations, searching for artificial functional ferromagnets experimentally and by brute-force is doomed to fail. A more systematic search method and better selection criteria are highly needed. In the following sections, we describe a computational scheme, which is

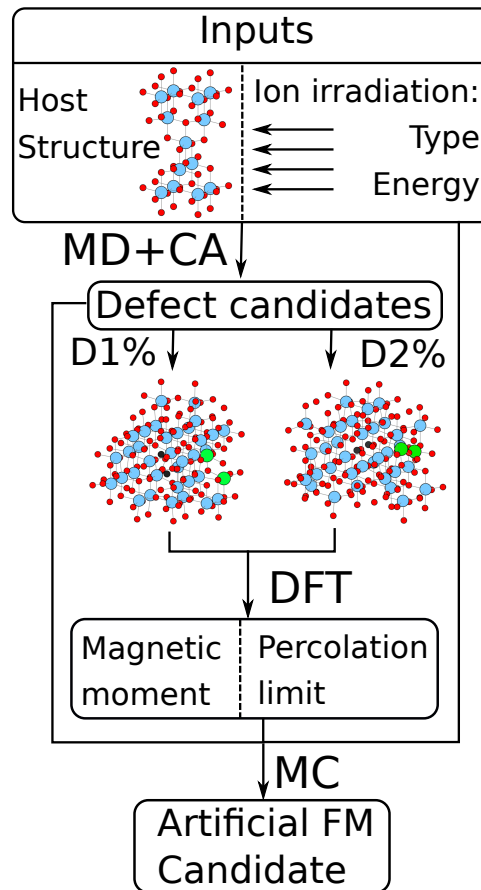


FIGURE 2.2: **Computational scheme for the prediction of artificial functional magnetic materials.** The computational scheme takes as inputs the atomic structure of a host material and the ion type and energy range of the ion irradiation. In a first step, molecular dynamics (MD) simulations and cluster analysis (CA) algorithms yield possible defect structures and their corresponding creation probabilities, likely to be formed during the ion irradiation process. The resulting defective structures are used as input for DFT electronic structure calculations, giving the magnetic ground state and the percolation limit for each defect type. Finally, using the results of all calculations and applying Monte Carlo (MC) methods, a magnetic phase diagram is constructed, which indicates the irradiation parameters likely to create an artificial FM.

depicted in Figure 2.2 and allows the systematic discovery of potential artificial functional ferromagnets, that are realizable experimentally by ion irradiation. Taking as input the atomic structure of a host material, the type and energy of the ion irradiation, potential defective structures and their creation probabilities are obtained using Molecular Dynamics (MD) simulations, as described in Section 2.2. DFT electronic structure calculations are then performed for the resulting defective structures and their magnetic ground state is determined (Section 2.3). For defects yielding a non-zero magnetic moment, the percolation limit is estimated (see Section 2.4). Finally, taking into account ion energy loss in the irradiated host material and the defect formation probabilities predicted by the MD simulations, a magnetic phase diagram can be constructed using Monte Carlo (MC) methods (Section 2.5).

## 2.2 Predicting defect structures from collision cascades

A first step in the computational discovery of artificial functional ferromagnet candidate materials, realizable by ion irradiation, is the selection of potential defects created by ion impact. The standard tool used to calculate ion ranges and irradiation damage is the binary collision code SRIM [40]. This code calculates collisions between an incident ion and atoms in a material using MC methods, taking into account the electronic and nuclear stopping power. Due to the probabilistic nature of the algorithm, the resulting defect structures are not accessible and a more sophisticated method is needed. Classical MD simulations have been used to calculate collision dynamics in the past [41]. In contrast to the MC methods, they take as input the atomic structure of the host material and calculate the displacement of each atom due to their interaction with each other and the incoming ion. The dynamics are calculated in small time steps, usually of the order of a few fs, and the system is let to evolve for 10-100 ps, depending on the energy of the ion. The interactions are modeled using effective pair potentials, taking into account attractive and repulsive forces between the atoms. Some MD codes can also take into account the energy loss of highly energetic ions by interactions with electrons.

Although MD codes exist that are very robust and optimized for speed, these simulations are very time-consuming. Especially when simulating the impact of highly energetic ions, with kinetic energies up to 100 MeV, where the simulated atomic system has to be large enough to contain the entire collision cascade and the time step has to be small enough to accurately capture all interactions, the time needed to perform the simulation can get unreasonably high. Some benchmarks performed on modern computers indicate calculation speeds of the order of millions of atom-time steps per second, which corresponds to a simulation time of  $\sim 100$  ns/day or  $\sim 10^5$  collision cascades calculated per day.

To minimize the computational effort, the simulations can be restricted to the energy range around the displacement threshold of the host atoms. This threshold is usually of the order of  $\sim 10$  eV. Then, the MD simulation starts with the primary knock-on atom (PKA), the host atom involved in the first collision with an impact ion, which is placed at the boundary of the simulation box and given an initial velocity corresponding to the PKA kinetic energy. This allows to use fewer atoms in the simulation box ( $5 \times 10^3$ - $10^4$  atoms) and to simulate a large number of PKAs with different initial conditions. To capture the ballistic dynamics of the collision cascade, it is usually sufficient to evolve the system for  $\sim 10$  ps.

For each PKA, the MD simulation gives the position of each displaced host atom involved in the collision cascade. The resulting atomic structures can be compared with the initial host structure and individual defect types, created during the collision process, can be identified using cluster analysis (CA) techniques. The simulation of a large number of collision cascades allows to evaluate the formation of defects statistically and to obtain defect formation probabilities as a function of the PKA energy.

In order to relate the defect formation probabilities obtained from MD simulations of PKA collision cascades to an ion impact event, the much

faster MC method can be used to calculate the depth and energy distribution of PKAs. In fact, the SRIM code allows to accurately calculate the position and energy distribution of PKAs by simulating  $10^5$  ion impact events within minutes. Using the defect formation probabilities, we can thus efficiently calculate the density distribution of all defects created by ion irradiation, as a function of ion type and energy.

This first step yields the possible defect structures created in a given host lattice by the irradiation with a given kind of ion and their formation probabilities as a function of the ion energy. In the next step, the magnetic ground state of these defect structures has to be determined.

## 2.3 Finding magnetic defect candidates

As mentioned previously, one requirement for a defective host to become an artificial ferromagnet is that the defects carry a non-zero magnetic moment. Therefore, once the possible defect structures created by ion irradiation have been found by means of MD simulations, their magnetic ground state has to be calculated. From the previous step, we know the positions of the displaced atoms within the host lattice of each defect structure. The electronic structure of the defects can then be calculated from first principles within the framework of DFT, whose principles we shall briefly outline.

In solids, the electronic structure can be described by an interacting many-body wavefunction  $|\Psi\rangle$  obeying the Schrödinger equation

$$\hat{H} |\Psi\rangle = E |\Psi\rangle, \quad (2.12)$$

with a Hamiltonian of the form

$$\hat{H} = \hat{T} + \hat{W} + \int d^3r \{v_{\text{ext}}(\mathbf{r})\hat{n}(\mathbf{r}) + \mathbf{B}_{\text{ext}}(\mathbf{r}) \cdot \hat{\mathbf{m}}(\mathbf{r})\}, \quad (2.13)$$

with  $\hat{T}$  the kinetic energy and  $\hat{W}$  the interaction terms,  $v_{\text{ext}}$  and  $\mathbf{B}_{\text{ext}}$  an external electrostatic potential and magnetic field, and  $\hat{n}$  and  $\hat{\mathbf{m}}$  the particle and magnetization density operators. Due to the interaction term  $\hat{W}$ , solving the Schrödinger equation for large systems directly is impossible. DFT allows to map the interacting many-electron system onto an auxiliary non-interacting system.

The basis of DFT is the Hohenberg-Kohn theorem, stating that any state  $|\Psi\rangle$  of a system of interacting electrons described by a Hamiltonian of the form (2.13), is a functional of the densities  $(n, \mathbf{m})$ :

$$|\Psi\rangle \equiv |\Psi[n, \mathbf{m}]\rangle. \quad (2.14)$$

Therefore, any observable of the system must also be a functional of those densities, notably the total energy

$$E = \langle \Psi[n, \mathbf{m}] | \hat{H} | \Psi[n, \mathbf{m}] \rangle \equiv E[n, \mathbf{m}]. \quad (2.15)$$

The ground state  $|\Psi_0\rangle$  is then determined by the density  $(n_0, \mathbf{m}_0)$  that minimizes the total energy:

$$E[n_0, \mathbf{m}_0] < E[n, \mathbf{m}], \forall (n, \mathbf{m}) \in \mathcal{N} \quad (2.16)$$

( $\mathcal{N}$  is the set of all possible densities of the system).

Although the exact functional dependence of the total energy functional is very complicated and unknown, it is universal for all systems with a given kind of interaction  $\hat{W}$  (e.g. Coulomb interaction) and good approximations of the energy functional are known. We note that for our purposes, it is usually sufficient to consider the limit of collinear magnetization in the absence of an external magnetic field, in which case the pair of densities  $(n, \mathbf{m})$  can be expressed by the spin densities  $(n_\uparrow, n_\downarrow)$ , as

$$n = n_\uparrow + n_\downarrow, \mathbf{m} \equiv m\hat{\mathbf{z}} = (n_\uparrow - n_\downarrow)\hat{\mathbf{z}}. \quad (2.17)$$

Knowing the ground state density  $(n_{\uparrow,0}, n_{\downarrow,0})$ , all ground state properties of the system can be calculated, in principle. On the other hand, the ground state density can be determined by minimizing the total energy functional. In DFT, the total energy functional

$$E[n_{\uparrow}, n_{\downarrow}] = T[n_{\uparrow}, n_{\downarrow}] + \int d^3r v_{\text{ext}}(n_{\uparrow} + n_{\downarrow}) + E_H[n_{\uparrow}, n_{\downarrow}] + E_{xc}[n_{\uparrow}, n_{\downarrow}] \quad (2.18)$$

is usually decomposed into contributions from the kinetic energy ( $T$ ), interaction with the external potential ( $v_{\text{ext}}$ ), the Hartree term ( $E_H$ ) and the exchange-correlation term, which accounts for all other interactions.

The ground state density can be determined using the Kohn-Sham (KS) scheme. The system of interacting electrons is mapped onto an auxiliary system of non-interacting electrons, subject to an effective potential  $v_s^{\sigma}[n_{\uparrow}, n_{\downarrow}]$ , yielding the same density as the original system. This auxiliary system obeys the KS equations of spin-density functional theory

$$\left\{ -\frac{\hbar^2 \nabla^2}{2m} + v_s^{\sigma}[n_{\uparrow}, n_{\downarrow}](\mathbf{r}) \right\} \phi_{\alpha\sigma}(\mathbf{r}) = \epsilon_{\alpha\sigma} \phi_{\alpha\sigma}(\mathbf{r}), \quad (2.19)$$

for the auxiliary wavefunctions  $\phi_{\alpha\sigma}(\mathbf{r})$  (where  $\sigma = \uparrow, \downarrow$  is the spin index) of the non-interacting system. The effective potential takes the form

$$v_s^{\sigma}[n_{\uparrow}, n_{\downarrow}] = v_{\text{ext}} + v_H[n] + v_{xc}^{\sigma}[n_{\uparrow}, n_{\downarrow}], \quad (2.20)$$

where the spin-dependent exchange-correlation potential

$$v_{xc}^{\sigma}[n_{\uparrow}, n_{\downarrow}] = \frac{\delta E_{xc}[n_{\uparrow}, n_{\downarrow}]}{\delta n_{\sigma}} \quad (2.21)$$

is the functional derivative of the exchange-correlation energy w.r.t the spin density and accounts for internal spin interactions (such as the exchange interaction introduced earlier). Eq. (2.19) can be solved self consistently with an initial guess of the density and yields the ground state spin density  $(n_{\uparrow,0}, n_{\downarrow,0})$ , which we need in order to determine the magnetic properties of the defects found in the MD simulations.

At each self-consistency iteration step, the KS equations (2.19) must be solved numerically. Therefore, they have to be brought into a form that is convenient for the computer. This is usually done by expanding the KS wavefunctions  $\phi_{\alpha\sigma}$  using a finite set of basis functions, transforming the KS equations into a linear algebra problem. The choice of the basis strongly depends on the system. In quantum chemistry, for the description of molecular systems, atomic-like basis functions are very popular. For the description of periodic systems, planewave basis functions are a common choice. Often, these planewaves are used to describe only the delocalized valence electrons, as an accurate description of localized core electrons require a very large number of planewaves. The contribution of the core electrons to the charge density must then be accounted for separately. One popular method is the use of pseudopotentials, which incorporate the core electron contribution in an effective external potential. The Full-potential Linearized Augmented Planewave (FLAPW) method, used in this work and described in Section 2.5.2, employs a combination of these two types of basis functions to accurately describe all electrons in the system.



In practice, calculations of the electronic structure of defective solids are performed using the supercell technique, where defects are embedded in a supercell consisting of several unit cells of the host lattice. Applying periodic boundary conditions to the whole supercell, a periodic lattice with the periodicity of the host lattice can be modeled and the size of the supercell determines the defect concentration in the system. Varying the defect concentration allows to estimate the percolation threshold, at which the magnetic defects start to interact ferromagnetically. We should mention that, although supercell methods are widely used in the literature to calculate the electronic structure of defects in solids, more advanced schemes exist that overcome some of their limitations. Especially Green's function methods should be mentioned, which among other convenient features allow for a natural embedding of defects in a host system and give direct access to the exchange interaction parameters via the Liechtenstein formula [42].

## 2.4 Magnetic percolation

In the previous sections, we introduced the exchange interaction between two electron spins, which is the microscopic origin of long range magnetic order. We saw that this interaction was limited in range, as it vanishes exponentially with the distance between two spins. In artificial ferromagnets, where the spins are localized at defects, the interaction strength is governed by the defect density. For a ferromagnetic phase to emerge in a defective host material, the defect concentration must be larger than a critical threshold, the so-called magnetic percolation limit.

To get an understanding of the emergence of a long ranged magnetic order in a defective host material, we simulate the magnetic percolation process in an anatase  $\text{TiO}_2$  host. As discussed in detail in the next section, dFP defects are mostly responsible for the artificial ferromagnetism in this host material. We first generate a supercell of  $200 \times 200 \times Z$  ( $Z \in [1, 200]$ ) unit cells, and randomly mark some of the cells as containing a dFP defect. Then, applying Algorithm 1, we find all cells in the grid that contain a dFP and are close enough to interact with each other. These interacting cells form a percolation domain. To simulate a bulk host, we enforce periodic boundary conditions.

---

### Algorithm 1: Search percolation domains in a random grid

---

```

input : grid, LxMxN grid of cells, randomly marked as defect
input :  $r_{\max}$ , Threshold distance of the interaction
output: labels, LxMxN grid of labels 0-number of domains

1 current_label  $\leftarrow$  0;
2 foreach cell with index i in grid do
3   if cell is not visited and cell contains defect then
4     current_label  $\leftarrow$  current_label + 1;
5     Initialize an empty queue;
6     push cell to queue;
7     mark cell as visited;
8     assign current_label to cell;
9     while queue is not empty do
10      take cell from queue;
11      foreach neighbor at distance  $r \leq r_{\max}$  do
12        if neighbor is not visited and neighbor contains defect
13          then
14            push neighbor to queue;
15            mark neighbor as visited;
16            assign current_label to neighbor;
17          end
18        end
19      end
20 end

```

---

Examples of such grids are shown in Figure 2.3(c-e), containing 2.5 at.%, 7.5 at.% and 10 at.% dFP defects, respectively, where each percolation domain is shown in a different color (black cells are not magnetic). We see that, at low defect concentration, the percolation domains are small and isolated

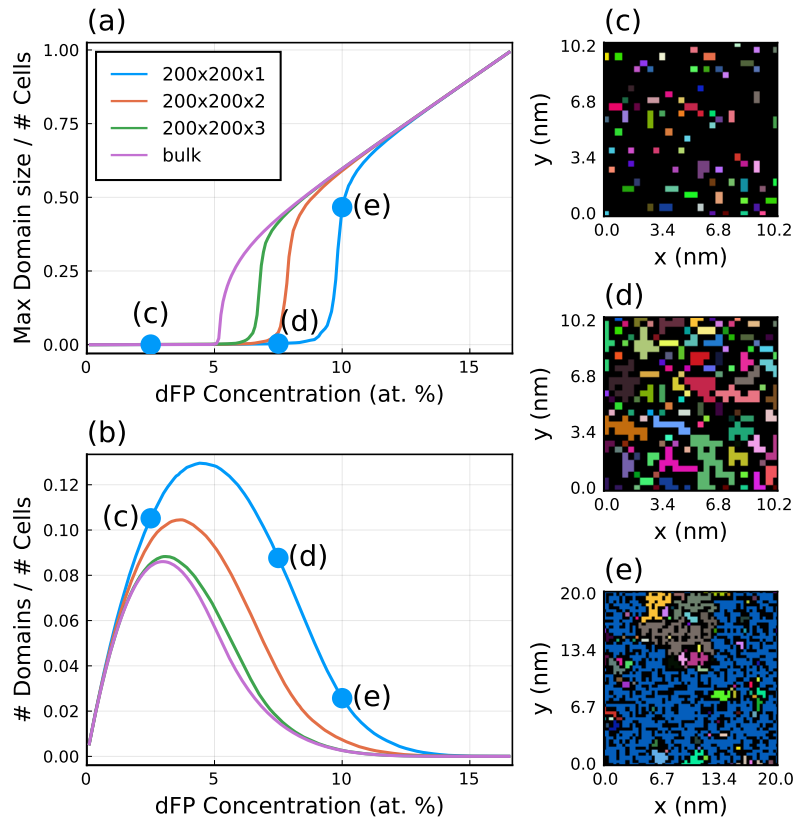


FIGURE 2.3: **Percolation model of an emerging artificial ferromagnetic phase.** We simulate a  $200 \times 200 \times Z$  unit cell  $\text{TiO}_2$  lattice, with a thickness  $Z$  of 1, 2, 3 and 200 unit cells. Each cell is randomly marked as containing a magnetic di-Frenkel Pair (dFP) defect with a probability  $P \in [0, 1]$ . Nearest neighbor magnetic cells interact and form percolation domains. Varying the probability  $P$ , and thereby the dFP concentration, we see three regimes: at low concentration ( $< 5$  at. % in the monolayer), the sample is paramagnetic and the percolation domains are small. In the intermediate regime (5-9 at. % in the monolayer), the magnetic dFP defects start to interact and the domains grow rapidly in size. At the percolation threshold, 9 at. %, 7.5 at.%, 6 at.% and 5 at. % in the mono-, bi-, trilayer and the bulk system, respectively, the domains merge and form a large percolation continent. (a) The figure shows the number of cells that can be found in the maximum possible domain (normalized by the total number of cells) for the four computed sizes and as a function of the dFP concentration. (b) Similar to (a) but for the number of percolation domains (normalized by the total number of cells). (c)-(e) Examples of monolayer grids, in which individual domains are color-coded. The colors are arbitrary and are only meant to visualize the different domains. Black cells correspond to non-magnetic cells that do not contain any dFP defect. Regions of the same color correspond to percolation domains, in which each cell has at least one nearest neighbor cell containing a dFP. The defect concentration was set to 2.5 at. % (c), 7.5 at. % (d) and 10 at. % (e). These three examples are marked by blue dots in (a) and (b).

System Dimensions	$\beta$
2	$0.138 \pm 0.004$
3	$0.417 \pm 0.003$

TABLE 2.1: Critical exponent  $\beta$  of the magnetic percolation transition.

(Figure 2.3(c)) and no long-range order can emerge. Increasing the defect concentration, the isolated percolation domains grow (Figure 2.3(d)) and finally merge to form one large domain (Figure 2.3(e)), called the percolation continent.

By simulating a large number ( $10^5$ ) of such random grids, using different defect concentrations, we calculate the average size of the percolation continent (the largest percolation domain in the grid) and the average number of percolation domains. Figure 2.3(a) shows the size of the percolation continent (normalized to the grid size) as a function of the defect concentration, for different grid geometries. We observe that the continent starts to grow rapidly at a certain defect concentration, the percolation threshold, that depends on the geometry of the grid. In the bulk, the percolation threshold is at 5 at.% according to the DFT calculations. Reducing the dimensionality of the system, the simulations (Figure 2.3(a)) show that the threshold shifts to higher concentrations up to 10 at.% in a  $\text{TiO}_2$  monolayer.

Figure 2.3(b) shows the number of percolation domains (normalized to the grid size) as a function of the defect concentration. We can identify three regimes in the percolation process. At low concentrations ( $< 5$  at.% in the  $\text{TiO}_2$  monolayer), the number of domains increases almost linearly and the percolation domains are small and isolated. The sample is paramagnetic, no long-range order emerges. At intermediate defect concentrations (5-9 at.% in the  $\text{TiO}_2$  monolayer), the number of percolation domains decreases and their average size grows. The domains start to merge and a medium range interaction starts to emerge. In this regime the sample is usually superparamagnetic. At the percolation threshold, large domains start to merge and form a percolation continent, that grows. This is the onset of the long-ranged order and the ferromagnetic phase emerges.

This process describes a second order geometrical phase transition at a critical defect concentration  $p_c$ . In statistical physics, the behavior of a system undergoing such a phase transitions is characterized by an order parameter. Here, the order parameter is the probability  $P_\infty$  that a cell belongs to the percolation continent. As the magnetic cells are randomly selected,  $P_\infty$  is simply equal to the size of the percolation continent divided by the total number of cells (Figure 2.3(a)). The critical behavior of the order parameter at the phase transition follows a universal power law

$$P_\infty \propto (p - p_c)^\beta \quad (2.22)$$

with the critical exponent  $\beta$ . This exponent only depends on the dimensionality of the system and is otherwise universal. Table 2.1 shows the values of  $\beta$  obtained from the simulations of the bulk 3D and the monolayer 2D system.

For a defective host material to become an artificial ferromagnet, with a

---

robust emerging long-range ordered phase, it is therefore necessary to introduce a defect concentration larger than the percolation limit. But large defect densities also affect the stability of the host lattice and inevitably lead to its amorphization. Finding an optimal defect concentration is therefore essential to create artificial functional magnetic materials. In the next section, we will apply the computational scheme described in this chapter step by step to the anatase  $\text{TiO}_2$  host lattice and illustrate its predictive power.

## 2.5 Magnetic phase diagram of anatase $\text{TiO}_2$ artificial ferromagnet

In the previous sections, we have introduced the concept of artificial magnetic materials, created by introducing defects in non-magnetic host lattices by means of ion irradiation. We have described a computational scheme to systematically discover potential artificial ferromagnet candidates. In the following section, we apply this scheme to the widely available non-magnetic semiconducting oxide  $\text{TiO}_2$ , a well-known host material for artificial ferromagnetism, to test its predictive power. In the next chapter, the predictions will be tested by experiment.

### 2.5.1 Defect creation in anatase $\text{TiO}_2$

The first step consists in finding defect structures created by ion irradiation. As explained in Section 2.2, rather than simulating the ion impact directly, MD simulations of the PKAs have the advantage of reducing the computational cost and complexity. Robinson et al. [43, 44] have carried out detailed MD simulations of low energy collision cascades for PKAs in the three low-pressure polymorphs of  $\text{TiO}_2$ , namely rutile, anatase and brookite, at PKA energies around the displacement threshold. As already mentioned, during the MD simulation, the PKA is displaced under the influence of an external force and interacts with the other atoms of the host lattice through a set of pair potentials. In their simulations, Robinson et al. employ the Buckingham pair potential to model equilibrium atomic interactions and the Ziegler-Biersack-Littmark pair potential to capture nuclei-nuclei interactions at small atomic separation, which is necessary to capture the collision dynamics. Simulations were carried out in large supercells (rutile: 4608 atoms, anatase: 4800, brookite 6144 atoms) at  $T = 300$  K. For each of the polymorphs, 10 lattice configurations have been equilibrated for different durations between 12 and 20 ps, resulting in different starting lattice configurations for the collision cascade simulations. Then, the collision cascades resulting from the two possible PKAs (Ti and O) have been simulated in each of the starting lattices for 10 ps. In total, simulations of 100 different initial PKA directions sampled uniformly from the unit sphere, with energies of 5 eV to 200 eV (in steps of 5 eV), were performed in each of the initial lattice configurations, resulting in  $8 \times 10^5$  MD simulations per polymorph. This large degree of statistical sampling allows for a detailed defect analysis. Defect cluster analysis was performed on each of the resulting collision cascades. Specifically, the residual damage, i.e. the resulting point defects such as vacancies and interstitials, was decomposed into cluster domains using a recursive neighbor search algorithm (similar to Algorithm 1) with a cutoff of 3 Å. This allows to categorize types of defect clusters with similar structure and to perform statistical analysis over the types of defects resulting from PKAs in specific ranges of initial energy. The authors categorize all defect clusters containing up to four constituent point defects. All other clusters are categorized as large clusters and are not analyzed any further.

The results obtained in the anatase polymorph are especially interesting: At Ti PKA energies  $E_{\text{PKA}}$  near the Ti displacement threshold ( $E_d = 39$  eV  $\leq E_{\text{PKA}} \leq E_d + 20$  eV), most defects are found on the Ti sublattice and one of the primary defect complexes, formed with a creation probability

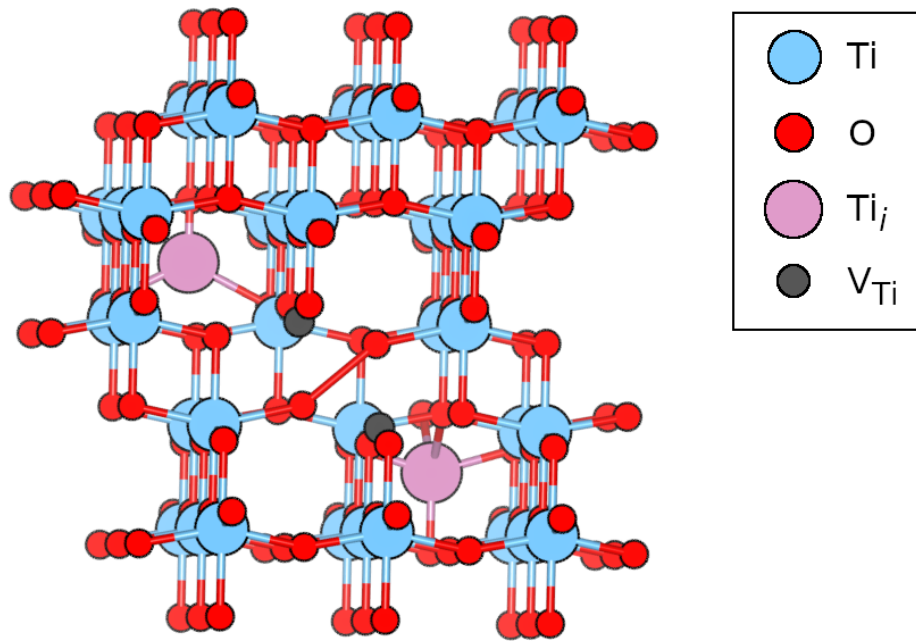


FIGURE 2.4: **Sketch of a dFP defect in anatase  $\text{TiO}_2$ .** A  $3 \times 3 \times 1$  supercell of the anatase structure is shown containing two Ti vacancies ( $V_{\text{Ti}}$ ) and two Ti interstitials  $\text{Ti}_i$ .

of 42 % in the simulated collision cascades, is the dFP. It emerges from the displacement of two Ti atoms into interstitial positions leaving two Ti vacancies and two Ti interstitials (see Figure 2.4). Other defects include single oxygen vacancies (13 %) and interstitials (18 %) (see Figure 2.5(a)). At higher impact energies, the formation of di-vacancies and large defect clusters is more prevalent (see Figure 2.5(b)), leading to the amorphization of the host matrix. For oxygen PKAs, the most prevalent defects are isolated oxygen vacancies and interstitials over the whole simulated PKA energy range (see Figure 2.5(c,d)).

The next step consists in finding the magnetic properties of the defect structures identified by the MD simulations. We recall that for a robust magnetically ordered phase to emerge, a rather high concentration of defects with a non-zero magnetic moment are necessary to overcome the percolation threshold. Already at this stage, the probability distribution of defects created by the collision cascades and obtained by MD simulations can give some hints as to whether a host material could be turned into an artificial ferromagnet. In the case of anatase  $\text{TiO}_2$ , mainly three different kinds of defects are created at low impact energies, namely dFP, oxygen vacancies and interstitials. On the other hand, at higher impact energies, the amount of random disorder is much higher, which would favor amorphization over magnetic percolation. We stress that, in general, amorphous phases do not show FM, but if at all, they show paramagnetism.

### 2.5.2 Magnetic properties of dFP defects in anatase $\text{TiO}_2$

Magnetic properties of many defects in  $\text{TiO}_2$  have been calculated in the past, such as oxygen vacancy ( $O_V$ ) [45, 46], Ti interstitial ( $\text{Ti}_i$ ) [47] and the

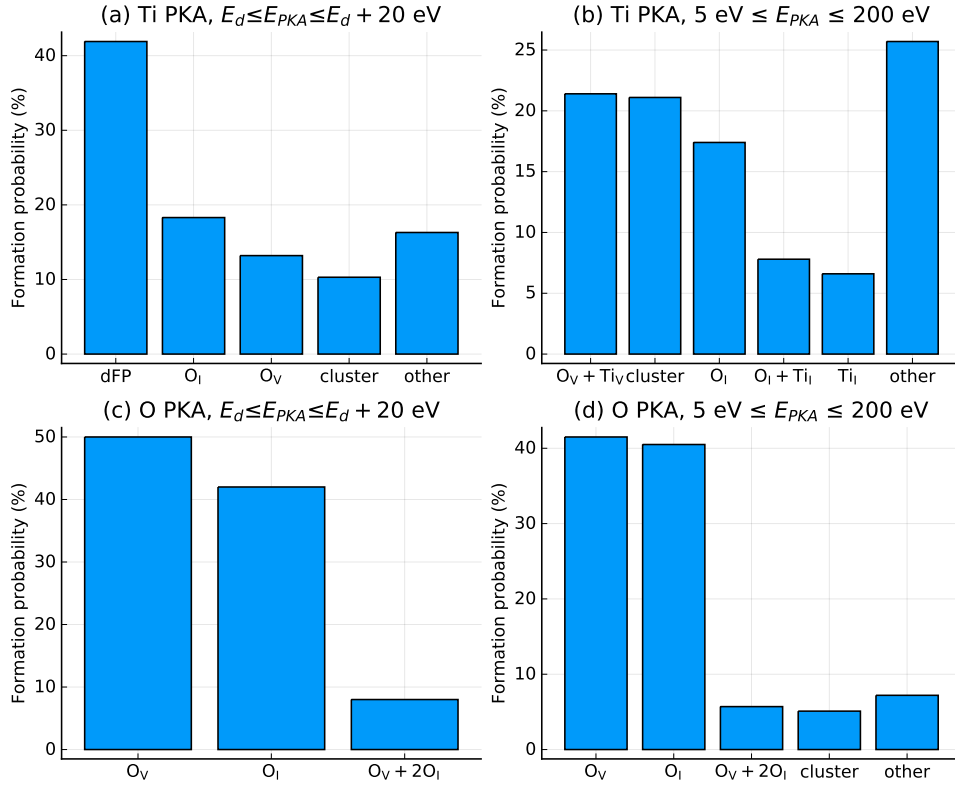


FIGURE 2.5: **Defect creation probabilities** resulting from MD simulations of Ti and O PKAs in the anatase polymorph of  $\text{TiO}_2$ . At each PKA energy, taken from the range 5 eV to 200 eV in steps of 5 eV, 100 initial impact directions were sampled from the unit sphere and each resulting collision cascade was simulated in 10 different initial anatase lattices consisting of 4800 atoms during 10 ps. The resulting irradiation damage was analyzed using clustering methods and categorized by type of defect clusters. The defect formation probability was then calculated over the whole sample of  $8 \times 10^5$  MD runs. Panels (a,b) show the probability distribution of the most prevalent defect types created by Ti PKAs with energies near the Ti displacement threshold of  $E_d^{\text{Ti}} = 39$  eV (a) and in the whole simulated energy range (b). Panels (c,d) show similar results for the O PKAs. (Data taken from Reference [44]).



dFP [34].

Notably, Stiller et al. [34] have performed DFT spin structure calculations for each dFP configuration in anatase, with vacancy-interstitial distances ranging from 3 Å (first nearest neighbor) to 10 Å (twelfth nearest neighbor) and vacancy-vacancy distances ranging from first to ninth nearest neighbors, or a total of 108 different dFP configurations. They used the projector augmented-wave (PAW) method with the Perdew-Burke-Ernzerhof (PBE) exchange correlation functional and an additional screened on-site Coulomb interaction of  $U = 4$  eV on Ti 3d orbitals. Each defect structure was embedded in a  $3 \times 3 \times 1$ -supercell of the anatase host. Five of the simulated dFP configurations resulted in a magnetic ground state, having a magnetic moment of  $2\mu_B$  per dFP. The magnetic moments coupled ferromagnetically at a distance of  $\sim 6$  Å.

Wang et al. [46] calculated the magnetic ground state of  $\text{O}_V$  at the (001)-surface of anatase  $\text{TiO}_2$  and their magnetic interactions, using the PAW method with PBE functional and a screened Coulomb interaction of  $U = 3.3$  eV. The defects were embedded in a  $2 \times 4 \times 7$ -supercell slab of the host surface. They find that the  $\text{O}_V$  defect structures carry a magnetic moment of  $1.63\mu_B$  and couple ferromagnetically up to a distance of  $\sim 8$  Å.

In this work, the magnetic properties of one of the dFP defects investigated in [34] (labeled “di-FP1” in the reference) were calculated on the basis of density functional theory using the FLAPW method implemented in the FLEUR code [48], in order to illustrate the process and to confirm the results obtained by the authors. In the FLAPW method, the unit cell is partitioned into non-overlapping muffin-tin (MT) spheres of radius  $r_{MT}$ , centered at each atom and an interstitial region (IR) (see Figure 2.6).

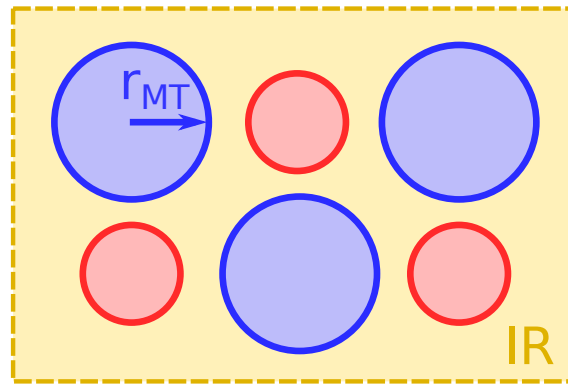


FIGURE 2.6: **Muffin-tin decomposition** In the FLAPW method, space is decomposed into non-overlapping spherical muffin-tin (MT) regions, indicated by blue and red circles, of radius  $r_{MT}$ , centered at the atom positions and an interstitial region (IR), shown in yellow. The MT radius is specified per atom type in the system, here two different types are indicated in blue and red.

Inside the MT spheres, a set of atomic-like basis functions are used to describe the localized core electron states and in the IR, the basis set consists of plane waves to best describe the delocalized valence states. At the MT boundaries, the resulting wavefunctions are matched in value and slope to ensure continuity requirements. Specifically, the LAPW basis set has the

form

$$\phi_{kG}(r) = \begin{cases} \frac{1}{\sqrt{\Omega}} e^{i(k+G)r} & \text{for } r \in \text{IR} \\ \sum_L [a_{kG}^{L\alpha} u_l^\alpha(r_\alpha, E_l^\alpha) + b_{kG}^{L\alpha} \dot{u}_l^\alpha(r_\alpha, E_l^\alpha)] Y_L(r_\alpha) & \text{for } r \in \text{MT}^\alpha \end{cases} \quad (2.23)$$

where  $u_l^\alpha$  are solutions to the radial Schrödinger equation in the potential of atom  $\alpha$  and  $\dot{u}_l^\alpha$  their energy derivatives.  $Y_L$  are spherical harmonics with the composite index  $L = (l, m)$  for the angular momentum quantum numbers. The coefficients  $a_{kG}^{L\alpha}$  and  $b_{kG}^{L\alpha}$  are determined by the continuity condition at the MT boundary. The size of the basis set is controlled by several cutoff parameters, that have to be carefully tuned in order to obtain high quality results: The summation over the index  $L$  is limited by the cutoffs  $l_{\max}^\alpha$ . For Ti atoms,  $l_{\max} = 8$  was used and for O atoms  $l_{\max} = 6$ . For the plane wave part of the basis, a cutoff parameter  $K_{\max} = |k + G|_{\max}$  and the grid of  $k$ -vectors used to sample the first Brillouin zone determine the plane-wave basis used in the IR. Here, a value of  $K_{\max} = 4.5 \text{ \AA}^{-1}$  and a grid of  $6 \times 6 \times 8$   $k$ -vectors were used.

The FLEUR code differentiates between three types of electron states, namely core electrons, semi-core electrons and valence electrons. The semi-core electrons are treated in a similar way to the valence electrons, but the basis functions are localized to the MT spheres, so-called semi-core local orbitals (SCLO), of the form:

$$\phi_L^{\text{LO}}(r) [a_L^{\text{LO}} u_l^\alpha(r_\alpha, E_l^\alpha) + b_{kG}^{L\alpha} \dot{u}_l^\alpha(r_\alpha, E_l^\alpha) + c_L^{\text{LO}} u_l^\alpha(r_\alpha, E_l^{\text{LO}})] Y_L(r_\alpha) \quad (2.24)$$

with an additional radial function. The parameters  $a, b, c$  are determined such that the basis function value and slope vanish at the MT boundary. The core electron density is calculated fully relativistically by solving the Kohn-Sham-Dirac equations.

The atomic configuration of Ti is [Ar] 3d<sup>2</sup> 4s<sup>2</sup> and of O is [He] 2s<sup>2</sup> 2p<sup>4</sup>. For the calculation of the TiO<sub>2</sub> electronic structure, the Ti 3d and 4s states were treated as valence states, while the 3s and 3p states were treated as semi-core states. The O 2p states were treated as valence states and the 2s as semi-core states. A supercell of  $3 \times 3 \times 1$  anatase unit cells was constructed, containing one dFP defect. The defect structure corresponds to the ‘‘di-FP1’’-defect in [34]. The spin density  $\rho_\sigma$  was converged to self-consistency and the resulting magnetization ( $M = \rho_\uparrow - \rho_\downarrow$ ) is shown in Figure 2.7. The total magnetic moment per supercell was found to be  $2 \mu_B$  with  $0.54 \mu_B$  concentrated at each of the two Ti interstitials (marked in purple in Figure 2.7).

The magnetization extends out from the Ti interstitials and their nearest neighbor Ti atoms in the  $xz$ -plane with a  $d_{xz}$ -like symmetry. Additionally, a non-zero magnetization is found at the nearest neighbor O atoms. Figure 2.8 shows a map of the magnetic moment distribution on the  $xz$ -plane going through the two Ti interstitials ( $\text{Ti}_i$ ). It can be seen that the majority of the magnetic moment is distributed at the  $\text{Ti}_i$  and their two nearest neighbor Ti host atoms. Additionally, the nearest neighbor oxygen atoms and the next-nearest Ti atom carry magnetic moment.

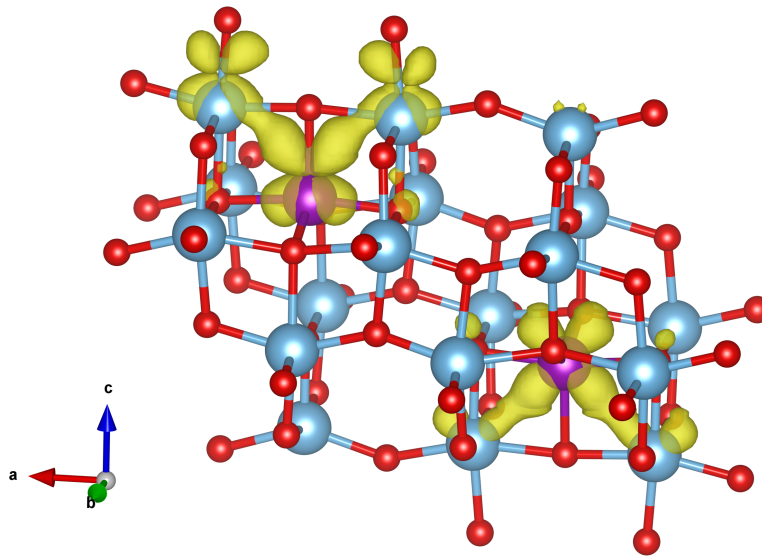


FIGURE 2.7: **Magnetization of the dFP defect supercell.** Ti atoms are shown as blue spheres, O atoms as red spheres and the two Ti interstitials as purple spheres. An isosurface corresponding to 10 % of the maximum magnetization is shown in yellow.

After obtaining a self-consistent spin density, the density of the Kohn-Sham states used in the self-consistency cycle is calculated. It should be noted that the resulting density of states (DOS) is the one corresponding to the effective non-interacting electron system and care should be taken when interpreting it. Especially in transition metal oxides, this approximation often leads to a crude underestimation of the bandgap. Nonetheless, the DOS calculated from the KS states can yield valuable information about the electronic structure of the material.

Figure 2.9 shows the DOS calculated for the anatase TiO<sub>2</sub> supercell containing one dFP defect. The upper half of the DOS (positive values) shows the density of states in the majority spin channel (“spin-up”), while the lower half (negative values) shows the density of states in the minority spin channel (“spin-down”). The energy scale (on the x-axis) is referenced to the highest occupied state. The total DOS, shown in grey, forms two large bands: the valence band on the left and the conduction band on the right. The lower-lying core states are not shown. The two bands are separated by a bandgap of 2.2 eV, which underestimates the experimental bandgap of 3.2 eV, as stated above. Within the bandgap, a narrow defect band is formed, which is not present in the pristine system. While the valence band density is almost identical in the two spin channels, the narrow defect band is strongly spin-polarized. Not only the density of states but also the bandwidth of the narrow defect band is higher in the majority spin channel.

From the KS states, the density of states can be projected on certain atomic orbitals, yielding the so-called projected density of states (PDOS). In Figure 2.9, the PDOS projected on the O 2p orbitals is shown in blue and the PDOS projected on the Ti 3d orbitals is shown in orange. Most O 2p states are located in the valence band, whereas most Ti 3d states are located in the conduction band.

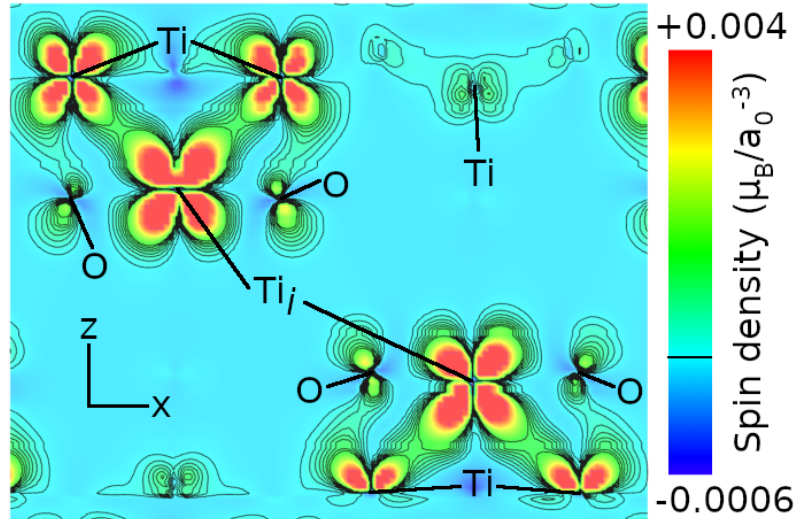


FIGURE 2.8: **Magnetization in the XZ-plane through the Ti interstitials.** A heatmap of the magnetization is shown in a cut through the supercell along the XZ-plane passing through the Ti interstitials. The magnetization is given in units of  $\mu_B/a_0^3$ . The positions of the Ti interstitials ( $Ti_i$ ), the host Ti and O atoms are marked. The cyan color corresponds to zero magnetization. Warmer colors (red) indicate positive magnetization, cooler colors (blue) indicate negative magnetization. The quantization axis is along the Z-direction.

Looking at the defect band, one sees that O 2p states are present in both spin channels and their density is almost equal. This matches with the low magnetization around the oxygen atoms, as shown in Figure 2.8. On the other hand, a rather large density of Ti 3d states is present in the majority spin channel, compared to the density of Ti 3d states in the minority spin channel. This matches the local  $d_{xz}$  symmetry of the magnetization around the  $Ti_i$  and surrounding Ti host atoms and with the fact that the two  $Ti_i$  carry more than half of the total magnetic moment in the supercell.

Overall, the computational results match those published in Reference [34]. The dFP defects are certainly a good defect candidate for the formation of an artificial ferromagnetic phase in anatase  $TiO_2$ .

### 2.5.3 Constructing a magnetic phase diagram

The final step consists in combining the results obtained from MD simulations and DFT magnetic property calculations. From MD simulations, we obtained the probability distribution of defects created as a function of the PKA energy. The cascades resulting from the PKAs have to be related to ion impact events resulting from the ion irradiation. In addition to ion collisions, other effects that influence the ion range and energy loss have to be taken into account, such as ion-electron interactions. The MC methods, as implemented in the SRIM code, can be used to calculate the energy and depth distribution of PKA collisions resulting in a  $TiO_2$  host from ion irradiation.

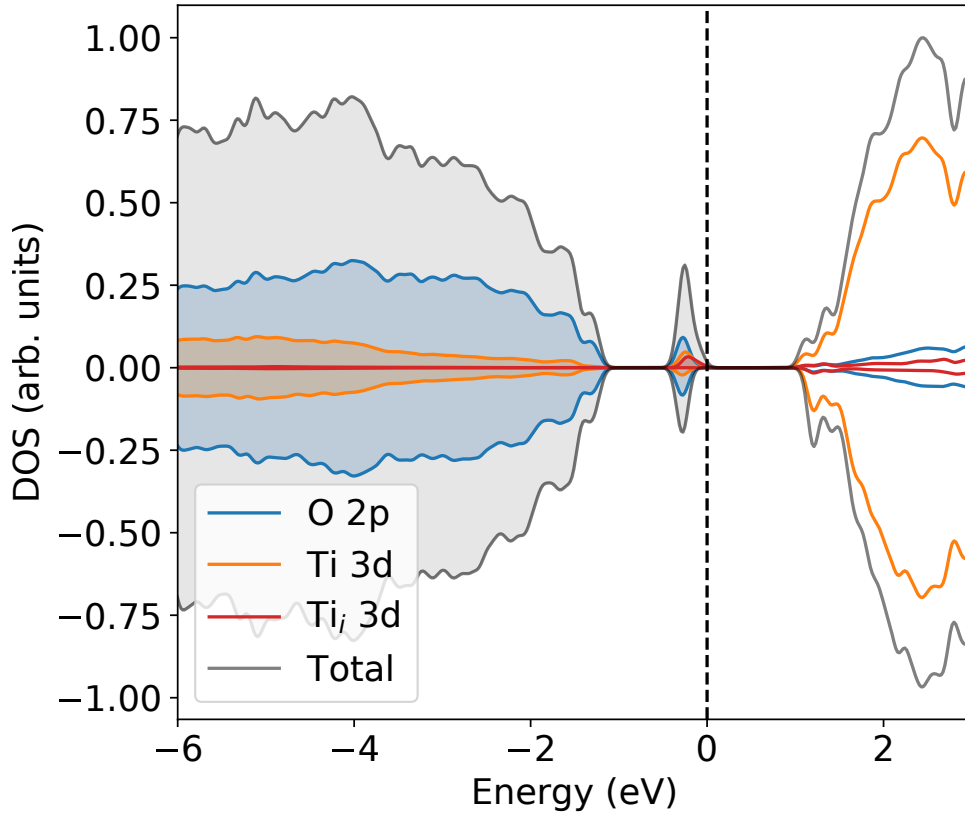


FIGURE 2.9: **Density of states (DOS)** of the anatase  $\text{TiO}_2$  supercell containing one dFP defect. The total DOS is shaded in grey. The partial DOS, projected on the O 2p states and on the Ti 3d states is shaded in blue and orange, respectively. The energy is referenced to the highest occupied state (at  $E = 0$  eV), which lies in the anatase  $\text{TiO}_2$  bandgap. Positive values of the DOS show states in the majority spin channel (“spin-up”) and negative values indicate states in the minority spin channel (“spin-down”). A narrow spin-polarized band emerges within the bandgap due to the dFP defect.

In the full cascade mode, the SRIM code saves detailed information about each simulated collision in the “COLLISION.txt” output file, which can be read and further analyzed based on the results of the MD simulations. We performed MC simulations of collision events resulting from  $10^5$   $\text{Ar}^+$  ions, at ion energies in the range  $200 \text{ eV} \leq E_{\text{ion}} \leq 1500 \text{ eV}$  in steps of 50 eV, into a  $\text{TiO}_2$  target of 100 nm thickness. The resulting defects were then calculated based on the PKA energies and the probability distribution obtained by the MD simulations. The depth distribution of all resulting defects was calculated using a histogram method, by accumulating one bin per atomic layer of the  $\text{TiO}_2$  host.

Figure 2.10 shows the resulting depth distributions as a function of the ion energy. Figure 2.10(a) shows the distribution of dFP defects along the (001)-direction (x-axis, in units of  $c$  lattice constants) created by the irradiation with an  $\text{Ar}^+$  fluence of  $10^{16} \text{ cm}^{-2}$ , as a function of the ion energy (y-axis). The dFP concentration is indicated by the color scale in at. %. We first observe that the dFP defects are distributed over a larger region below the

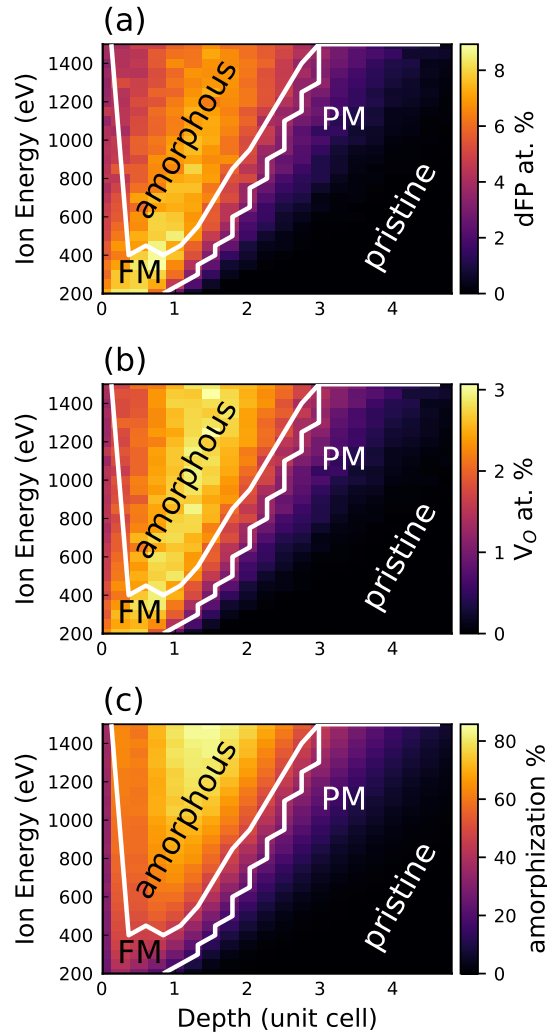


FIGURE 2.10: **Defect distribution** created in anatase  $\text{TiO}_2$  host by  $\text{Ar}^+$  ions with a fluence of  $10^{16} \text{ cm}^{-2}$  as a function of ion energy. The depth is indicated in unit-cells along the (001) crystal direction ( $c = 9.75 \text{ \AA}$ ). The color scales indicate the defect concentrations. The white lines separate regions with high enough defect concentration to form a FM phase, with high degree of amorphization (amorphous), with low defect concentration forming a paramagnetic phase (PM) and of pristine host material. The color scale indicates: (a) the distribution of dFP (in at.%), (b) the distribution of oxygen vacancies (in at.%), (c) the degree of amorphization (in %).



sample surface, the higher the ion energy. At  $200 \text{ eV} \leq E_{\text{ion}} \leq 400 \text{ eV}$ , the dFP are mostly confined to the first unit cell below the surface, whereas at  $1000 \text{ eV}$ , they spread over three unit cell layers. Furthermore, at low irradiation energies, the dFP defects are much more concentrated and reach densities of up to 8 at.%, compared to a maximum of 6 at.% at  $E_{\text{ion}} = 1000 \text{ eV}$ .

Similar results are obtained for the oxygen vacancy defects, as shown in Figure 2.10(b). There, the maximum defect density is overall smaller (3 at.%) compared to the dFP defect, but is also less affected by the ion energy, i.e. concentrations of 3 at.% are found throughout the considered ion energy range. A similar broadening of the depth distribution at higher ion energies, comparable to the dFP defect is observed.

From DFT calculations, we know that these two types of defects carry non-zero magnetic moment, which couple ferromagnetically upon reaching the percolation threshold of  $\sim 5 \text{ at.}\%$  [34, 45, 46] (corresponding to a defect separation of  $\sim 6 \text{ \AA}$ ). This allows to define a region in parameter space, in which an artificial ferromagnetic phase can emerge. This region is indicated in Figure 2.10 by a white line separating a ferromagnetic (FM) and a paramagnetic (PM) region.

Besides dFP and  $\text{O}_V$ , other types of defects are also created during the ion irradiation, which do not contribute to the magnetic percolation process, but affect the stability of the host lattice. The amorphization of the host lattice counteracts the emergence of a robust FM phase, and therefore has to be taken into account. We define the degree of amorphization as the percentage of atoms displaced from their equilibrium position in the pristine host lattice, and show its distribution in Figure 2.10(c). At high irradiation energies,  $E_{\text{ion}} \geq 1000 \text{ eV}$ , the degree of amorphization reaches values up to 80 % near the surface. A second white line indicates a region in parameter space, in which the amorphization process dominates over the magnetic percolation process and inhibits the emergence of a robust FM phase.

The resulting magnetic phase diagram indicates a narrow region in parameter space, in which a robust artificial ferromagnetic phase can emerge from the creation of defects using low energy ion irradiation. In the next chapter, we show the experimental realization of artificial ferromagnetic materials based on anatase  $\text{TiO}_2$  hosts and check our computational predictions. But first, we shall review some of the experimental evidence of artificial ferromagnetism collected over the past two decades and revisit some of the conclusions based on the physical principles introduced in this chapter.

## 2.6 Revisiting prior experimental results

The computational methods introduced in this chapter not only serve as a predictive scheme to discover artificial ferromagnetic materials in a systematic and efficient way, but can also help to gain a deeper understanding of the experimental results obtained in the past two decades during the development of the field.

In the early days, the first experimental evidence of artificial ferromagnetism due to defects was received with a lot of skepticism, as some groups believed that introducing high amounts of defects into a host material of the order of the percolation threshold would destroy the host lattice and prohibit the emergence of a ferromagnetic ordered phase, which led to wild speculations about the origin of the magnetic signals [17, 49, 50]. Misguided by the established understanding of the mechanisms underlying the intrinsic 3d- and 4f-shell magnetic oxides, various interpretations of the origin of the magnetic signals measured in a wide range of defective non-magnetic host materials fed the controversy [51].

First, the role of magnetic transition metal ions, such as Ni, Co, Mn or Fe, was misinterpreted, as they were believed to be a crucial ingredient for the so-called dilute magnetic semiconductors (DMS). Although such doping could play a role in certain host materials, it was soon realized that these DMS materials were a special case of a much larger class of artificial ferromagnetic materials and that other kinds of point defects, such as vacancies, that carry a magnetic moment could as well lead to the formation of a ferromagnetic phase.

The use of exchange models such as direct or superexchange mechanisms, that were established to explain the magnetic coupling in intrinsic magnetic oxides, led to a crude overestimation of the aforementioned magnetic percolation threshold in defective artificial magnetic oxides: Threshold values as high as 30% were thus assumed [51], which were in strong contradiction to the experimental values, showing ferromagnetic signals at much lower defect concentrations of less than 10%.

Lastly, the small size of the measured ferromagnetic signals in the majority of the experimental reports soon led to doubts about the origin of the signals, questioning the quality of the measurements and the purity of the investigated samples. It was believed that many reports could be explained by the formation of secondary phases of magnetic impurities [51]. The difficulties of estimating the effective volume or mass of the ferromagnetic phases emerging within the host materials made it rather difficult to calculate the magnetization from bulk measurements and most groups simply took the whole sample volume as a reference, which largely underestimated the reported magnetization values.

Although the number of experimental reports of artificial ferromagnetic phases emerging in non-magnetic host materials is incredible, ranging in the thousands of published articles, systematic investigations of the percolation process leading to the emerging artificial ferromagnetic phases are rather scarce. Particle irradiation techniques allow the controlled creation of defects in a host material and can readily be used to measure the magnetic properties as a function of the defect concentration. Few reports of such systematic experimental investigations exist in the literature, but their



results were largely overlooked in the debate described above. In this section, we shall revisit and discuss two of these reports using the theoretical framework introduced in the previous sections of this chapter.

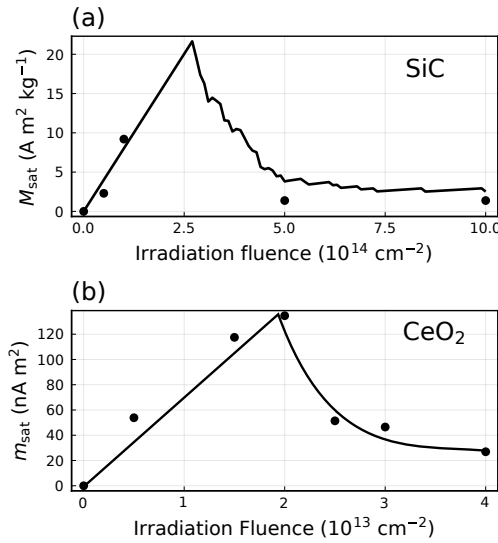


FIGURE 2.11: **Magnetization measurements in SiC and  $\text{CeO}_2$ .** (a) Saturation magnetization of the ferromagnetic signal as a function of the ion irradiation fluence in a 6H-SiC single crystal sample irradiated with  $\text{Ne}^+$  ions at  $E_{\text{ion}} = 140 \text{ keV}$  (data reproduced from [29]); (b) Saturation magnetic moment of a  $\text{CeO}_2$  bulk sample, irradiated with  $\text{Xe}^+$  ions at  $E_{\text{ion}} = 200 \text{ MeV}$  (data reproduced from [28]). The magnetic properties were measured after each irradiation step. The solid line in (a) show the calculated magnetization as described in the text; in (b) the line is just a guide for the eye. All measurements were done at room temperature.

Li et al. [29] reported saturation magnetization values of the ferromagnetic signals emerging in 6H-SiC thin film samples after  $\text{Ne}^+$  ion irradiation at an ion energy of  $E_{\text{ion}} = 140 \text{ keV}$  at fluences up to  $10^{15} \text{ cm}^{-2}$  (see Figure 2.11(a)). The published magnetization data was related to the total film thickness of 460 nm, although the authors estimate the average penetration depth of the ions of only 185 nm. Increasing the ion fluence up to  $10^{14} \text{ cm}^{-2}$ , a steady increase of the ferromagnetic moment at saturation is observed, hinting towards a magnetic percolation process taking place. The authors attribute the emerging ferromagnetic phase to the creation of di-vacancy defect complexes by the ion irradiation. Increasing the ion fluence even more, the magnetic moment at saturation decreases abruptly, which the authors attribute to the amorphization of the host lattice. Similar experimental results were obtained by Wang et al. [52] using  $\text{Xe}$  ions at  $E_{\text{ion}} = 500 \text{ keV}$ . In addition to the bulk magnetometric measurements, the authors reported element specific X-ray absorption and magnetic dichroism (XMCD) results confirming the di-vacancy centers as the source of the emerging ferromagnetic phase. Their role was already predicted by DFT electronic structure calculations [30, 52], which estimated their magnetic moment of  $2 \mu_B$ .

Using MD simulations performed by Li et al. [53] of defect formation

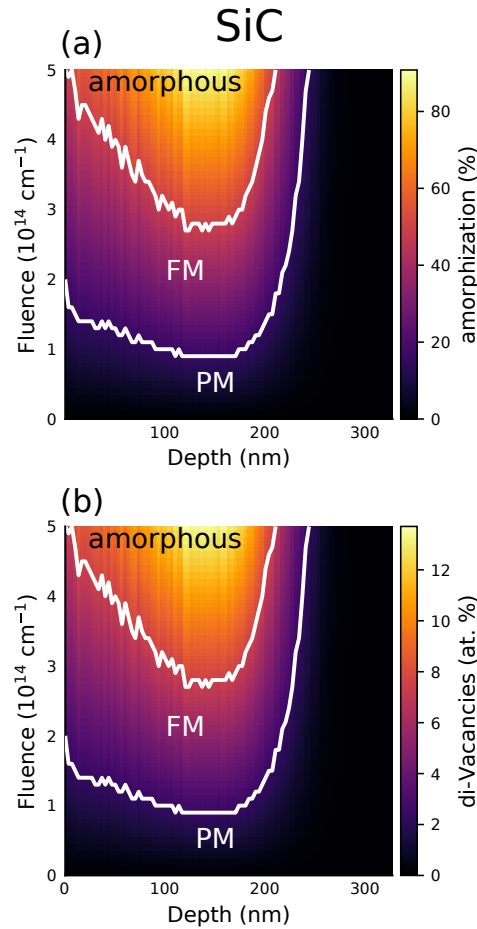


FIGURE 2.12: **Magnetic phase diagram of defective SiC.** The defect distribution created in 6H-SiC by irradiation with  $\text{Ne}^+$  ions at  $E_{\text{ion}} = 140 \text{ keV}$  along the (0001) crystal direction (x-axis) as a function of ion fluence (left axis). The color scales (right axis) indicate the degree of amorphization (a) and di-vacancy defect concentration (b). The white lines separate regions with high enough defect concentration to form a FM phase, with high degree of amorphization (amorphous), with low defect concentration forming a paramagnetic phase (PM) and of pristine host material.

processes during ion irradiation in SiC, we construct a magnetic phase diagram of the emerging ferromagnetic phase following the procedure outlined in the previous sections. Figure 2.12(a) shows the amorphization of the SiC host lattice and Figure 2.12(b) the density of di-vacancies created along the (0001) crystal direction, resulting from the irradiation with  $\text{Ne}^+$  ions at  $E_{\text{ion}} = 140 \text{ keV}$  up to a total fluence of  $5 \times 10^{14} \text{ cm}^{-2}$ . The region delimited by white lines and labeled FM shows the expected emerging ferromagnetic phase. This allows us to get a more realistic estimate of the effective volume of the emerging ferromagnetic phase, which we used to calculate the corrected magnetization values shown in Figure 2.11(a) (left axis). Additionally, taking the calculated magnetic moment of  $2 \mu_B$  per di-vacancy defect and integrating the defect density (Figure 2.12(b)), we can

estimate the expected saturation magnetization of the emerging ferromagnetic phase as a function of the irradiation fluence. This is shown in Figure 2.11(a) as a solid line. We see that the magnetization increases linearly up to a maximum value of  $22 \text{ A m}^2 \text{ kg}^{-1}$  at a fluence of  $\approx 3 \times 10^{14} \text{ cm}^{-2}$ , at which point the amorphization of the host lattice starts to show its effect and the ferromagnetic phase is destroyed in a large region of the sample. This is reflected by a sharp decrease of the magnetization at saturation.

Although magnetization data at the onset of the amorphization of the ferromagnetic phase are missing in the experimental data of Reference [29], the experimental points and the calculated magnetization based on our model match very well. A very similar qualitative behavior is shown in magnetization data obtained by Shimizu et al. [28] in  $\text{CeO}_2$ , irradiated with  $\text{Xe}^+$  ions at  $E_{\text{ion}} = 200 \text{ MeV}$  (Figure 2.11(b)). The authors related the magnetization to the estimated penetration depth of the Xe ions of  $12 \mu\text{m}$ , again leading to an underestimation. For lack of a more accurate knowledge of the magnetic volume, we only show in Figure 2.11(b) the total magnetic moment at saturation  $m_{\text{sat}}$ .

To conclude this chapter, we shall comment on the assumptions and approximations entering the computational scheme. In principle, the techniques introduced in the previous sections can be classified as ab-initio methods: The scheme takes as input the atomic positions of the ideal host structure and the ion irradiation parameters and yields the phase diagram of a possible artificial ferromagnet. In practice, additional inputs are necessary that require some prior knowledge of the host material. Especially the MD simulation step requires effective interatomic pair potentials to model the interactions within the host material and with the incident ions. These potentials have to be provided and tuned to the specific material system. This requirement could be lifted by performing the MD simulations on the level of DFT, where the interactions mediated by the electronic system are calculated by DFT at each MD timestep. Although possible, this method is computationally very expensive and would limit the size of the simulated systems to a few hundred atoms. Therefore, to simulate full collision cascades, especially at high PKA energies, these approximations are necessary. Fortunately, well tested pair potentials exist for a large number of materials and can be retrieved from curated databases [54, 55].

In the next chapter, we will experimentally investigate the emerging artificial ferromagnetic phase in anatase  $\text{TiO}_2$ , in a similar way to the reports discussed in this section, by following the theoretical predictions of the previous section.



## Chapter 3

# Artificial ferromagnetism in TiO<sub>2</sub> hosts

In the previous chapter, we have introduced the physical principles of artificial ferromagnetism due to defects. We have shown how defects created by ion irradiation in non-magnetic host materials can lead to the emergence of a ferromagnetic phase and introduced a computational scheme to discover candidate artificial ferromagnetic materials. Applying this scheme to the TiO<sub>2</sub> host, we constructed a magnetic phase diagram and found that low energy ion irradiation could lead to the magnetic percolation of defects and the emergence of a FM phase.

As outlined in Section 2.6, most experimental accounts of artificial ferromagnetism in the literature compare magnetization measurements of virgin host material samples with those obtained after introducing defects. A systematic investigation of the emergence of the artificial ferromagnetic phase and its evolution in a range of parameters is lacking. In this chapter, we systematically investigate the emergence of a ferromagnetic phase, as predicted in the previous chapter, by irradiating anatase TiO<sub>2</sub> thin films with varying fluences of Ar<sup>+</sup> ions at low energies in the range  $300 \text{ eV} \leq E_{\text{ion}} \leq 1 \text{ keV}$ . The emergence of the ferromagnetic phase is then examined by magnetization measurements using SQUID magnetometry.

For the low energy ion irradiation, specifically at ion energies  $E_{\text{ion}} \leq 1 \text{ keV}$ , we constructed an irradiation setup that we describe in detail in Section 3.1. In Section 3.2, we discuss the experimental methods used to measure the small magnetic signals originating from the ferromagnetic phase. In Section 3.3, we present the experimental realization of an artificial ferromagnet created in TiO<sub>2</sub> hosts by low energy Ar<sup>+</sup> ion irradiation and systematically analyze its properties based on the theoretical predictions of Section 2.5.

### 3.1 Low energy ion irradiation

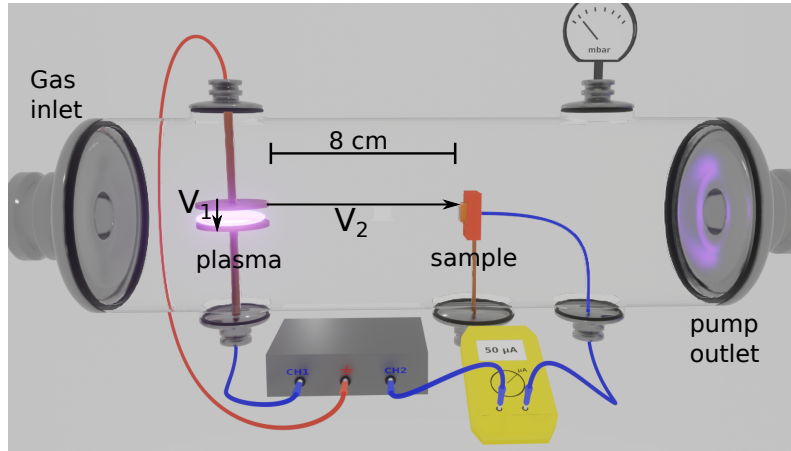


FIGURE 3.1: **Plasma chamber** Sketch of the plasma chamber built for low energy ion irradiation.

For ion irradiation at low energies  $E_{\text{ion}} \leq 1$  keV, we built a remote plasma chamber in parallel plate configuration, that can accelerate plasma ions onto the sample to be irradiated. The chamber is sketched in Figure 3.1 and consists of a sealed glass tube. One end (left side in the sketch) is connected to a driving gas line. The gas flow is controlled by a needle valve. The other end (right side in the sketch) is connected to a rotary pump. Two parallel Cu plates are radially suspended at the center of the chamber, 1 cm apart from each other. One plate (the upper plate in the sketch) is connected to ground, the other is connected to a high voltage source  $V_1$ . The sample holder is placed at a distance of 8 cm downstream from the plates. The sample is placed in a  $0.4 \text{ cm}^2$  Au frame, which is connected to a second high voltage source  $V_2$ . The pressure inside the chamber is measured by a pressure gauge.

When a high negative voltage  $V_1$  is applied across the two plates, at an Ar pressure of  $\sim 10^{-4}$  bar, a Townsend discharge is ignited as electrons are accelerated towards the ground plate and ionize the Ar atoms in the gas, separating the negatively charged electrons and positively charged  $\text{Ar}^+$  ions. The discharge is sustained by the emission of secondary electrons at the negatively biased plate. The ionized gas is heated and a plasma forms upon reaching thermal equilibrium.

The remote plasma serves as an ion source for the irradiation of the sample, placed at a distance of 8 cm from the plates. The negative voltage  $V_2$  accelerates the positively charged  $\text{Ar}^+$  ions onto the sample. The energetic ions hit the sample surface and generate collision cascades. Furthermore, some ions hit the surface of the Au frame surrounding the sample and generate secondary electrons by impact ionization of the Au atoms. The secondary electron current  $I$  is measured in order to estimate the fluence  $f$  of  $\text{Ar}^+$  ions hitting the sample:

$$f(t) = \frac{It}{eA}, \quad (3.1)$$

where  $t$  is the duration of the irradiation process,  $e$  the elementary charge and  $A$  the surface area of the Au frame.

In order to verify the function of the remote plasma setup and to find correct parameters for the irradiation process, we performed plasma simulations using the finite elements methods implemented in the Comsol package. The simulations are performed in three steps. First, the plasma ignition phase is simulated, during which only the negative voltage  $V_1$  is applied. The plasma simulation takes into account four different particle species, namely electrons ( $e^-$ ), neutral Ar atoms, neutral excited Ar atoms (noted  $Ar^*$ ) and positively charged  $Ar^+$  ions, which are coupled by the following impact reactions:

1.  $e^- + Ar \Rightarrow e^- + Ar$  (elastic scattering)
2.  $e^- + Ar \Rightarrow e^- + Ar^*$  (excitation)
3.  $e^- + Ar^* \Rightarrow e^- + Ar$  (relaxation)
4.  $e^- + Ar \Rightarrow 2e^- + Ar^+$  (ionization)
5.  $e^- + Ar^* \Rightarrow 2e^- + Ar^+$  (ionization)
6.  $Ar^* + Ar^* \Rightarrow e^- + Ar + Ar^+$  (relaxation + ionization)
7.  $Ar^* + Ar \Rightarrow Ar + Ar$  (relaxation)

Each impact reaction is described by an energy-dependent reaction cross-section. The cross-section data was retrieved from the LXcat database [56], which contains calculated as well as experimental cross-section data.

At the plates, the following surface reactions were taken into account:

1.  $Ar^+ \Rightarrow Ar$  (neutralization)
2.  $Ar^* \Rightarrow Ar$  (relaxation)

At the negatively biased plate, the emission of secondary electrons was calculated in the neutralization reaction (1). The secondary emission coefficient was set to 0.25 and the mean secondary electron energy was calculated from the mean ion energy and the work function of Cu (4.7 eV).

The Cu electrodes were modeled as metal contacts, and terminated with a ballast resistance of 1 k $\Omega$  to damp the effect of current spikes and allow for a smoother convergence of the plasma potential.

The chamber geometry was discretized using a fine mesh optimized for plasma simulations, resulting in  $\sim 3 \times 10^4$  degrees of freedom to be solved for. The background gas density was treated as an ideal gas and its temperature was set to  $T = 293.15$  K. The pressure  $p$  in the chamber, and the two applied voltages  $V_1$  and  $V_2$  were set up as simulation parameters.

In the initial simulation step, the evolution of the plasma electric potential, electron density and electron energy density were calculated on a coarse mesh during a simulation period of 1 s, at which point their convergence was checked. This allowed to considerably speed up the actual plasma simulations by using the converged potential as a starting point.

In a second step, after the initial plasma ignition was simulated, the negative voltage  $V_2$  was turned up and the system was let to evolve for an



additional period of 1 s, this time on the finer mesh, until reaching convergence. Figure 3.2 shows the resulting ion density at thermal equilibrium in the chamber, at an applied voltage  $V_1 = -800$  V between the plates and  $V_2 = -300$  V at the sample holder. The Ar gas pressure  $p$  was set to 0.1 mbar (panel (a)), 0.15 mbar (panel (b)), 0.2 mbar (panel (c)) and 0.25 mbar (panel (d)). The average ion density in the chamber increases with increasing Ar pressure  $p$  and reaches a maximum ( $2.5 \times 10^{17} \text{ m}^{-3}$  at  $p = 0.25$  mbar) at a distance of 1 cm of the plates and falls off towards the sample. In the region surrounding the negatively biased plate, the positively charged  $\text{Ar}^+$  ions are accelerated towards the plate and are neutralized in the surface reaction (1), while producing secondary electrons. This is reflected by the dark blue area surrounding the lower plate in Figure 3.2 indicating the absence of ions. The electrons emitted from the lower plate are accelerated towards the upper ground plate and ionize neutral atoms in the bulk reactions (4-6). These processes lead to an equilibrium ion distribution within the chamber. Lowering the gas pressure and thereby its density affects the ion density and thereby the charge distribution within the chamber.

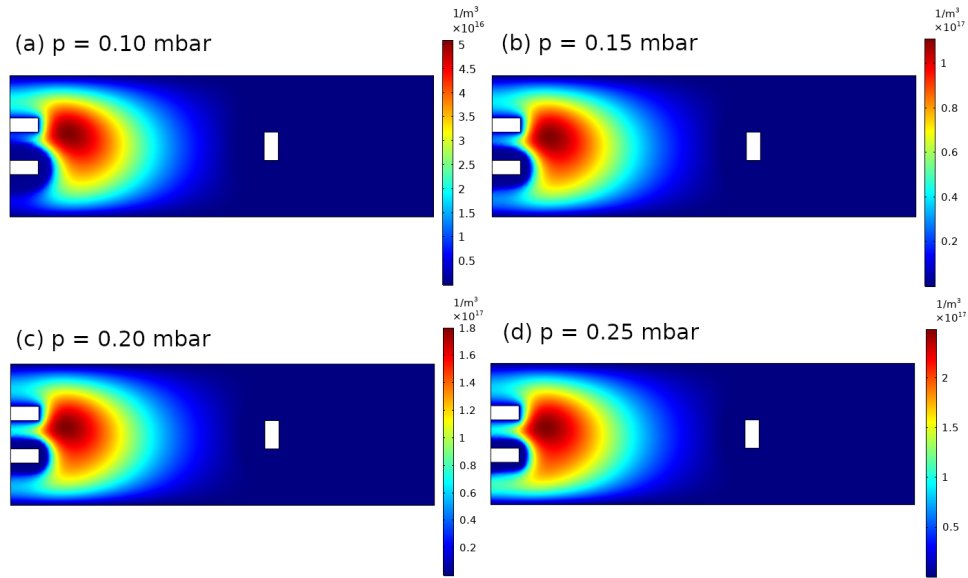


FIGURE 3.2: **Plasma ion density**  $\text{Ar}^+$  ion density in the plasma, calculated by finite elements method as implemented in the Comsol plasma module. The external voltage applied between the plates to the left of the chamber was set to  $-800$  V and the voltage at the sample holder (right white rectangle) was set to  $-300$  V. The color scale indicates the ion density inside the plasma chamber in units of ions/ $\text{m}^3$ . The Ar gas pressure inside the chamber was set to (a) 0.1 mbar, (b) 0.15 mbar, (c) 0.2 mbar and (d) 0.25 mbar.

The charge distribution  $\rho$  within the chamber builds up an electrostatic potential  $V_E$ , that satisfies Poisson's equation:

$$-\nabla^2 V_E = \frac{\rho}{\epsilon_0}. \quad (3.2)$$

Figure 3.3 shows the electric potential calculated at an applied voltage  $V_1 =$

–800 V between the plates and  $V_2 = -300$  V at the sample holder, referenced to ground. The Ar gas pressure  $p$  was set to 0.1 mbar (panel (a)), 0.15 mbar (panel (b)), 0.2 mbar (panel (c)) and 0.25 mbar (panel (d)). A negative potential builds up around the biased plates: At the lower plate, the potential strongly depends on the Ar pressure and reaches  $V_E = -450$  V at  $p = 0.1$  mbar,  $V_E = -380$  V at  $p = 0.15$  mbar,  $V_E = -350$  V at  $p = 0.2$  mbar and  $V_E = -320$  V at  $p = 0.25$  mbar. Furthermore, the electric field  $E = -\nabla V_E$ , increases near the plate with increasing Ar pressure. At the sample holder (right plate) the potential reaches values  $V_E \simeq -280$  V.

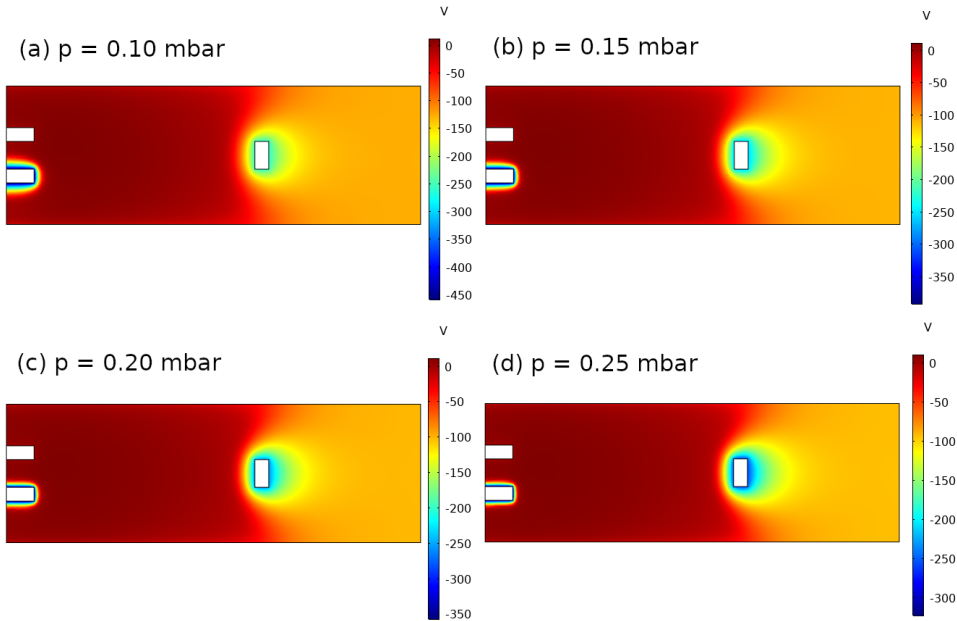


**FIGURE 3.3: Plasma electric potential** Electric potential due to the charge distribution within the plasma, calculated by finite elements method as implemented in the Comsol plasma module. The color scale indicates the potential inside the plasma chamber, referenced to the ground electrode. The external voltage applied between the plates to the left of the chamber was set to  $-800$  V and the voltage at the sample holder (right white rectangle) was set to  $-300$  V. The color scale indicates the ion density inside the plasma chamber in units of  $\text{ions}/\text{m}^3$ . The Ar gas pressure inside the chamber was set to (a) 0.1 mbar, (b) 0.15 mbar, (c) 0.2 mbar and (d) 0.25 mbar.

Once the final ion distribution and electric potential has been converged, the third step consists in calculating trajectories of the ions within the plasma. This is done using the charged particle tracing module, taking into account the electric potential  $V_E$  and elastic scattering between the plasma particles. The trajectories and kinetic energy of  $10^4$  ions, with initial positions sampled from the ion distribution obtained in the previous step, were simulated. The trajectories of those ions intersecting the sample surface are shown in Figure 3.4. They correspond to the plasma calculated at a pressure of 0.2 mbar and applied voltages  $V_1 = -800$  V and  $V_2 = -300$  V. The ion density calculated in the second step is indicated by shades of gray in the background. The colors show the kinetic energy of the particle along

its trajectory according to the scale shown to the right of the figure. Most ions hitting the sample originate from a region 4 cm in front of the sample surface. Ions created further away will likely be accelerated towards the plate and therefore do not reach the sample. The maximum kinetic energy acquired by the ions when hitting the sample is 280 eV.

The plasma parameters accessible experimentally are the external voltages  $V_1$  and  $V_2$ , and the chamber pressure. We are most interested in the effect these parameters have on the ion fluence and energy at the sample surface. Therefore, we performed systematic parameter sweeps and evaluated the resulting ion density and energy as outlined above. As can be seen in Figure 3.2, the ion density and therefore the ion fluence at the sample surface is mostly affected by the pressure inside the chamber. The higher the pressure, the more ions are generated inside the plasma. The ion energy, on the other hand, is not affected much by the Ar pressure.

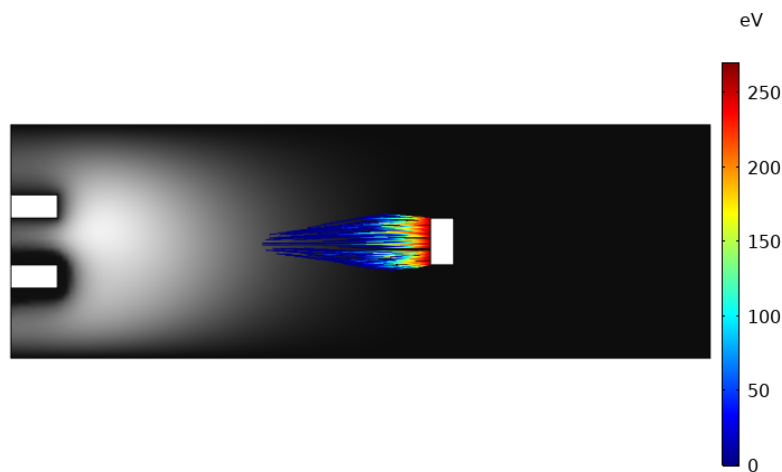


FIGURE 3.4: **Ion trajectories** Trajectories of single  $\text{Ar}^+$  ions hitting the sample surface, simulated using the Comsol charged particle tracing module. A sample of  $10^4$   $\text{Ar}^+$  ions are released according to the ion distribution calculated in the plasma simulation at a pressure of 0.2 mbar and applied voltages  $V_1 = -800$  V between the plates and  $V_2 = -300$  V at the sample holder (see Figure 3.2). The ion trajectories are simulated taking into account the electric potential shown in Figure 3.3 and elastic scattering between plasma particles. The shaded background shows the ion density (as in Figure 3.2(c)) and the colors of the trajectories represent the kinetic energy of the simulated ions (see color bar on the right hand side).

The ion energy is mostly determined by the bias voltage  $V_2$  of the sample holder. The positively charged ions generated in the plasma are accelerated towards the negatively biased sample holder and acquire kinetic energy. The charge distribution within the chamber lowers the electric potential at the sample surface, therefore the kinetic energy reached by the ions hitting the sample has an upper bound determined by the voltage  $V_2$ . The voltage  $V_1$  between the two plates also has an effect on the charge distribution and therefore on the potential within the chamber, although its effect near the sample is less striking than that of the voltage  $V_2$ .

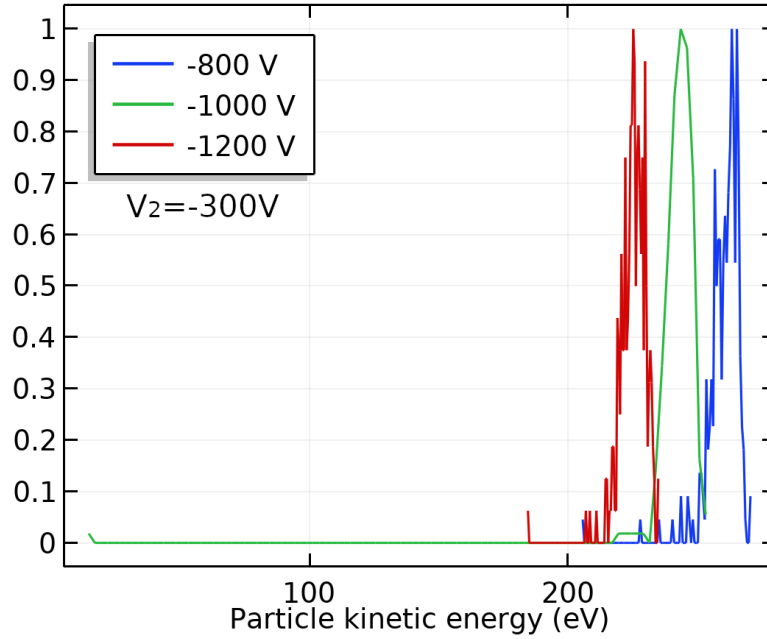


FIGURE 3.5: **Ion energy distribution function** The kinetic energy distribution of ions hitting the sample surface was calculated from the  $10^4$  ion trajectories (see Figure 3.4) using a histogram method, with 100 energy bins uniformly distributed over the full range of ion kinetic energies. The external voltage applied across the two plates was set to  $-800$  V (blue curve),  $-1000$  V (green curve) and  $-1200$  V (red curve). A voltage of  $-300$  V was applied at the sample holder. The kinetic energy is shown on the x-axis and the relative number of ions having this kinetic energy when reaching the sample surface is shown on the y-axis.

From the ion trajectories calculated in the third simulation step, the ion energy distribution function can be obtained using a histogram method. The kinetic energy of each of the simulated ions hitting the sample surface was calculated and a histogram consisting of 100 energy bins was constructed. Figure 3.5 shows the ion energy distribution function of ions hitting the sample surface in a plasma generated at a pressure  $p = 0.15$  mbar and a sample voltage  $V_2 = -300$  V. The energy distribution at three different values of the applied voltage between the plates  $V_1 = -800$  V,  $-1000$  V and  $-1200$  V is shown. The ion energy distribution functions resulting from the simulations show narrow peaks around the average ion energy with a full width at half maximum of  $\sim 5$  eV.

The simulations show that the lower the voltage between the plates, the more the ion energy approaches the ideal value corresponding to the electric potential applied at the sample holder, i.e. 300 eV. At  $V_1 = -1200$  V, the mean ion kinetic energy is  $\langle E_{\text{ion}} \rangle = 220$  eV, at  $V_1 = -1000$  V it is  $\langle E_{\text{ion}} \rangle = 250$  eV and at  $V_1 = -800$  V, it is  $\langle E_{\text{ion}} \rangle = 280$  eV. On the other hand, if the voltage applied between the plates is too low, the plasma simulation does not converge and no plasma is ignited in the first place.

Figure 3.6 shows the ion energy distribution functions calculated at a voltage  $V_2 = -500$  V at the sample holder and  $V_1 = -800$  V,  $-1000$  V and  $-1200$  V across the plates. There, the mean kinetic energy of the ions is

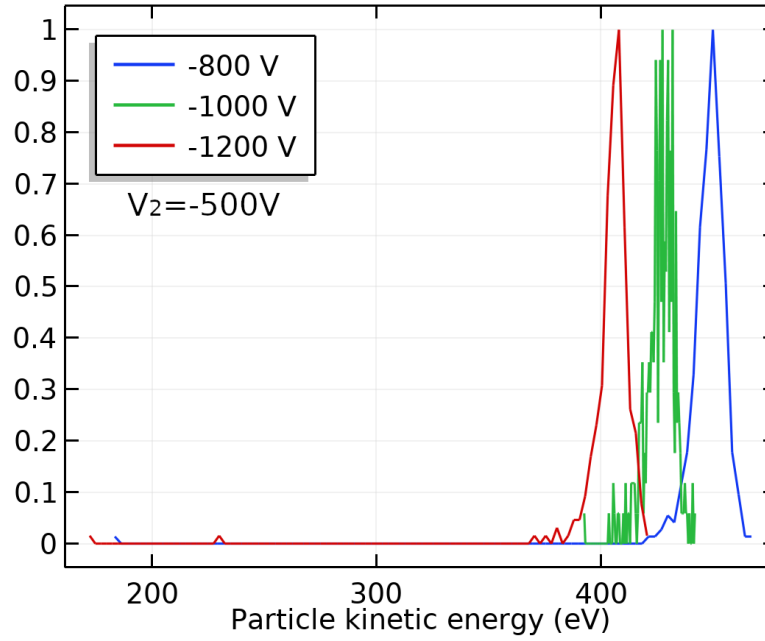


FIGURE 3.6: **Ion energy distribution function** The kinetic energy distribution of ions hitting the sample surface was calculated from the  $10^4$  ion trajectories (see Figure 3.4) using a histogram method, with 100 energy bins uniformly distributed over the full range of ion kinetic energies. The external voltage applied across the two plates was set to  $-800$  V (blue curve),  $-1000$  V (green curve) and  $-1200$  V (red curve). A voltage of  $-500$  V was applied at the sample holder. The kinetic energy is shown on the x-axis and the relative number of ions having this kinetic energy when reaching the sample surface is shown on the y-axis.

equal to 410 eV at an applied voltage across the plates of  $V_1 = -1200$  V, at  $V_1 = -1000$  V it is 430 eV and at  $V_1 = -800$  V, it is 450 eV.

Figure 3.7 shows the ion energy distribution functions calculated at a voltage  $V_2 = -1000$  V at the sample holder and  $V_1 = -1200$  V,  $-1400$  V and  $-1600$  V across the plates. At lower voltages, the plasma did not converge properly. The calculated kinetic energy distribution shows a mean value at 800 eV at an applied voltage across the plates of  $V_1 = -1600$  V. At  $V_1 = -1400$  V, the mean kinetic energy is equal to 830 eV and at  $V_1 = -1200$  V, it is 850 eV.

Although the plasma simulations fail at low voltages  $V_1$  between the plates, experimentally, we observe a considerable current density of the order of  $1 \text{ A m}^{-2}$  flowing between the two plates at voltages as low as  $V_1 = 500$  V and Ar gas pressures ranging from  $p = 0.5$  mbar down to  $p = 0.05$  mbar. The current flowing between the two plates indicates the presence of a large number of mobile charge carriers in the plasma. When applying an acceleration voltage  $V_2$  between the grounded plate and the sample holder, a current can be measured flowing through the sample holder, indicating that charge carriers reach the sample surface and secondary electrons are emitted from the Au frame on the sample holder. The current density typically measured at the sample holder is of the order of  $0.1 \text{ A m}^{-2}$ .

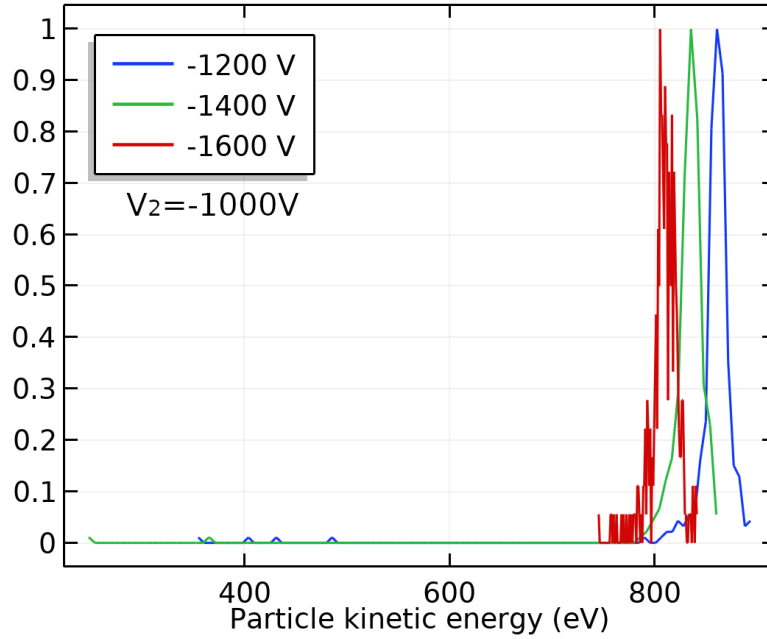


FIGURE 3.7: **Ion energy distribution function** The kinetic energy distribution of ions hitting the sample surface was calculated from the  $10^4$  ion trajectories (see Figure 3.4) using a histogram method, with 100 energy bins uniformly distributed over the full range of ion kinetic energies. The external voltage applied across the two plates was set to  $-1200$  V (blue curve),  $-1400$  V (green curve) and  $-1600$  V (red curve). A voltage of  $-1000$  V was applied at the sample holder. The kinetic energy is shown on the x-axis and the relative number of ions having this kinetic energy when reaching the sample surface is shown on the y-axis.

Assuming a secondary electron emission parameter of 0.25, i.e. one secondary electron is emitted every fourth ion impact, this corresponds to an ion flux of  $2.5 \times 10^{14} \text{ cm}^{-2} \text{ s}^{-1}$ . This allows to control the ion fluence by measuring the current through the Au frame on the sample holder and the irradiation duration.

In the following, we will refer to the nominal ion energy  $E_{\text{ion}} = c_{\text{ion}} V_2$ , i.e. the kinetic energy that the  $\text{Ar}^+$  ions of charge  $c_{\text{ion}} = +e$  acquire in the electric potential  $V_2$ . But we should keep in mind that the actual kinetic energy of the ions can deviate from this nominal value by up to 20% (Figures 3.5, 3.6, 3.7).

### 3.2 SQUID magnetometry

In order to measure the magnetic signals originating from an emerging ferromagnetic phase induced by defects in a non-magnetic host material, high sensitive magnetometry techniques are required. Especially at the onset of magnetic percolation, the expected magnetic signals are very small. Superconducting quantum interference device (SQUID) magnetometry is the most common technique for the characterization of these magnetic materials, owing to its high sensitivity and the availability of commercial turn-key magnetic property measurement system (MPMS) solutions, such as the MPMS-XL7 from Quantum Design used in this work. Nevertheless, much care has to be taken when characterizing artificial ferromagnets, as the magnetic signals can easily reach the detection limit of commercial SQUID magnetometers. In this section, the measurement principle is introduced and guidelines for high sensitivity measurements are discussed.

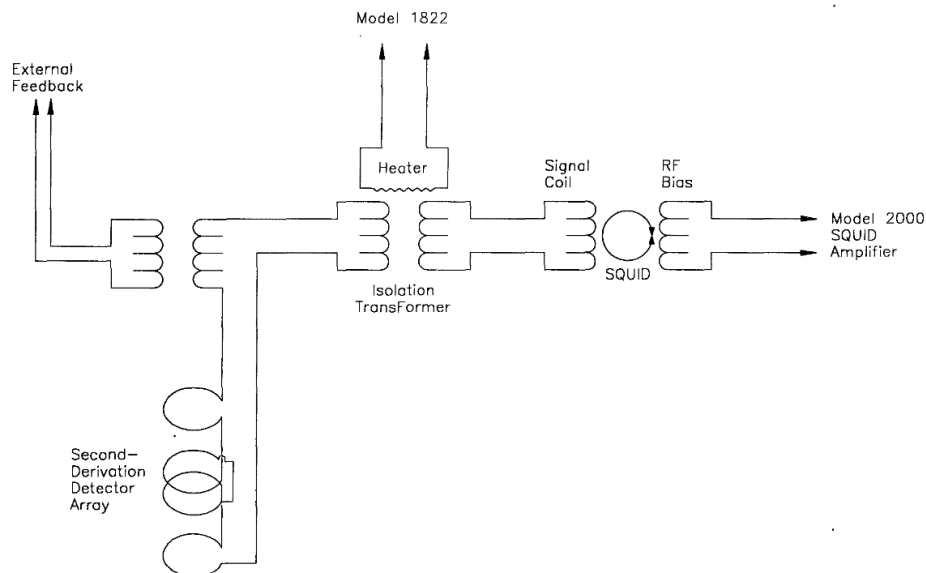


FIGURE 3.8: **Sketch of the MPMS-XL SQUID detection system.** It shows the main components of the magnetometer measurement circuitry: The second-order gradiometer (lower left) consisting of an array of four pickup coils is inductively coupled to the SQUID through the isolation transformer. The RF SQUID signal is amplified and demodulated to produce the raw measurement data. Adapted from [57].

The detection unit in most commercial MPMS nowadays consists of three parts: the SQUID is made up of a superconducting loop with a single (RF SQUID) or two (DC SQUID) Josephson junctions. When a supercurrent flows, the voltage drop across the junction depends on the difference  $\Delta\varphi$  of the phases of the superconducting wavefunctions on each side of the junction, which in turn depends on the magnetic flux  $\Phi$  penetrating the loop. Therefore, the SQUID translates magnetic flux to electrical voltage. The so-called tank circuit is made up of superconducting pickup coils configured as a second order gradiometer, as depicted in the lower left part of



Figure 3.8. Two outer loops are wound in opposite direction to the two inner loops. A magnetic field  $B(z) = B_0 + B_1z$ , threading the coils induces a current inside the outer loops which is canceled by an opposite current induced in the inner loops. A small magnetic source placed within the gradiometer, on the other hand, induces a net current in the tank circuit. The pickup coils are inductively coupled to the SQUID circuit, which is isolated from the magnetic environment by superconducting shielding. A heater is mounted on the isolation transformer, allowing to drive it into normal state and release trapped flux prior to each measurement. The RF SQUID setup implemented in the MPMS XL is driven with an external RF bias current and the resulting voltage is amplified and demodulated.

The gradiometer is wrapped by a superconducting solenoid, which in the case of the MPMS XL-7 can produce magnetic fields up to 7 T along the longitudinal axis of the gradiometer. The whole assembly is placed in a  $\text{He}_4$  cryostat and the temperature inside the sample space is controlled in order to allow the sample to be cooled down to 2 K or heated up to 390 K.

During a measurement, the sample is driven across the pickup coils while recording the SQUID voltage as a function of the sample position. This data is the raw signal produced by the MPMS and is then translated by software to the total magnetic moment of the sample using an analytical model. A significant improvement in the sensitivity of the measurement can be achieved using the reciprocating sample oscillation (RSO) mode, where the sample oscillates up and down and produces an alternating magnetic flux in the coils, leading to an alternating output voltage. The frequency of the readout is then locked to the frequency of the oscillating sample.

The magnetic sample is mounted on a rod, that can be moved up and down in the pickup coil arrangement by a stepper motor. Prior to the actual measurement, the exact sample position, relative to the central windings has to be determined. The sample reference frame is determined by a centering scan, during which the sample is scanned through the whole coil assembly while applying an external magnetic field. Depending on the magnetic properties of the sample, a maximum (para- or ferromagnetic sample) or minimum SQUID voltage (diamagnetic sample) is reached when the sample is placed inside the inner loops of the pickup coil. If the response of the sample to the external magnetic field is too weak, the sample position can not be determined in this way. Then, a paramagnetic marker placed at the exact position of the sample on the sample holder can be used to calibrate the sample reference frame.

As stated above, the pickup coil assembly is setup as a second order gradiometer and is sensitive to magnetic fields that are non-linear along the gradiometer axis. This means that the external magnetic field, which is assumed to be homogeneous throughout the sample space, is not measured. As the stray field of a magnetic point dipole falls off as  $1/r^3$  at a distance  $r$ , magnetic fields originating from sources far away from the gradiometer are highly damped. On the other hand, magnetic fields originating from small sources within the gradiometer volume strongly affect the measurement. Besides the sample to be investigated, other sources of magnetic fields have to be eliminated in order to reduce the background signal and improve the sensitivity of the measurement.



The presence of magnetic particles near the sample can be one source of background signal, that can not be neglected. Therefore, when measuring samples with small magnetic signals, it is especially important to avoid any contamination of the sample space. The sample and sample holder should only be handled with special non-magnetic tools to avoid a contamination from, e.g., metallic tweezers. In addition, the sample needs to be mounted on a non-magnetic support, that does not contribute to the measurement. This is usually done by clamping the sample inside a long plastic drinking straw. Although the straw may have a small diamagnetic response to an external magnetic field, this response does not affect the measurement, as long as it is homogeneous and the straw is longer than the pickup coil assembly. Using a plastic straw as the sample holder also has the advantage that a typical square thin film sample can easily be oriented with respect to the external field, i.e. the field can be applied in plane or out of plane, as shown in Figure 3.9. When clamping the sample inside the straw, much care has to be taken, as every deformation of the straw leads to a local perturbation in the straw response that will be picked up by the SQUID.

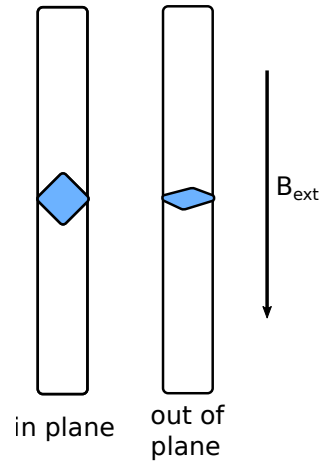


FIGURE 3.9: **SQUID sample holder.** Especially for thin film samples grown on a square substrate, a plastic drinking straw is a convenient support, as explained in the text. The square sample is clamped inside the straw and is held in place at two opposite corners. This way, the sample can be rotated freely around the clamping axis to measure configurations, where the external magnetic field  $B_{\text{ext}}$  is applied in plane and out of plane.

By default, the MPMS software models the magnetic sample as a point dipole and fits the total magnetic moment of the sample to the raw SQUID voltage:

$$V(z) = V_0 + V_1 z + V_2 \left[ \frac{2}{(R^2 + (z + \delta z)^2)^{3/2}} - \frac{2}{(R^2 + (z + \delta z + \Lambda)^2)^{3/2}} - \frac{2}{(R^2 + (z + \delta z - \Lambda)^2)^{3/2}} \right], \quad (3.3)$$

where  $V_0$  and  $V_1$  are fitting parameters accounting for drifts in the SQUID voltage during the scan,  $R$  and  $\Lambda$  are the radius and the separation of the

pickup coils,  $\delta z$  is a fitting parameter accounting for a misalignment of the sample w.r.t the center coils. The fitting parameter  $V_2$  is then translated to a magnetic moment using a device dependent calibration factor, that has to be determined using a sample of known magnetic moment. The approximation of the sample to a point dipole is good enough in many cases, especially when the sample is spherical and small. Therefore, the MPMS software performs the fitting procedure automatically and saves the resulting magnetic moment in the main data file. When measuring small signals, it is useful to analyze the raw signals manually and assess the quality of the measurement.

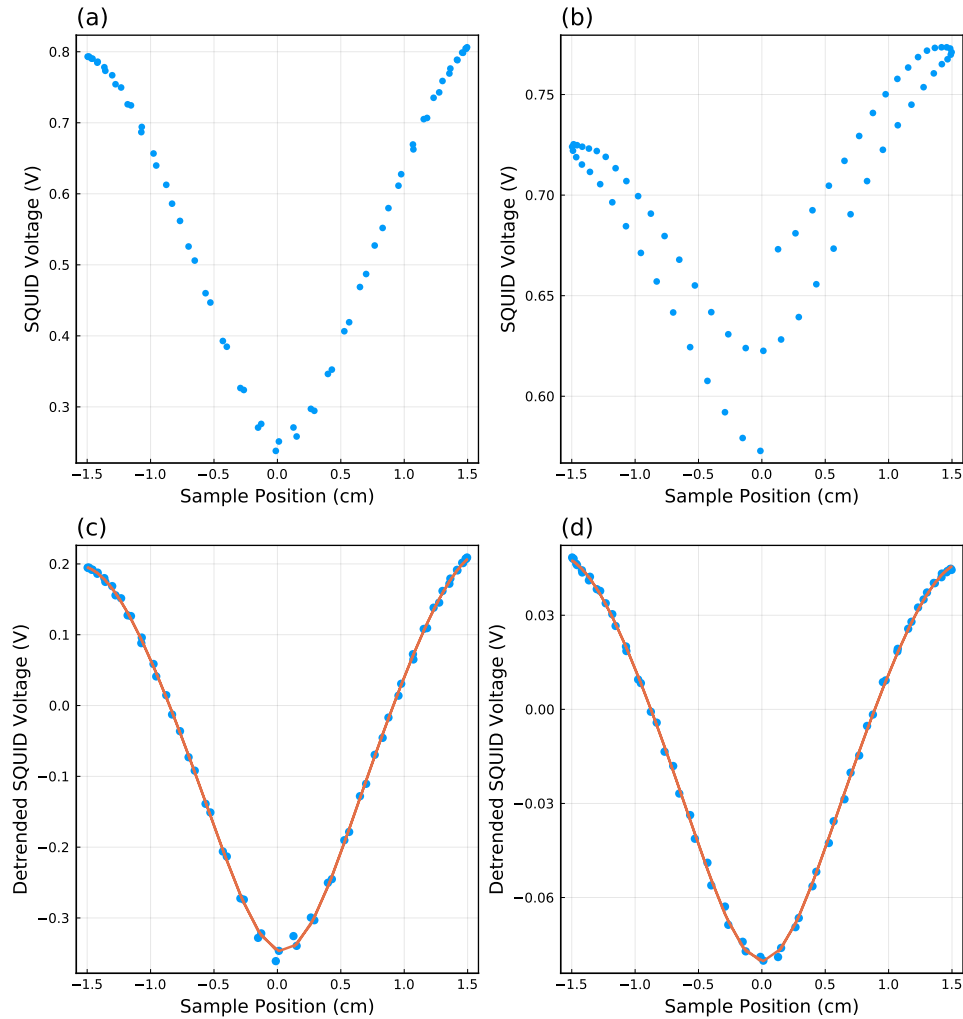


FIGURE 3.10: **Raw SQUID voltage.** The upper panels show typical measurements of the raw SQUID voltage response as a function of the magnetic sample position, obtained in the RSO mode. Prior to the measurement, the sample reference frame has been centered at the inner pickup coil position. The measurement shown on the right (b,d) has a large drift in the SQUID voltage, compared to the measurement shown on the left (a,c). The lower panels show the same data, corrected for the SQUID drift. The line shows the fit resulting from Equation (3.3).

Figure 3.10 shows a typical measurement obtained by scanning a diamagnetic sample across the SQUID pickup coils. The SQUID voltage is plotted as a function of the sample position relative to the central windings of the coil. An external magnetic field of 2 kOe was applied in the positive direction of the pickup assembly. The response of the diamagnetic sample opposes the external field and the signal measured by the SQUID therefore shows a minimum when the sample is placed inside the central winding, at  $z = 0$  in the sample reference frame. The measurement was performed in the RSO mode, in which the sample scan starts at the center of the pickup coil assembly, is scanned symmetrically about the origin in a predefined range (here 3 cm) and back to the center. During the scan, a total of 64 positions are recorded. The scan range has to be set in such a way that the sample does not leave the volume of homogeneous external magnetic field. Otherwise, at least for a ferromagnetic sample, a change of the external magnetic field could affect the magnetization state of the sample. On the other hand, the scan range should be large enough to measure not only the response of the central windings, but also that of the outer loops. Ideally, the sample should be brought close enough to each loop during the scan to induce a sizable magnetic flux through the loops. As the flux induced by a magnetic moment  $m$  falls off as  $m/r^3$  at distance  $r$ , the scan range has to be optimized for each sample.

In Figure 3.10(a), the raw SQUID voltage recorded on the way up coincides with that measured on the way down. This is not always the case, as shown in Figure 3.10(b), where the SQUID voltage has a drift which can be due to electronic drift in the SQUID or amplifier circuits. This drift has to be corrected for, in order to fit Equation (3.3) to the voltage data. The drift correction can be achieved by fitting a line to the raw voltage data. As the drift is usually not position dependent, and in the RSO mode the scan direction is not continuous in time, the voltage measurement has to be expressed as a function of time first. As the time is not recorded for each scan point, the data can be referenced to a continuous row index, assuming the measurement duration of each scan position is the same. The corrected voltage signal, the so-called detrended voltage, is shown in the lower panels of Figure 3.10. The solid lines show the resulting best fits of Equation (3.3).

When measuring samples with a geometry that significantly deviates from the spherical point dipole approximation, such as very thin magnetic films, it can be necessary to correct for the sample geometry to get an accurate magnetic moment measurement. Figure 3.11 shows the detrended SQUID voltage resulting from two scans of the same diamagnetic sample with dimensions  $5 \text{ mm} \times 5 \text{ mm} \times 0.5 \text{ mm}$  and same applied magnetic field  $B_{\text{ext}} = 2 \text{ kOe}$ , once with the sample normal oriented along the gradiometer axis (blue) and perpendicular to it (orange). The resulting magnetic moments deviate by  $\sim 5 \%$ , although the sample is purely diamagnetic and should not show any magnetic anisotropy. The simple point dipole model (Equation (3.3)) used by the MPMS software can not account for the sample geometry and therefore a more complete model has to be derived. We start with a single magnetic point dipole with dipole moment  $\vec{m}$  at the position  $\vec{r}_d$  and want to calculate the magnetic flux  $\Phi_B$  induced by the dipole through a coil winding of radius  $\rho_0$ , parallel to the  $xy$ -plane and whose center is positioned at  $\vec{r}_c$ . We use cylindrical coordinates with unit vectors  $(\hat{\rho}, \hat{\varphi}, \hat{z})$  to describe the system and define the relative position between dipole and

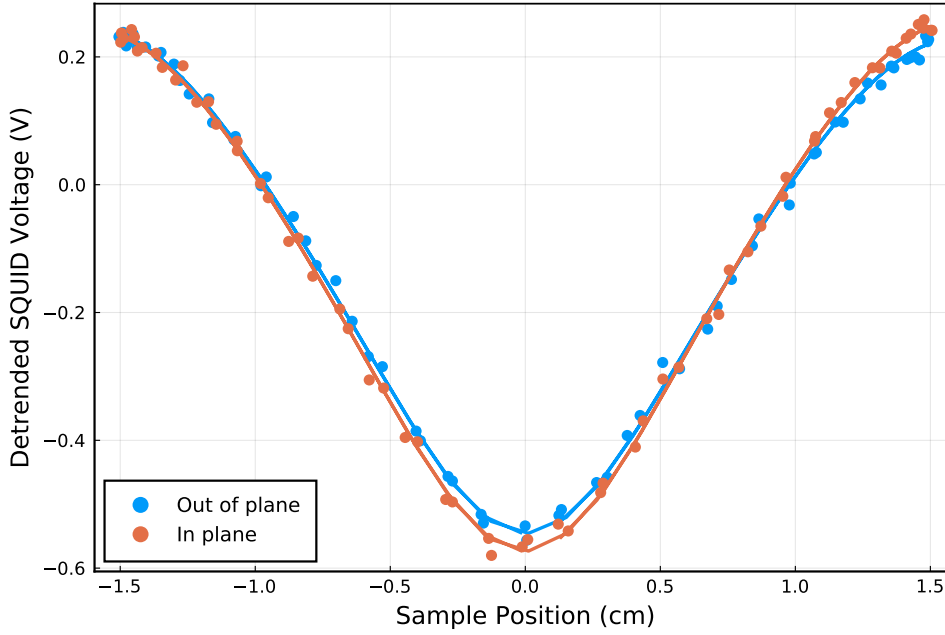


FIGURE 3.11: **Sample geometry corrections.** The fitting procedure of the MPMS system software assumes a sample geometry that can be approximated by a magnetic point dipole. When this approximation does not hold, the real geometry has to be taken into account in order to reduce the fitting error.

coil  $\vec{r}_r = \vec{r}_c - \vec{r}_d$  (see Figure 3.12).

The scalar dipole potential is defined as

$$\phi_m(\vec{r}_r) = \frac{\vec{m} \cdot \vec{r}_r}{4\pi|\vec{r}_r|^3} = \frac{1}{4\pi} \frac{\rho_m \rho_r \cos(\varphi_r - \varphi_m) + z_m z_r}{(\rho_r^2 + z_r^2)^{3/2}}, \quad (3.4)$$

from which we can calculate the stray magnetic field emitted by the dipole:

$$\vec{B}_m(\vec{r}_r) = -\mu_0 \nabla \phi_m(\vec{r}_r). \quad (3.5)$$

In cylindrical coordinates, the gradient transforms as

$$\nabla f = \frac{\partial f}{\partial \rho} \hat{\rho} + \frac{1}{\rho} \frac{\partial f}{\partial \varphi} \hat{\varphi} + \frac{\partial f}{\partial z} \hat{z} \quad (3.6)$$

and with

$$\begin{aligned} \frac{\partial \phi_m}{\partial \rho_r} &= \frac{1}{4\pi} \frac{\rho_m (z_r^2 - 2\rho_r^2) \cos(\varphi_r - \varphi_m) - 3z_m \rho_r z_r}{(\rho_r^2 + z_r^2)^{5/2}}, \\ \frac{\partial \phi_m}{\partial \varphi_r} &= \frac{1}{4\pi} \frac{\rho_m \rho_r \sin(\varphi_m - \varphi_r)}{(\rho_r^2 + z_r^2)^{3/2}}, \\ \frac{\partial \phi_m}{\partial \varphi_r} &= \frac{1}{4\pi} \frac{z_m (\rho_r^2 - 2z_r^2) - 3\rho_m \rho_r z_r \cos(\varphi_r - \varphi_m)}{(\rho_r^2 + z_r^2)^{5/2}}, \end{aligned} \quad (3.7)$$

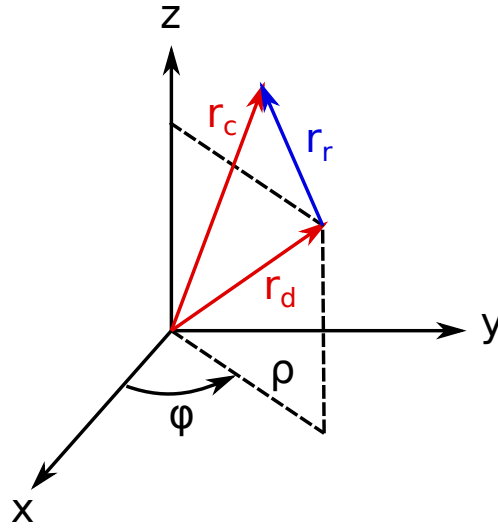


FIGURE 3.12: **Coordinate system** used to calculate the sample geometry correction factors for the raw SQUID voltage fitting procedure.

we obtain

$$\vec{B}_m = \frac{\mu_0}{4\pi (\rho_r^2 + z_r^2)^{3/2}} \left[ \frac{\rho_m (z_r^2 - 2\rho_r^2) \cos(\varphi_r - \varphi_m) - 3z_m \rho_r z_r}{(\rho_r^2 + z_r^2)} \hat{\rho}_r + \rho_m \sin(\varphi_m - \varphi_r) \hat{\varphi}_r + \frac{z_m (\rho_r^2 - 2z_r^2) - 3\rho_m \rho_r z_r \cos(\varphi_r - \varphi_m)}{(\rho_r^2 + z_r^2)} \hat{z}_r \right]. \quad (3.8)$$

The magnetic flux through the coil winding enclosing the surface  $S$  is then

$$\Phi_B = \int_S \vec{B}_m \cdot d\vec{A}_c, \quad (3.9)$$

with the surface element

$$d\vec{A}_c = \hat{z}_c \rho_c d\rho_c d\varphi_c. \quad (3.10)$$

This yields the following integral for the magnetic flux through a single coil winding:

$$\Phi_B = \frac{\mu_0}{4\pi} \int_0^{\rho_0} \int_{-\pi}^{\pi} \frac{\rho_c (\rho_r^2 - 2z_r^2) z_m - 3\rho_c \rho_r z_r \cos(\varphi_r - \varphi_m) \rho_m}{(\rho_r^2 + z_r^2)^{5/2}} d\varphi_c d\rho_c, \quad (3.11)$$

with

$$\begin{aligned} \rho_r &= \sqrt{\rho_c^2 + \rho_d^2 - 2\rho_c \rho_d \cos(\varphi_c - \varphi_d)} \\ \varphi_r &= \arctan \left[ \frac{\rho_c \sin(\varphi_c) - \rho_d \sin(\varphi_d)}{\rho_c \cos(\varphi_c) - \rho_d \cos(\varphi_d)} \right] \\ z_r &= z_c - z_d. \end{aligned} \quad (3.12)$$

Due to the form of  $\varphi_r$ , the integral in Equation (3.11) becomes intractable

and we won't be able to solve it analytically. Looking at the special case of a magnetic dipole  $\vec{m} = (0, 0, m_z)$ , oriented along the gradiometer axis and positioned at its center along the  $\hat{z}$  axis ( $\vec{r}_d = (0, 0, z_d)$ ), we find

$$\begin{aligned}\Phi_B &= \int_0^{\rho_0} \int_{-\pi}^{\pi} \frac{\mu_0 m_z \rho_c (2(z_c - z_d)^2 - \rho_c^2)}{4\pi ((z_c - z_d)^2 + \rho_c^2)^{5/2}} d\varphi_c d\rho_c \\ &= \frac{\mu_0 m_z}{2} \frac{\rho_0^2}{((z_c - z_d)^2 + \rho_0^2)^{3/2}},\end{aligned}\quad (3.13)$$

and retrieve the simple dipole model Equation (3.3) used by the MPMS software, with  $\rho_0 = R$  and  $z_c = 0, \pm\Lambda$ .

To see how a small misalignment  $\vec{r}_d = (\rho_d, 0, z_d)$  of the magnetic dipole  $\vec{m} = (0, 0, m_z)$  off the central gradiometer axis affects the magnetic flux through the coils, we expand the integrand in Equation (3.11) in a power series about  $\rho_d = 0$  up to second order:

$$\begin{aligned}\vec{B} \cdot d\vec{A}_c &\approx \frac{\mu_0 m_z}{4\pi} \left[ \frac{2(z_c - z_d)^2 \rho_c - \rho_c^3}{((z_c - z_d)^2 + \rho_c^2)^{5/2}} \right. \\ &\quad - \frac{3\rho_c^2 (2z_c - 2z_d + \rho_c)(-2z_c + 2z_d + \rho_c) \cos(\varphi_c)}{((z_c - z_d)^2 + \rho_c^2)^{7/2}} \rho_d \\ &\quad \left. + \frac{3\rho_c (-4z_r^4 - 3z_r^2 \rho_c^2 + \rho_c^4 - 5\rho_c^2 (-6z_r^2 + \rho_c^2) \cos(\varphi_c)^2)}{2((z_c - z_d)^2 + \rho_c^2)^{9/2}} \rho_d^2 \right] d\varphi_c d\rho_c.\end{aligned}\quad (3.14)$$

Integration of the power series yields a second order correction to the flux:

$$\Phi_B \approx \frac{\mu_0 m_z}{2} \left[ \frac{\rho_0^2}{((z_c - z_d)^2 + \rho_0^2)^{3/2}} + \frac{3(\rho_0^2 - 4(z_c - z_d)^2) \rho_0^2}{4((z_c - z_d)^2 + \rho_0^2)^{7/2}} \rho_d^2 \right]. \quad (3.15)$$

Near the central windings, where the sample produces maximum magnetic flux through the coil assembly, and  $z_c \approx z_d$ , the misalignment  $\rho_d$  of the sample off the central axis of the gradiometer increases the flux by a factor  $\sim \rho_d^2/\rho_0^3$ . This explains the different magnetic moments obtained from the two measurements shown in Figure 3.11. The sample geometry can not well be approximated by a point dipole and its orientation in the gradiometer matters.

To calculate the finite size effect of the sample, we need to integrate the magnetization over the whole sample volume  $V$ . Assuming the magnetization is homogeneous in the sample volume, we can express it as

$$\vec{M}(\vec{r}_M) \equiv (\rho_M, \varphi_M, z_M) = \frac{\vec{m}}{V} \quad (3.16)$$

We can then write the magnetic flux through a coil winding due to the sample of volume  $V$ :

$$\Phi_B(V) = \frac{\mu_0}{4\pi} \int_V \left\{ \int_0^{\rho_0} \int_{-\pi}^{\pi} \left[ \frac{\rho_c (\rho_r^2 - 2z_r^2) z_M}{(\rho_r^2 + z_r^2)^{5/2}} - \frac{3\rho_c \rho_r z_r \cos(\varphi_r - \varphi_M) \rho_M}{(\rho_r^2 + z_r^2)^{5/2}} \right] d\varphi_c d\rho_c \right\} \rho_d d\rho_d d\varphi_d dz_d \quad (3.17)$$

We calculate the finite size effect of a sample of dimension  $5 \text{ mm} \times 5 \text{ mm} \times 0.5 \text{ mm}$  with a total magnetic moment of 1 emu on the total magnetic flux through the gradiometer, by numerically integrating Equation (3.17). Figure 3.13 shows the resulting total magnetic flux when the sample is placed with the surface normal parallel to the  $z$ -axis (“Out of plane”) and parallel to the  $x$ -axis (“In plane”). The solid lines correspond to the fit using Equation (3.3), yielding values proportional to the magnetic moment  $m_{\perp}$  ( $m_{\parallel}$ ) that would be calculated by the MPMS software. By comparing these values, we find a deviation of

$$\frac{m_{\parallel} - m_{\perp}}{m_{\parallel}} \times 100 = 4.81\%. \quad (3.18)$$

which is close to the deviation of 4.95 % obtained from the measurements shown in Figure 3.11. Comparing the effective moments  $m_{\parallel}$  and  $m_{\perp}$  mea-

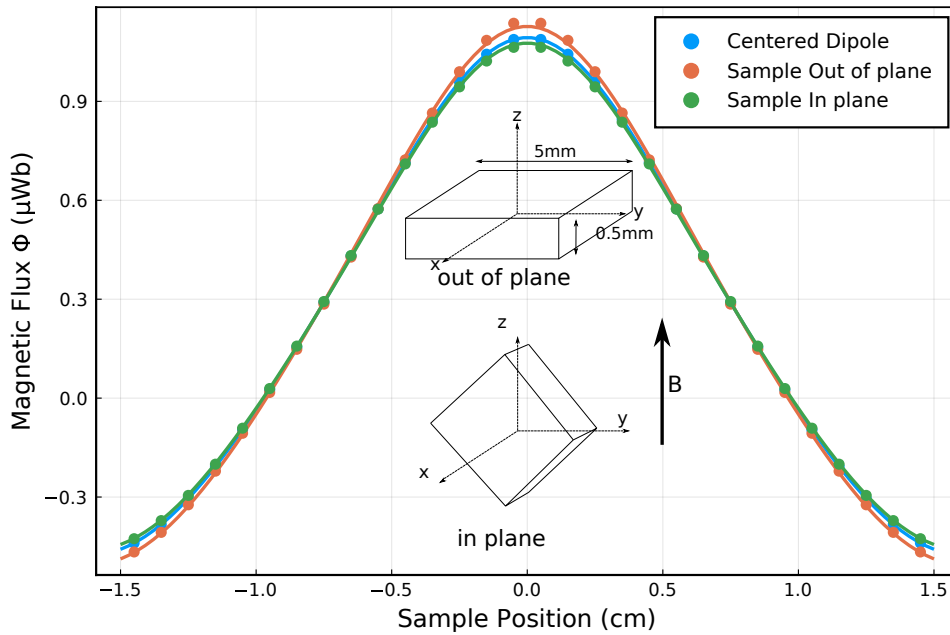


FIGURE 3.13: **Finite sample size effect** on the magnetic flux through the pickup coil assembly of the MPMS gradiometer, as a function of the  $z$ -position along the gradiometer axis, calculated for an axially centered magnetic dipole (blue), and for the two samples sketched in the inset.

sured by the MPMS software and the real total moment of the sample, we can calculate correction factors for the finite size effect of a specific sample geometry. Table 3.1 shows the resulting correction factors. To correct

the magnetic moment  $m_{\text{MPMS}}$  calculated by the MPMS software, one has to multiply by the finite size correction factor ( $m_{\text{corr}} = m_{\text{MPMS}} * C_{\text{fs}}$ ).

Sample Geometry $X \times Y \times Z$ (mm)	Correction factor ( $C_{\text{fs}}$ )
$5 \times 5 \times 0.5$	0.969296
$0.5 \times 5 \times 5$	1.015966

TABLE 3.1: Correction factors  $C_{\text{fs}}$  for the finite sample size effects on the magnetic moment calculated by the MPMS software for samples of relevant geometry and orientation for this work.

All corrections, fitting algorithms and data processing functionalities outlined in this section have been implemented in the Julia programming language and used to analyze the SQUID magnetometry measurement data throughout this work.



### 3.3 Experimental realization of an artificial ferromagnet in TiO<sub>2</sub>

Following the predictions of an artificial ferromagnetic phase emerging in anatase TiO<sub>2</sub>, due to the percolation of defects created by low energy ion irradiation (Section 2.5), a systematic experimental investigation of the magnetic percolation process is in order. Using the experimental methods described in the previous sections, a set of three anatase TiO<sub>2</sub> thin film samples were incrementally irradiated with small steps of ion fluence, each with a nominal ion energy of  $E_{\text{ion}} = 200$  eV, 500 eV and 1000 eV, respectively. After each irradiation step, the magnetic properties of the samples were measured, using SQUID magnetometry, in order to follow the percolation process and detect the emergence and evolution of the artificial ferromagnetic phase.

The TiO<sub>2</sub> thin film samples were prepared in two steps: First, 40 nm thin amorphous TiO<sub>2</sub> films were deposited on  $5 \times 5 \times 0.5$  mm<sup>3</sup> LaAlO<sub>3</sub> (100) substrates by ion beam sputter deposition, from a Ti target at an O<sub>2</sub> background pressure of  $1.5 \times 10^{-5}$  mbar and Ar ions with an energy of 1000 eV and a scattering angle of 110°. The details of the growth process are described in Ref [58]. In a second step, the amorphous films crystallized in the anatase phase by post-growth annealing in air at a temperature  $T = 500^\circ$  C for 1 h.

The Ar<sup>+</sup> ion irradiation parameters, specifically the chamber pressure and temperature, Ar gas flow, the voltages  $V_1$  between the parallel plates and  $V_2$  at the sample holder (see Section 3.1) were chosen, such that the three samples were irradiated with comparable ion fluences and ion energies spanning the region of the magnetic phase diagram (Figure 2.10), where the emergence of an artificial ferromagnetic phase is expected. The irradiation parameters used for the three samples are shown in Table 3.2.

Sample name	TiO <sub>2</sub> 200	TiO <sub>2</sub> 500	TiO <sub>2</sub> 1000
Chamber pressure (mbar)	$2.5 \times 10^{-2}$	$2.5 \times 10^{-2}$	$2.5 \times 10^{-2}$
Chamber temperature (K)	293	293	293
Ar partial pressure (mbar)	0.12	0.12	0.12
$V_1$ (V)	-1000	-1000	-1000
$V_2$ (V)	-200	-500	-1000
$I_1$ (mA)	2.5	2.5	2.5
$I_2$ ( $\mu$ A)	2.5	8	20

TABLE 3.2: Irradiation parameters used for the three TiO<sub>2</sub> thin film samples.  $V_1$  and  $I_1$  are the voltage and current flowing through the parallel plates and  $V_2$ ,  $I_2$  are the voltage (referenced to the ground plate) and current at the sample holder.

After each irradiation step, the total magnetic moment of the samples were measured using SQUID magnetometry and the fitting procedure outlined in Section 3.2, as a function of the applied magnetic field in the range -5 T to 5 T at constant temperature  $T = 300$  K, the so-called magnetic hysteresis loops, and as a function of temperature at a constant applied magnetic field. Before each hysteresis loop measurement, the magnetization of the sample was reset by applying a sequence of magnetic field oscillations, with decreasing amplitude  $B_{i+1} = -\frac{1}{\sqrt{2}}B_i$ , starting at  $B_0 = 1$  T, as shown

in Figure 3.14, followed by a reset of the remnant field in the superconducting solenoid, performed by driving the superconducting wire into normal state and quenching the magnet coil. This procedure allows to start each hysteresis loop measurement at zero field and zero magnetization of the samples.

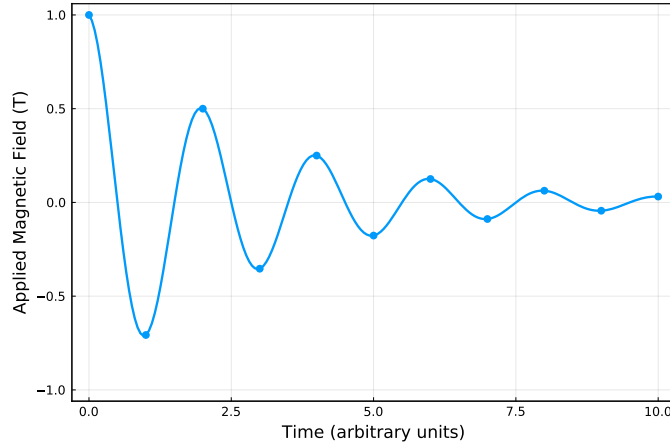


FIGURE 3.14: **Magnetization reset sequence.** To reset the magnetization of the sample, a sequence of magnetic fields with oscillating amplitude is applied.

Figure 3.15(a) shows two examples of raw hysteresis curves, measured at  $T = 300$  K after the sample  $\text{TiO}_2$ 1000 had been irradiated with a total  $\text{Ar}^+$  ion fluence of  $0.6 \times 10^{16} \text{ cm}^{-2}$  and  $8.7 \times 10^{16} \text{ cm}^{-2}$ , respectively, at a nominal ion energy of 1000 eV. The first observation is that the sample reacts to an applied magnetic field with an opposing magnetization, which is a signature for diamagnetic behavior. In addition to the linear in field diamagnetic response of the sample, a small non-linear hysteretic response is clearly visible and grows with increasing ion fluence. To emphasize this non-linear response, the high field response is fit to a line and subtracted from the total signal. The remainder of the signal, after subtraction of the linear diamagnetic contribution, is shown in Figure 3.15(b). The signals have the shape of a ferromagnetic hysteresis loop. As the measurement started in a state of zero magnetization after applying the oscillating field sequence (Figure 3.14), the so-called virgin curve is visible, starting at the origin. Increasing the applied magnetic field, the magnetic moment increases rapidly and finally saturates at the saturation moment  $m_{\text{sat}}$ . Reversing the magnetic field, the magnetic moment decreases again. But instead of returning to a state of zero magnetic moment when the external field is turned off, the sample shows a remnant moment  $m_{\text{rem}}$ . Only when a negative field  $B_c$ , the coercive field, is applied, the magnetic moment of the sample returns to zero. The hysteresis loop continues symmetrically upon reversing the magnetic field at the negative saturation regime.

The hysteresis loops showing increasing saturation moments  $m_{\text{sat}}$  upon ion irradiation are a signature of the artificial ferromagnetic phase, emerging in the  $\text{TiO}_2$  host due to the percolation of paramagnetic defects. According to the simulations of the percolation process (see Figure 2.3), at defect concentrations below the percolation threshold, the sample should be

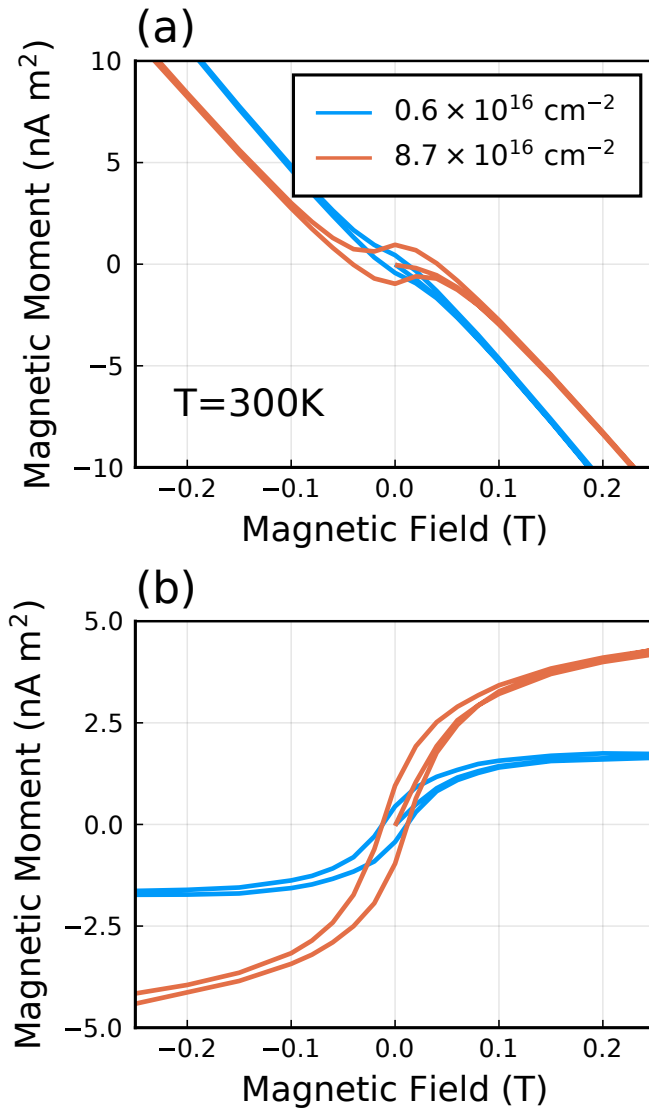


FIGURE 3.15: **Hysteresis loops of  $\text{TiO}_2$  artificial ferromagnet**, measured at  $T = 300\text{ K}$ . (a) Total magnetic moment as a function of the applied magnetic field, measured after sample  $\text{TiO}_21000$  had been irradiated with a fluence of  $0.6 \times 10^{16}\text{ cm}^{-2}$  (blue) and  $8.7 \times 10^{16}\text{ cm}^{-2}$  (orange). (b) Same as (a), but with the linear diamagnetic contribution to the total magnetic moment subtracted to emphasize the ferromagnetic hysteresis.

paramagnetic. At high temperature and moderate magnetic field, a paramagnet shows a magnetization that evolves linearly with applied magnetic field with a positive slope. Due to the diamagnetic contribution, which is also linear in field (but with a negative slope), the paramagnetic contribution can not easily be isolated from the room temperature hysteresis loops. Therefore, the magnetic moment was also measured as a function of the sample temperature at a constant applied magnetic field.

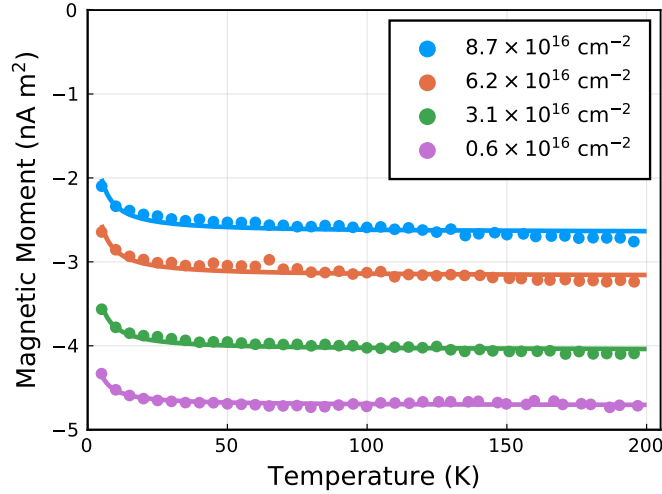


FIGURE 3.16: **Temperature dependence of the magnetic moment.** Total magnetic moment of sample TiO<sub>2</sub>1000, measured as a function of temperature while cooling the sample from  $T = 300$  K down to  $T = 5$  K at an applied magnetic field of  $B = 0.1$  T, after the sample was irradiated with a fluence of  $0.6 \times 10^{16} \text{ cm}^{-2}$ ,  $3.1 \times 10^{16} \text{ cm}^{-2}$ ,  $6.2 \times 10^{16} \text{ cm}^{-2}$  and  $8.7 \times 10^{16} \text{ cm}^{-2}$ . The solid lines show fits to Equation (3.20).

Figure 3.16 shows the temperature dependence of sample TiO<sub>2</sub>1000 after it was irradiated with a fluence of  $0.6 \times 10^{16} \text{ cm}^{-2}$ ,  $3.1 \times 10^{16} \text{ cm}^{-2}$ ,  $6.2 \times 10^{16} \text{ cm}^{-2}$  and  $8.7 \times 10^{16} \text{ cm}^{-2}$  at a constant applied magnetic field  $B = 0.1$  T. The total magnetic moment is negative, owing to the diamagnetic contribution dominating the measured signal. The offset between the curves reflects the increasing ferromagnetic contribution to the total magnetic moment, as the irradiation fluence increases. At the applied magnetic field, the ferromagnetic contribution is saturated. As the sample is cooled down, the total magnetic moment increases. This temperature dependence is mostly due to the contribution of isolated paramagnetic defects.

Assuming the total magnetic moment of the sample is composed of a diamagnetic  $m_{\text{dia}}$ , a paramagnetic  $m_{\text{para}}$  and a ferromagnetic  $m_{\text{fm}}$  contribution, such that

$$m_{\text{total}} = m_{\text{dia}} + m_{\text{para}} + m_{\text{fm}}, \quad (3.19)$$

and at high applied magnetic field, the temperature dependence of the paramagnetic moment follows a Brillouin function:

$$m_{\text{para}}(T) = VN g \mu_B J B_J(g \mu_B J B / k_B T), \quad (3.20)$$

with

$$B_J(x) = \frac{2J+1}{2J} \coth\left(\frac{2J+1}{2J}x\right) - \frac{1}{2J} \coth\left(\frac{x}{2J}\right), \quad (3.21)$$

where  $\mu_B$  is the Bohr magneton,  $k_B$  the Boltzmann constant,  $\mu = gJ\mu_B$  the microscopic magnetic moment of the paramagnetic defects,  $V$  the sample volume and  $N$  the density of isolated paramagnetic defects in the sample.

The solid lines in Figure 3.16 show the fit of Equation (3.20), with  $N \sim 10^{14} \text{ cm}^{-3}$  paramagnetic defects having a magnetic moment of  $2\mu_B$  in the as-grown samples. The defect concentration slightly increases when the samples are irradiated.

At high temperature and moderate magnetic field, the magnetic moment due to the isolated paramagnetic defects can be approximated by Curie's law:

$$m_{\text{para}} = V \frac{C B}{\mu_0 T}, \quad (3.22)$$

where  $C$  is the material specific Curie constant

$$C = \frac{\mu_0 \mu_B^2}{3k_B} N g^2 J(J+1). \quad (3.23)$$

And therefore,  $m_{\text{para}}$  is linear in magnetic field. Under the assumption that the diamagnetic contribution to the total magnetic moment,  $m_{\text{dia}}$ , which is also linear in magnetic field, does not considerably change when irradiating the samples, the linear in magnetic field contribution to the total magnetic moment at room temperature can also be used to estimate the change in concentrations of the isolated paramagnetic defects due to the irradiation. By comparing the slope, or rather the magnetic susceptibility  $\chi = M/H$ , of the linear in field contribution to the total magnetic moment,  $\chi_{\text{linear}}(f) = \chi_{\text{dia}} + \chi_{\text{para}}(f)$ , as the samples are irradiated with increasing ion fluence  $f$ , to the susceptibility of the as-grown sample, the variation of the defect density  $N$  is obtained as shown in Figure 3.17. First, the slope of the as-grown sample is subtracted

$$\Delta\chi = \chi_{\text{linear}}(f) - \chi_{\text{linear}}(0) = \chi_{\text{para}}(f) - \chi_{\text{para}}(0) \quad (3.24)$$

and then, the defect concentration is calculated from the difference  $\Delta\chi$ , assuming an affected volume  $V$  corresponding to the penetration depth of the ions during the irradiation, (see Figure 2.10).

Figure 3.17 shows the change in number density of isolated paramagnetic defects, referenced to the densities of the as-grown samples. The number of isolated paramagnetic defects created during the irradiation first increases up to a maximum value ( $10^{15} \text{ cm}^{-3}$  in sample TiO<sub>2</sub>200,  $5 \times 10^{14} \text{ cm}^{-3}$  in sample TiO<sub>2</sub>500 and  $5 \times 10^{13} \text{ cm}^{-3}$  in sample TiO<sub>2</sub>1000) and then goes back down to zero, increasing the total fluence. This behavior is expected considering the magnetic percolation model and the calculations shown in Figure 2.3(b). As the number of paramagnetic defects created by ion irradiation increases, percolation domains start to form. Those defects belonging to a percolation domain no longer contribute paramagnetically to the total magnetic moment of the sample. As shown in Figure 2.3(b), the dimensions of the magnetic layer have an influence on the percolation process and a larger maximum is in fact expected for thinner magnetic layers. From the calculations of the irradiation damage (Figure 2.10), the ion penetration depth in the three samples correspond to 1,2 and 3 TiO<sub>2</sub> unit cells, respectively. The maximum number of defects contributing paramagnetically to the total magnetic moment of the sample reflects this dependence

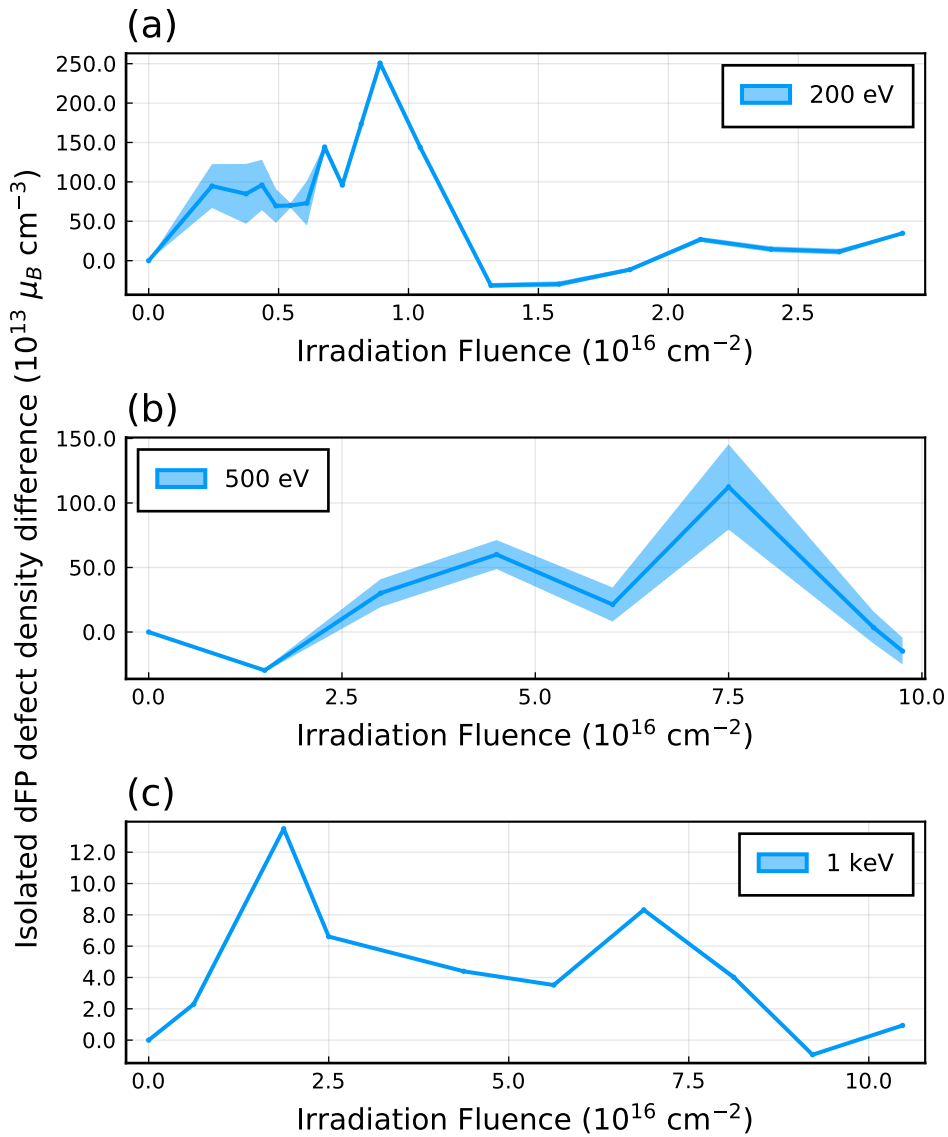


FIGURE 3.17: **Evolution of isolated paramagnetic defects.** The density of isolated paramagnetic defects are calculated from the change  $\Delta\chi$  of the paramagnetic susceptibility at room temperature compared to the as-grown samples, using Curie's law (Equation (3.22)), taking into account the volume of the sample affected by the ion irradiation. The relative concentration of isolated paramagnetic defects in sample (a)  $\text{TiO}_2$ 200, (b)  $\text{TiO}_2$ 500 and (c)  $\text{TiO}_2$ 1000 is shown as a function of the total irradiation fluence. The ribbons indicate confidence margins at 5% significance level.

quite well.

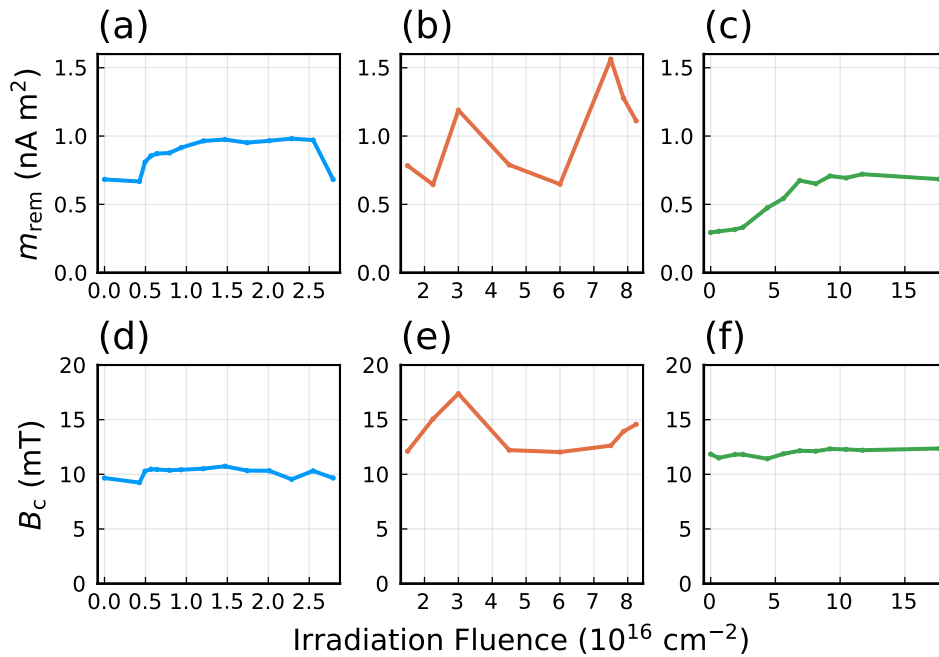


FIGURE 3.18: **Ferromagnetic hysteresis parameters.** Remnant magnetic moment (a-c) and coercive field (d-f) measured in the three TiO<sub>2</sub> thin film samples after each irradiation step. The columns show results for the samples irradiated at (a,d)  $E_{\text{ion}} = 200$  eV (b,e) 500 eV and (c,f) 1000 eV.

Upon increasing the irradiation fluence, percolation domains start to grow and their constituent defects are expected to contribute ferromagnetically to the total magnetic moment of the sample and explains the appearance of a ferromagnetic hysteresis loop. Figure 3.18 shows the evolution of the remnant magnetic moment  $m_{\text{rem}}$  at zero field and the coercive field of the three samples as a function of the irradiation fluence. With increasing irradiation fluence, the remnant magnetic moment also increases. This can be explained by the deterioration of the crystal lattice due to irradiation damage, which increases the pinning of magnetic domain walls during the magnetization reversal. Domain wall pinning is a clear signature of long-ranged ferromagnetic order. Although this behavior should also be reflected by an increase of the coercive field, this parameter is much more difficult to measure with high precision and therefore no significant change of the coercive field as a function of the irradiation fluence is apparent from the measurements.

Figure 3.19 shows the magnetic moment at saturation,  $m_{\text{sat}}$ , of the ferromagnetic signal measured after each irradiation step. As expected, the magnetic moment first increases with each step and saturates at high ion fluence. One major issue in all previous reports of artificial ferromagnetism was the uncertainty in the magnetic volume and mass, which is needed to calculate the magnetization. The lack of accurate magnetization values makes it very difficult to compare artificial ferromagnets with the intrinsic ones and to assess their usability. The phase diagram calculated in the previous chapter (Figure 2.10) helps here. In TiO<sub>2</sub>, the artificial ferromagnetic

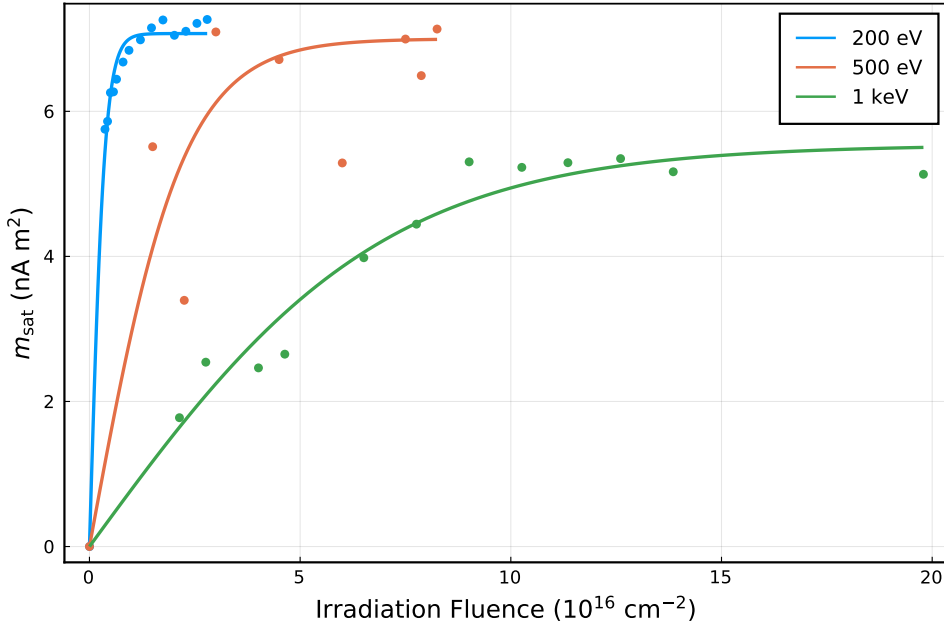


FIGURE 3.19: **Experimental observation of magnetic percolation.** Magnetic moment at saturation of the ferromagnetic signal, measured at room temperature as a function of the ion irradiation fluence, in the three TiO<sub>2</sub> thin film samples, irradiated with Ar<sup>+</sup> ions at  $E_{\text{ion}} = 200$  eV,  $E_{\text{ion}} = 500$  eV and  $E_{\text{ion}} = 1000$  eV. The magnetic properties were measured after each irradiation step. The lines show the best fits to Equation (3.25).

phase emerging at the experimental ion irradiation parameters is clearly confined to a thin region near the film surface. This prediction perfectly agrees with the experimental evidence and is the main reason for the existence of a perpendicular magnetic anisotropy [34], as discussed in more detail in the next chapter. The maximum magnetization obtained by taking into account the expected magnetic volume in each of the samples is summarized in Table 3.3 and reaches a value up to  $79 \text{ A m}^2 \text{ kg}^{-1}$ , which is as large as that reported for bulk magnetite (Fe<sub>3</sub>O<sub>4</sub>,  $M_s = 90 \text{ A m}^2 \text{ kg}^{-1}$ ) [59].

Knowing the magnetic volume and the magnetic moment of a single defect (e.g.  $2 \mu_B$  for the dFP), one can also calculate the defect concentration corresponding to the experimentally observed magnetization, see Table 3.3. In the irradiated TiO<sub>2</sub> thin films, the dFP concentration reaches almost 20 at.%, which is far beyond the aforementioned magnetic percolation threshold. It should be noted that the resulting defect concentration appears to decrease increasing the irradiation energy  $E_{\text{ion}}$  and thereby the ion penetration depth. As will be discussed in the next chapter, the presence of the surface has a great influence on the magnetic structure of the defects and therefore has to be taken into account when defects are created at low ion energies.

In the artificial ferromagnet created in the anatase TiO<sub>2</sub> host by ion irradiation, the theoretical predictions outlined in Section 2.5 showed that two processes mainly determine the limits of the emerging FM phase, namely the creation of dFP and oxygen vacancy defects and the amorphization of



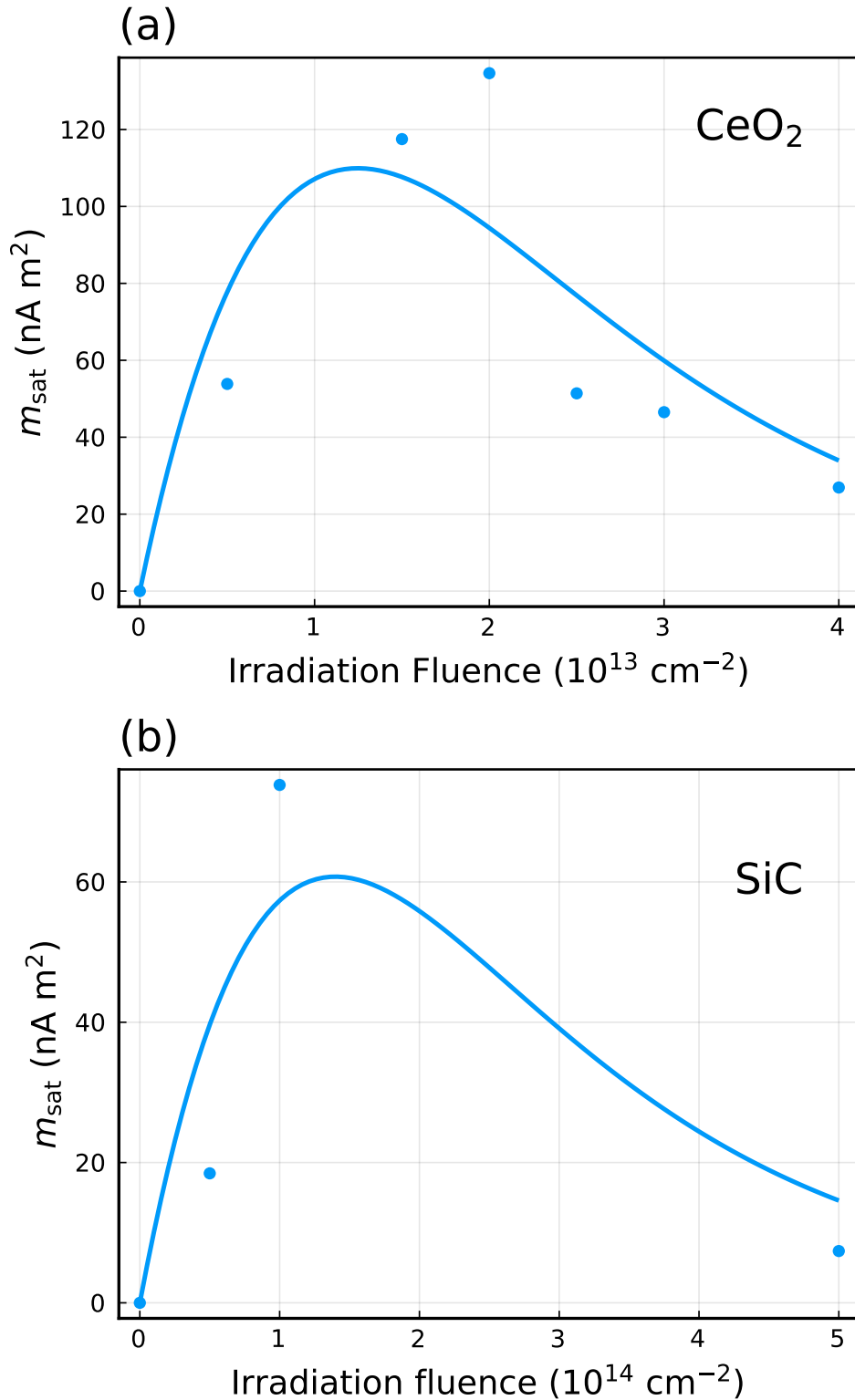


FIGURE 3.20: **Magnetic percolation in  $\text{CeO}_2$  and  $\text{SiC}$  based artificial ferromagnets.** Magnetic moment at saturation of (a) a  $\text{CeO}_2$  bulk sample, irradiated with  $\text{Xe}^+$  ions at  $E_{\text{ion}} = 200 \text{ MeV}$  (data reproduced from [28]) and (b) a 6H-SiC single crystal sample irradiated with  $\text{Ne}^+$  ions at  $E_{\text{ion}} = 140 \text{ keV}$  (data reproduced from [29]). The magnetic properties were measured after each irradiation step. The lines show the best fits to Equation (3.25).

Host	$E_{\text{ion}}$ (eV)	$M_{\text{sat}}$ (A m <sup>2</sup> kg <sup>-1</sup> )	Defects (at.%) <sup>‡</sup>	$\delta$
TiO <sub>2</sub>	200	79	19 (dFP)	1.01
TiO <sub>2</sub>	500	74	18 (dFP)	1.00
TiO <sub>2</sub>	1000	56	13 (dFP)	0.99
CeO <sub>2</sub>	$2 \times 10^8$	46*	10* (V <sub>O</sub> )	0.20
SiC	$1.4 \times 10^5$	20*	9.5* (divacancy)	0.28
Fe <sub>3</sub> O <sub>4</sub> †	–	90	–	–

TABLE 3.3: Experimentally determined magnetization at saturation, magnetic defect concentration, as well as the ratio  $\delta = \beta/\gamma$  of the two process rates obtained as fit parameters from Equation (3.25). (\*): The magnetization and defect concentration of the CeO<sub>2</sub> and SiC samples were corrected as described in the text. †: The magnetization of bulk magnetite is shown for comparison to a typical intrinsic FM. ‡: The defect concentration refers to all defects of that kind, including those that are isolated and do not contribute to the FM signal.

the host matrix. One other process that plays an important role at the surface of the sample is the sputtering of amorphous material during the irradiation. At large enough ion fluence, one would expect a large degree of amorphization in the irradiated sample and the FM phase to vanish. In reality, amorphous material is removed at the surface, permitting the ions to penetrate deeper into the sample and leading to a steady state between the magnetic defect creation and amorphization processes. This explains the stability of the FM phase even at an ion fluence as high as  $2 \times 10^{17}$  cm<sup>-2</sup>. In comparison, magnetization data obtained by Shimizu et al. [28] by irradiating CeO<sub>2</sub> samples with high energy ( $E_{\text{ion}} = 200$  MeV) Xe<sup>+</sup> ions (Figure 3.20(a)) and data obtained by Li et al. [29] by irradiating SiC samples with Ne<sup>+</sup> ions at  $E_{\text{ion}} = 140$  keV (Figure 3.20(b)) show a different behavior: there, the magnetization reaches a maximum at an ion fluence of  $2 \times 10^{13}$  cm<sup>-2</sup> (CeO<sub>2</sub>) and  $1 \times 10^{14}$  cm<sup>-2</sup> (SiC) and vanishes at higher fluence. Li et al. attribute the disappearance of the FM phase at high fluence to the amorphization of the host material.

The evolution of the FM phase with the ion fluence  $f$  can be described qualitatively by a rate equation for a constructive and a destructive process, resulting in

$$m_{\text{sat}}(f) = \alpha \frac{\exp(\beta f) - \exp(-\gamma f)}{\exp(-\beta f) + \exp(\gamma f)}, \quad (3.25)$$

with the rates  $\beta$  and  $\gamma$  of the two processes and a scaling parameter  $\alpha$ . Ideally, the ratio  $\delta = \beta/\gamma$  should be larger than one, so that the magnetic percolation process outweighs the destructive processes. This is almost the case for the TiO<sub>2</sub> samples (see Table 3.3).

It should be noted that for the CeO<sub>2</sub> and SiC samples, the authors calculate a magnetization taking into account the whole sample volume, in which the ions penetrate (with a penetration depth of 12  $\mu\text{m}$  in CeO<sub>2</sub> [28] and 460 nm in SiC). The origin of the magnetic signal in CeO<sub>2</sub> is attributed to the creation of oxygen vacancies and in SiC to pairs of Si and O divacancies, which carry a magnetic moment of  $2\mu_B$ . Considering the results of

the calculations for  $\text{TiO}_2$  and SiC (see Section 2.5 and Section 2.6), this assumption is not realistic, as it completely ignores destructive effects of the irradiation. Furthermore, for the  $\text{CeO}_2$  sample, the magnetization obtained under this assumption would translate to an oxygen vacancy concentration of merely 0.03 at.% or a defect separation of more than 4 nm, and for the SiC sample to a divacancy concentration of 0.4 at.% or a defect separation of 1.4 nm, at which the emergence of a FM phase at room temperature is impossible. Assuming a more realistic separation between the defects of 5 Å and using the computational results obtained for SiC in Section 2.6, the actual magnetic layer is much thinner (32 nm in the  $\text{CeO}_2$  sample and 20 nm in the SiC sample), and the resulting magnetization turns out to be of the same order of magnitude as that observed in  $\text{TiO}_2$  (see Table 3.3).

The proximity of the FM phase emerging in the  $\text{TiO}_2$  thin film hosts to the sample surface obviously plays an important role and explains the evolution of the magnetization as a function of the irradiation fluence, that differs from the observations in  $\text{CeO}_2$  and SiC hosts shown above. Due to the low ion energies used in this work to irradiate the  $\text{TiO}_2$  thin film samples, the region affected by the irradiation is much thinner. Following the theoretical predictions of Section 2.5, the emerging FM phase is expected to be of the order of a few monolayers of the host lattice. This has fundamental implications for the stability of the ordered phase and the magnetic percolation process. In the next chapter, we discuss these implications and investigate the dimensionality effects and the effect of the surface on the emerging artificial FM phase in  $\text{TiO}_2$  thin film hosts.



## **Chapter 4**

# **Artificial magnetic monolayers and surface effects**

## 4.1 Critical behavior and 2D magnetism

In Section 2.4, we introduced the magnetic percolation process, which describes a second order geometrical phase transition. We defined the order parameter  $P_\infty$  as the probability that a random defect belongs to the percolation continent. Its critical behavior near the phase transition follows a power law with a critical exponent  $\beta$  (Equation (2.22)). As we have seen in the previous chapter, the artificial FM phase emerging in anatase TiO<sub>2</sub> hosts upon ion irradiation follows such a percolation process. We shall now take a look at the critical behavior of the magnetic percolation process.

At high applied magnetic fields, all percolation domains contribute to the total magnetization. Therefore, even below the percolation threshold, where no ferromagnetic percolation continent has emerged yet, a non-zero saturating magnetization can be measured at moderate applied magnetic fields. The sample is super-paramagnetic. On the other hand, only the ferromagnetic percolation continent can show a spontaneous magnetization. Hence, a remanent magnetization only starts to appear at the percolation threshold.

This allows us to estimate the irradiation fluence necessary to create a defect concentration of the order of the percolation threshold, as shown in Figure 4.1 (b). For the sample TiO<sub>2</sub>200, this threshold fluence is  $f_c = 4.9 \times 10^{15} \text{ cm}^{-2}$  and for sample TiO<sub>2</sub>1000, we find  $f_c = 1.8 \times 10^{16} \text{ cm}^{-2}$  (see also Table 4.1). Using the results of the simulations described in Chapter 2 and the magnetic phase diagram (Figure 2.10), we can estimate the critical dFP concentration  $p_c$  corresponding to the fluence  $f_c$ . For Sample TiO<sub>2</sub>200, we find a critical concentration  $p_c = 8 \text{ at.}\%$  and for Sample TiO<sub>2</sub>1000,  $p_c = 5 \text{ at.}\%$ . These values correspond to those calculated using Monte Carlo simulations in Section 2.4.

As the remanent magnetization shows only contributions from the ferromagnetic percolation continent, its value should follow the same critical behavior as the order parameter  $P_\infty$  that describes the probability that a defect belongs to the percolation continent. Assuming that the dFP concentration  $p$  is proportional to the irradiation fluence  $f$ , we can fit the remanent magnetization to

$$M_{\text{rem}}(f) \propto (f - f_c)^\beta \quad (4.1)$$

and obtain a good estimate of the critical exponent  $\beta$ . The fits are shown in Figure 4.1 (b) as dashed lines. The experimental critical exponents  $\beta$  are shown in Table 4.1. For sample TiO<sub>2</sub>1000, we obtain a value of the critical exponent that matches well the theoretical value for a 3D system. For sample TiO<sub>2</sub>200, the value is in between those predicted for a 2D and 3D system, indicating that the resulting percolation process takes place in a quasi-2D region of the sample. This result is in accordance with the predicted thickness of one unit cell of the emerging FM phase. The saturation magnetization also follows a power law

$$M_{\text{sat}}(f) \propto f^\alpha \quad (4.2)$$

as shown by dashed lines in Figure 4.1 (a). The exponents  $\alpha$  obtained by fitting the experimental data are shown in Table 4.1.

For comparison, we calculated the critical exponent  $\alpha$  from the experimental magnetization data of CeO<sub>2</sub> hosts irradiated with Xe ions at  $E_{\text{ion}} =$

Sample	TiO <sub>2</sub> 200	TiO <sub>2</sub> 1000	CeO <sub>2</sub>
$f_c$ ( $10^{16}$ cm <sup>-2</sup> )	0.49	1.8	–
$p_c$ (at %)	8	5	–
$\alpha$	$0.10 \pm 0.05$	$0.29 \pm 0.05$	$0.6 \pm 0.2$
$\beta$	$0.31 \pm 0.03$	$0.41 \pm 0.05$	–

TABLE 4.1: Experimental percolation parameters ( $f_c$ : Critical fluence;  $p_c$ : Critical dFP concentration;  $\alpha, \beta$ : Critical exponents), obtained experimentally from magnetization data of TiO<sub>2</sub> samples irradiated with Ar<sup>+</sup> ions at  $E_{\text{ion}} = 200$  eV (TiO<sub>2</sub>200) and 1 keV (TiO<sub>2</sub>1000) and of CeO<sub>2</sub> samples irradiated with 200 MeV Xe ions [28].

200 MeV, published by Shimizu et al. [28] (see Figure 4.2). In the fitting procedure to the power law, we only considered those magnetization values obtained at fluences up to  $2 \times 10^{13}$  cm<sup>-2</sup>, where the effects of the amorphization are not too strong. We find a value  $\alpha = 0.6 \pm 0.2$ , which indicates a 3D percolation process. The other percolation parameters could not be recovered from the published experimental data.

Two dimensional long ranged magnetic order has long been thought to be impossible at finite temperatures, as stated by the Mermin-Wagner (MW) theorem [60]: In bulk 3D ferromagnets, the exchange interaction asserts a long range magnetic order up to the Curie temperature,  $T_C$ , where thermal fluctuations become strong enough to randomize the spin orientation. In 2D magnetic systems with isotropic exchange interaction, the dimensionality effect leads to an abrupt jump in the magnon dispersion and therefore strong spin excitations at any finite temperature, destroying magnetic order. The presence of a strong uniaxial local magnetic anisotropy opens a gap in the magnon dispersion, counteracting the Mermin-Wagner theorem in 2D and restoring long range order. This has been demonstrated experimentally in ultrathin transition metal films [61, 62] and 2D magnetic van der Waals materials [9, 63, 64]. 2D magnetic structures are not only interesting from a fundamental physics perspective, but also regarding their possible applications in 2D spintronics, magnonics or spin-orbitronics [1–3, 9, 64]. Due to the requirements of large exchange and anisotropy, intrinsic 2D magnetism is rather uncommon and largely restricted to low temperatures.

Ultrathin magnetic films of thicknesses reaching the monolayer limit have been of great interest, owing to their exotic magnetic properties. For instance, the critical behavior at the paramagnetic-ferromagnetic phase transition of an ultrathin ferromagnetic film shows a dimensional crossover upon reaching the two dimensional limit [61, 62, 65, 66]. In some materials, the magnetization strongly depends on the film thickness and can be enhanced [61, 62, 67] or reduced [68] at a critical thickness of the order of a few monolayers. At surfaces and interfaces, the crystal symmetry is broken in the direction normal to the film plane. This can lead to strong spin-orbit coupling and enhanced magnetic anisotropy. Also the contribution of the orbital magnetic moment can become important at the monolayer limit.

The computational results for the artificial ferromagnetic phase emerging in defective anatase TiO<sub>2</sub> hosts (Section 2.5) and the experimental realization of these artificial ferromagnets (Section 3.3) suggest that the emerging ferromagnetic phase resulting from the introduction of defects in the

host film by low energy ion irradiation, is confined to a thin layer near the film surface with a thickness of a few unit cells. In this chapter, the effects of the layer thickness and the influence of the surface on the magnetic properties are discussed. Specifically, the magnetic anisotropy of the different magnetic films are investigated. First, the origin of the magnetic anisotropy in thin films is introduced, followed by a discussion of the magnetic anisotropy measured in the  $\text{TiO}_2$  samples introduced in the previous chapter. The results are compared to DFT electronic structure calculations at the defective  $\text{TiO}_2$  surface.



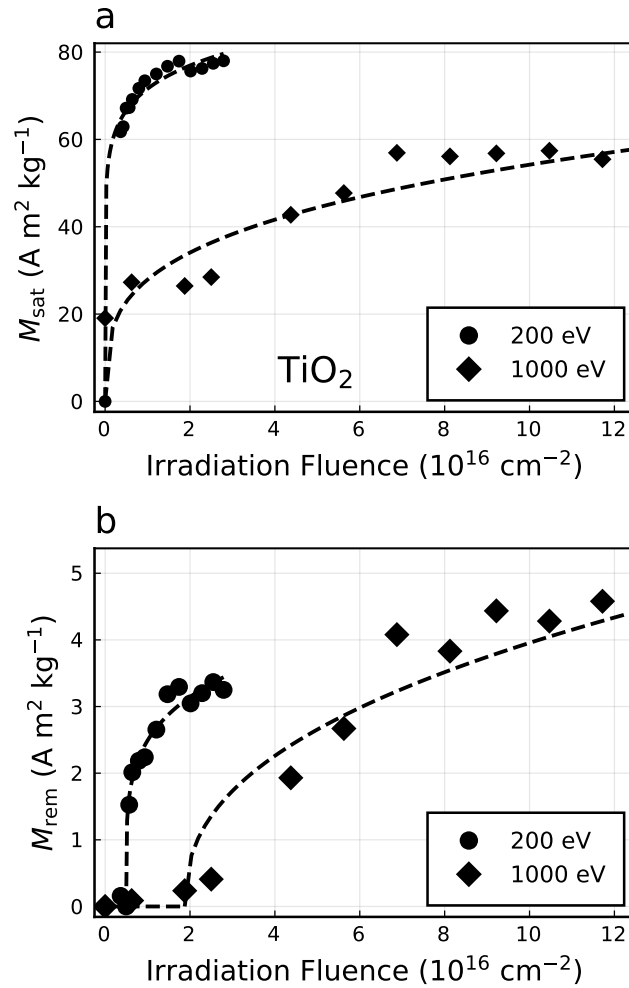


FIGURE 4.1: **Critical behavior at the percolation threshold.** Magnetization of artificial ferromagnets created in anatase TiO<sub>2</sub> thin films by Ar<sup>+</sup> ion irradiation at ion energies  $E_{\text{ion}} = 200$  eV and  $E_{\text{ion}} = 1000$  eV, measured at  $T=300$  K, as a function of the irradiation fluence. (a) Magnetization at saturation, measured at an applied magnetic field  $B = 5$  T. A constant diamagnetic contribution was subtracted. (b) Remanent magnetization at zero applied magnetic field, after the sample had been exposed to a field  $B = 5$  T. The dashed lines show the best fits to a power law (Equations (4.2) and (4.1)).

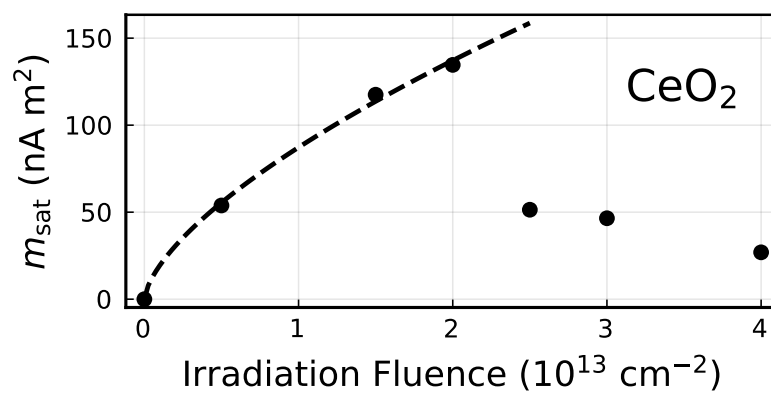


FIGURE 4.2: **Critical behavior.** Total magnetic moment at saturation of the FM phase emerging in a  $\text{CeO}_2$  bulk samples irradiated with  $\text{Xe}^+$  ions at  $E_{\text{ion}} = 200 \text{ MeV}$  (data reproduced from [28]). The dashed line shows the best fit to Equation (4.2), taking into account the measurements at fluences  $f \leq 2 \times 10^{13} \text{ cm}^{-2}$ , yielding the critical exponent  $\alpha$  shown in Table 4.1.

## 4.2 Magnetic anisotropy

The magnetization in ferromagnetic materials is usually anisotropic, i.e. the material can be magnetized with minimum energy in certain crystal directions, called the easy axes, while in other directions, the hard axes, a maximum of energy is necessary. The energy needed to change the magnetization of a ferromagnetic material from the easy to the hard axis is called Magnetic Anisotropy Energy (MAE).

The contributions to magnetic anisotropy mainly fall into three categories, namely the shape anisotropy due to the sample geometry. This contribution is usually dominating in slabs or thin films and leads to a magnetic easy axis lying within the plane of the film. The second contribution, the so-called Magnetocrystalline Anisotropy (MCA) mainly stems from the coupling between the orbital electron motion to the crystal field and results in preferential magnetization directions due to spin-orbit interaction. The third contribution is related to mechanical forces and stresses acting on the material, leading to anisotropy via magnetoelastic effects.

In the following section, the contributions to the magnetic anisotropy, which are most relevant to the artificial ferromagnetic TiO<sub>2</sub> samples, are described in more detail.

### 4.2.1 Demagnetizing field and magnetic shape anisotropy

The magnetic shape anisotropy can be thought of as resulting from the dipolar interaction between microscopic magnetic moments. This interaction is long-ranged and senses the surface of the sample. Therefore, the magnetic shape anisotropy can be described in a classical continuum theory.

Starting from the definition of the magnetic field inside a magnetic body

$$\vec{B} = \mu_0 (\vec{M} + \vec{H}), \quad (4.3)$$

its divergence is equal to

$$\nabla \cdot \vec{H} = \frac{1}{\mu_0} \nabla \cdot \vec{B} - \nabla \cdot \vec{M} = -\nabla \cdot \vec{M}. \quad (4.4)$$

Outside the body, in vacuum, one obtains

$$\nabla \cdot \vec{H} = \frac{1}{\mu_0} \nabla \cdot \vec{B} = 0. \quad (4.5)$$

In the absence of free currents, where  $\nabla \times \vec{H} = 0$ , a magnetic scalar potential

$$\vec{H} = -\nabla \phi \quad (4.6)$$

can be introduced and the above equations can be rewritten as

$$\nabla^2 \phi_{\text{in}} = \nabla \cdot \vec{M} \quad (4.7)$$

and

$$\nabla^2 \phi_{\text{out}} = 0. \quad (4.8)$$

These equations have the form of a Poisson equation, where the divergence of the magnetization acts as a source of magnetic field inside the sample. Continuity requirements of the fields at the surface of the magnetic body imply:

$$\phi_{\text{in}} = \phi_{\text{out}} \quad (4.9)$$

and

$$\frac{\partial \phi_{\text{in}}}{\partial n} = \frac{\partial \phi_{\text{out}}}{\partial n} + \vec{M} \cdot \vec{n}, \quad (4.10)$$

where  $\vec{n}$  is the surface normal and  $\partial n$  signifies the derivative with respect to the surface normal direction. The solution to the Poisson equation determines the so-called demagnetizing field  $H_d$  inside the magnetic body.

For arbitrary sample geometries, the demagnetizing field can have a very complex form and has to be determined numerically using micromagnetic simulation techniques. For simple and regularly shaped geometries, analytical approximations for the demagnetizing field exist. Notably, for uniformly magnetized ellipsoids, the demagnetizing field can be expressed as

$$H_k = (H_0)_k - \frac{\gamma_k}{4\pi} (M_0)_k \quad k = x, y, z \quad (4.11)$$

where  $H_0$  is a uniform external magnetic field,  $M_0$  is the uniform magnetization and  $\gamma_k$  are called the demagnetizing factors, that depend on the specific sample geometry. In the case of a sphere, all three factors are equal and  $\gamma_k = 4\pi/3$ . In the case of an infinite plane, i.e. an infinitely flat ellipsoid, the factor  $\gamma_n = 4\pi$  in the direction normal to the plane and zero otherwise.

For a thin magnetic film, this means that an external magnetic field applied in the direction normal to the sample is effectively lowered by the magnetization inside the film, while a field applied in the plane of the film is not affected. This gives rise to a magnetic shape anisotropy, favoring a magnetization lying in the plane of the thin film.

The energy of the demagnetizing field is given by

$$E_d = \mu_0 \int_{\text{magnet}} \vec{M} \cdot \vec{H}_d dV. \quad (4.12)$$

This allows to calculate the MAE due to the shape anisotropy. The shape anisotropy constant is equal to the energy difference between the magnetic field applied in plane and out of the film plane and can be expressed as

$$K_{\text{shape}} = -(E_{\perp} - E_{\parallel}) = \mu_0 \int_{\text{magnet}} \vec{M}^2 dV = \mu_0 \vec{M}^2 V = \mu_0 \frac{\vec{m}^2}{V}, \quad (4.13)$$

assuming uniform magnetization. The magnetic anisotropy energy due to the shape anisotropy of a thin magnetic film follows the dependence

$$\text{MAE}(\theta) = \mu_0 \frac{m_{\text{sat}}^2}{V} \cos^2(\theta) = K_{\text{shape}} \cos^2(\theta), \quad (4.14)$$

where  $\theta$  is the angle between the magnetization and the film normal. In magnetic films, the magnetic shape anisotropy constant  $K_{\text{shape}}$  is negative, favoring an in-plane easy axis.

In thin magnetic films, it is more common to express the MAE as a sheet energy density in units of  $\text{J m}^{-2}$ . With a film area of  $0.5 \times 0.5 \text{ cm}^2$  and

a magnetic moment at saturation  $m_{\text{sat}} \approx 5 \text{ nAm}^2$ , one obtains  $K_{\text{shape}} \approx 0.05 \text{ mJ m}^{-2} = 45 \text{ } \mu\text{eV/atom}$ .

### 4.2.2 Magnetocrystalline anisotropy

In general, the MCA has a complex dependence on the magnetization direction with respect to the crystallographic axes and is often represented as an expansion in powers of the magnetization direction cosines. In many crystals, there is a single axis of high symmetry (taken along the z-direction) and the MCA is uniaxial. To lowest order, the MAE takes the form

$$\text{MAE}(\theta) = K_u \cos^2(\theta), \quad (4.15)$$

where  $\theta$  is the angle between the magnetization direction and the high symmetry axis (z) and  $K_u$  is the uniaxial MCA constant. If  $K_u > 0$ , the easy direction is along the z-direction. Otherwise, there is an easy plane perpendicular to the z-axis and the lowest order MAE term does not fix the direction within this plane. In that case, higher order terms are needed to determine the easy-axis.

Microscopically, the magnetocrystalline anisotropy is due to the Spin-Orbit Interaction (SOI), which couples the electrons spin to their orbital angular momentum. In a crystal, the electrostatic potential of the atoms and the other electrons lift the orbital degeneracy, the so-called crystal field splitting. This leads to certain directions of the magnetization, the magnetic easy axes, having lower total energy than the hard axes. The number and directions of such axes depend on the symmetry of the crystal.

The MCA energy can be calculated from first principles using the DFT techniques introduced in Section 2.3. In order to take into account the effects of spin-orbit coupling, the Kohn-Sham equations have to be modified. The SOI results from the relativistic treatment of the electron in the context of the Dirac theory. In general, the KS-problem of DFT, Equation (2.19), can be modified to solve the Dirac instead of the Schrödinger equation in the so-called fully relativistic formulation of DFT [69]. For most applications, the so-called scalar relativistic approximation can be used and the SOI corrections can be incorporated, as described in Reference [69]. This approach is implemented in the FLEUR code and is used in this work.

To illustrate the effect of SOI on the magnetic anisotropy, we calculated the total energy of the bulk anatase supercell containing one dFP defect, as described in Section 2.5.2, taking SOI into account and varying the magnetization direction. The MAE due to the MCA is then calculated as the total energy difference of the magnetization directions. Calculating the total energy difference between the systems where the magnetization direction is fixed in the out of plane (001) crystal direction ( $E_{\perp}$ ) and in the in-plane (100) direction ( $E_{\parallel}$ ), the uniaxial MAE constant  $K_u = E_{\perp} - E_{\parallel}$  can be obtained. For the bulk 3D anatase system containing 5.5% dFP defects, we find  $K_u^{\text{bulk}} = 11 \text{ } \mu\text{eV/atom}$ .

### 4.3 Artificial ferromagnetic monolayer at TiO<sub>2</sub> surface with perpendicular magnetic anisotropy

All experimental results discussed in the previous chapter were obtained with a magnetic field applied within the anatase TiO<sub>2</sub> film plane. In order to determine the easy axis direction experimentally, measurements of the magnetization as a function of a magnetic field applied along the surface normal, i.e. along the (001) crystal axis, were also performed. Examples of the resulting magnetization loops are shown in Figure 4.3. In each panel, the in-plane magnetization is shown in blue and the out-of-plane magnetization is shown in orange. The panels (a,c,e) show the raw magnetization loops and (b,d,f) show the FM signals obtained after subtracting the linear dia- and paramagnetic background signals.

Figures 4.3(a,b) show the magnetization loops measured after irradiation of  $2.5 \times 10^{16} \text{ cm}^{-2}$  ions at  $E_{\text{ion}} = 200 \text{ eV}$ . The magnetization shows a preferential direction pointing out of the film surface, which is unexpected, as both the shape and MCA contributions to the magnetic anisotropy determined in the previous section suggest an in-plane easy axis. This is especially true in a magnetic monolayer, where the aspect ratio of the sample is maximal and the approximation of the shape anisotropy of an infinite plane becomes sensible. In order to give rise to a net out-of-plane magnetic easy axis, a strong additional contribution to the anisotropy energy must be present. As we will show, this contribution comes from the MCA at the sample surface.

The sample irradiated with  $6.0 \times 10^{16} \text{ cm}^{-2}$  ions at  $E_{\text{ion}} = 500 \text{ eV}$  shows the expected anisotropy behavior: the preferential direction of the magnetization lies within the plane of the film surface, as shown in Figure 4.3(c,d).

In the sample irradiated with  $1.2 \times 10^{17} \text{ cm}^{-2}$  ions at  $E_{\text{ion}} = 1000 \text{ eV}$ , the magnetization loops show an easy axis pointing out of the film plane, although the difference between the curves is less striking (see Figure 4.3(e,f)). All three examples were chosen at the total irradiation fluence at which the respective sample shows a maximum magnetization.

Figure 4.4 show the total MAE calculated from area differences of ferromagnetic hysteresis curves, such as those shown in Figure 4.3, as a function of the irradiation fluence, for the sample irradiated at (a)  $E_{\text{ion}} = 200 \text{ eV}$  and (b)  $E_{\text{ion}} = 500 \text{ eV}$ . At  $E_{\text{ion}} = 200 \text{ eV}$ , the MAE is negative throughout all irradiation fluences, indicating a magnetic easy axis normal to the film surface. The magnitude of the MAE first increases, reaching a maximum of  $0.018 \text{ mJ m}^{-2}$  around a fluence of  $10^{16} \text{ cm}^{-2}$  and then decreases to  $0.008 \text{ mJ m}^{-2}$ . At  $E_{\text{ion}} = 500 \text{ eV}$ , the MAE first increases to a positive value of  $0.035 \text{ mJ m}^{-2}$  at a fluence of  $2.5 \times 10^{16} \text{ cm}^{-2}$ , indicating a magnetic easy plane parallel to the film surface. Increasing the irradiation fluence further, the MAE decreases and changes sign, reaching a minimum of  $-0.028 \text{ mJ m}^{-2}$  at a fluence of  $7.5 \times 10^{16} \text{ cm}^{-2}$ , indicating a change from the easy plane to an out-of-plane easy axis. Increasing the fluence even further, the anisotropy flips again. The MAE seems to follow an oscillating behavior, flipping between in-plane and out-of-plane magnetic anisotropy.

It appears therefore plausible that the magnetic easy direction strongly depends on the depth of the magnetic layer below the surface. In fact, we have seen that at higher irradiation energies, where the easy axis lies

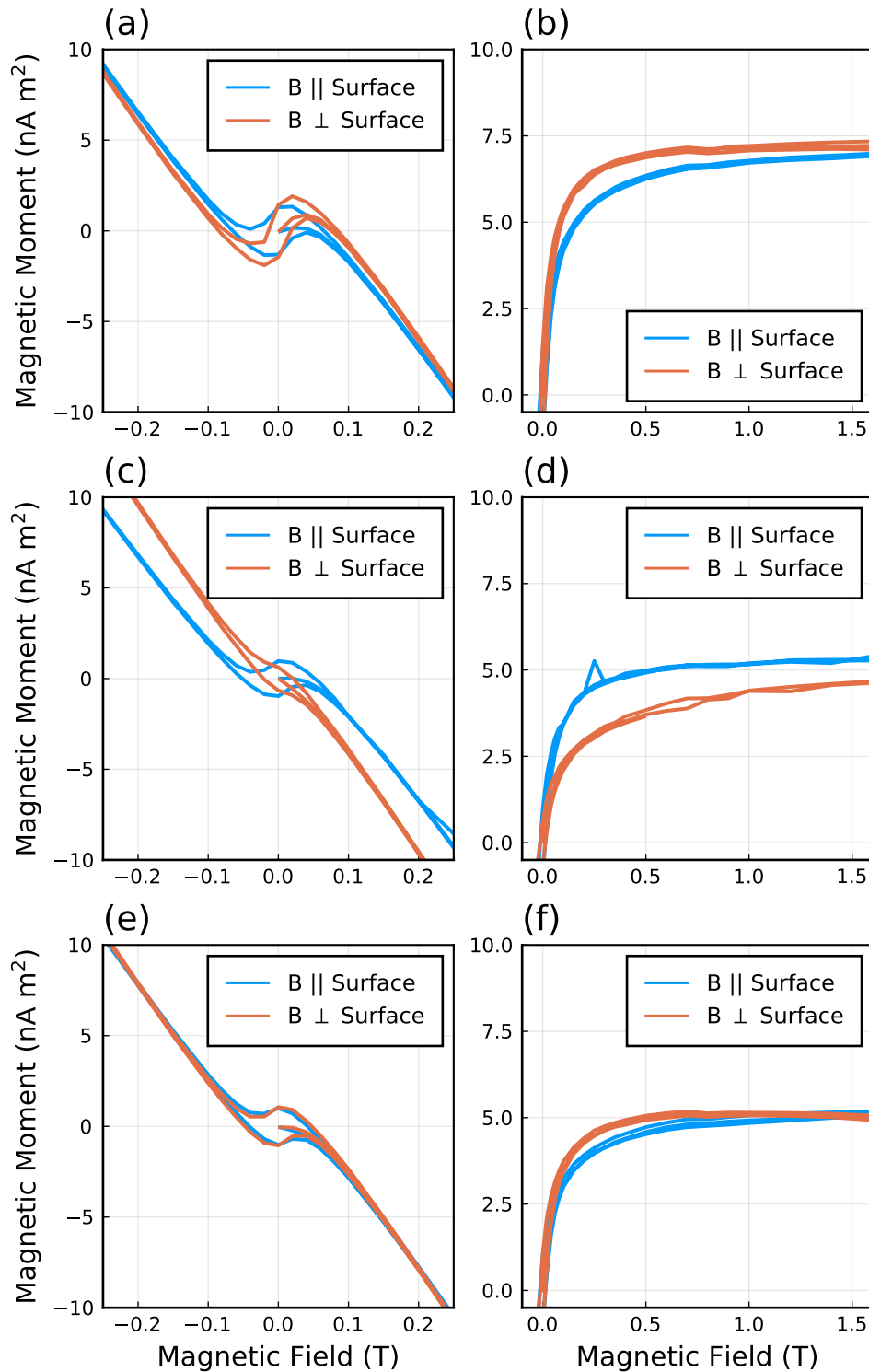


FIGURE 4.3: **Magnetic anisotropy** Magnetic hysteresis loops measured with the external magnetic field applied in the plane of the TiO<sub>2</sub> films (blue) and out-of-plane (orange). The left panels show the total magnetic moment measured by SQUID magnetometry, the right panels show the ferromagnetic signal after subtracting the background diamagnetic and paramagnetic signals. Panels (a),(b) show the results obtained for the sample after irradiation with Ar<sup>+</sup> ions with a fluence of  $2.5 \times 10^{16} \text{ cm}^{-2}$  at  $E_{\text{ion}} = 200 \text{ eV}$ , panels (c),(d) with a fluence of  $6.0 \times 10^{16} \text{ cm}^{-2}$  at  $E_{\text{ion}} = 500 \text{ eV}$  and (e),(f) with a fluence of  $1.2 \times 10^{17} \text{ cm}^{-2}$  at  $E_{\text{ion}} = 1000 \text{ eV}$ .

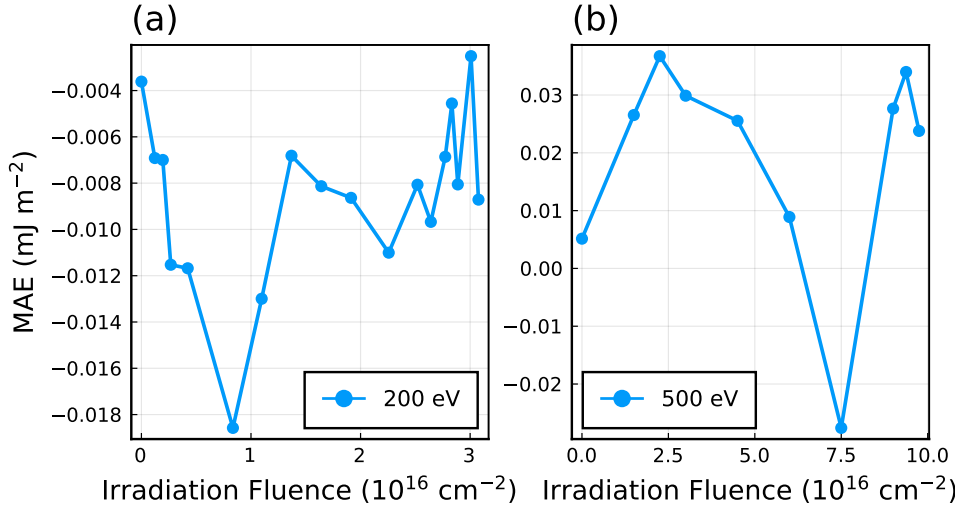


FIGURE 4.4: **Magnetic anisotropy energy.** The MAE determined from the area difference between the hysteresis curves measured at a field applied in-plane and out-of-plane. Positive values indicate an easy axis lying within the surface plane, negative values indicate an easy axis perpendicular to the surface. (a) MAE of the sample irradiated at  $E_{\text{ion}} = 200 \text{ eV}$  as a function of total irradiation fluence. (b) MAE of the sample irradiated at  $E_{\text{ion}} = 500 \text{ eV}$ .

within the film plane, the FM phase emerges not only at the surface but also in a buried layer in the bulk of the sample, whereas at 200 eV it emerges right at the surface (Figure 2.10) with a perpendicular magnetic anisotropy (PMA). This behavior is well known in metallic multilayers, where a PMA is present in multilayer films grown on different substrates and switches at a film thickness of several tens of Å [70].

This suggests that the perpendicular contributions to the MAE must come from magnetic surface states, which dominate in the sample irradiated at  $E_{\text{ion}} = 200 \text{ eV}$ . The proportion of magnetic bulk and surface states created during the ion irradiation then determines the total measured MAE.

In the next section, we will investigate the magnetic properties of the dFP defect at the anatase  $\text{TiO}_2$  [001] surface using the FLAPW method and compare the results to those obtained in the bulk (Section 2.5.2).



## 4.4 DFT calculations of the defective anatase TiO<sub>2</sub> [001] surface

To understand the oscillations of the MAE in the sample irradiated at 500 eV and its dependence on the irradiation energy, we performed DFT electronic structure calculations of the defective TiO<sub>2</sub> surface using the FLAPW method implemented in the FLEUR code. In most solid-state DFT codes that use plane wave basis sets, the calculation of surfaces or interfaces requires some tricks to incorporate the broken translational symmetry. One common strategy is to create a supercell containing a so-called vacuum region, i.e. the size of the supercell is extended in the direction normal to the surface, in order to separate the periodic copies of the atomic structure from each other. Ideally, this vacuum region should be large enough to prevent any interaction between the copies. In practice, such a large vacuum region significantly impacts the computational cost and a tradeoff between speed and accuracy has to be found. In the FLAPW method, space is partitioned into muffin-tin and interstitial regions, as described in Section 2.5.2, and the KS wavefunctions are matched at the region boundaries. This trick can be used to model surfaces in an efficient way [71]. The basis functions are extended into the exterior boundary regions of the surfaces, the vacuum regions, along the z-direction. There, they take the form of linear combinations

$$\phi_{kG}^{\text{vac}}(r) = [a_{kG}^{\text{vac}} u_{kG}^{\text{vac}}(z, E^{\text{vac}}) + b_{kG}^{\text{vac}} \dot{u}_{kG}^{\text{vac}}(z, E^{\text{vac}})] \times \frac{1}{\sqrt{A}} e^{i(k+G)r}, \quad (4.16)$$

of the solutions  $u_{kG}^{\text{vac}}$  and their energy derivatives  $\dot{u}_{kG}^{\text{vac}}$  of the Schrödinger equation in the vacuum region:

$$\left[ -\frac{1}{2} \frac{\partial^2}{\partial z^2} + \frac{1}{2} (k+G)^2 + V_{\text{eff}}^{\text{vac}}(z) - E^{\text{vac}} \right] u_{kG}^{\text{vac}}(z, E^{\text{vac}}) = 0 \quad (4.17)$$

at the energy  $E^{\text{vac}}$  in the effective vacuum potential  $V_{\text{eff}}^{\text{vac}}$ . This method allows to model two semi-infinite vacuum regions in the exterior of the surfaces of a slab and avoids the spurious interaction between the periodic copies, that one has to deal with in traditional supercell methods.

Following the construction of the defective TiO<sub>2</sub> system in the bulk (Section 2.5.2), we created a supercell with  $3 \times 3$  lateral unit cells of the anatase TiO<sub>2</sub> host and four layers in the (001) direction (see Figure 4.5(b)). One dFP defect was introduced in the supercell in such a way that one Ti interstitial was placed in an inner layer (Ti<sub>i</sub>1) and the other at the lower surface layer (Ti<sub>i</sub>2). In a first step, the atomic positions of the lower two layers ((1) and (2) in Figure 4.5) were relaxed, while keeping the upper two layers ((3) and (4) in Figure 4.5) fixed at their bulk positions. After structural relaxation, the surface layer (1) shows displacements comparable to values found in the literature [72] ( $\alpha = 142^\circ$ , Ti<sub>5c</sub>-O<sub>2c</sub> (short) = 1.813 Å, Ti<sub>5c</sub>-O<sub>2c</sub> (long) = 2.010 Å, Ti<sub>5c</sub>-O<sub>3c</sub> = 1.941 Å).

Then, the self consistent charge and spin densities were calculated following the method described in Section 2.5.2. Figure 4.5 shows the relaxed bulk (panel (a)) and surface (panel (b)) structures. The atomic positions are represented as spheres (blue: Ti; red: O; pink: Ti<sub>i</sub>). Isosurfaces at a spin density of  $0.005 \mu_B a_0^{-3}$  are shown in yellow. Comparing the spin densities

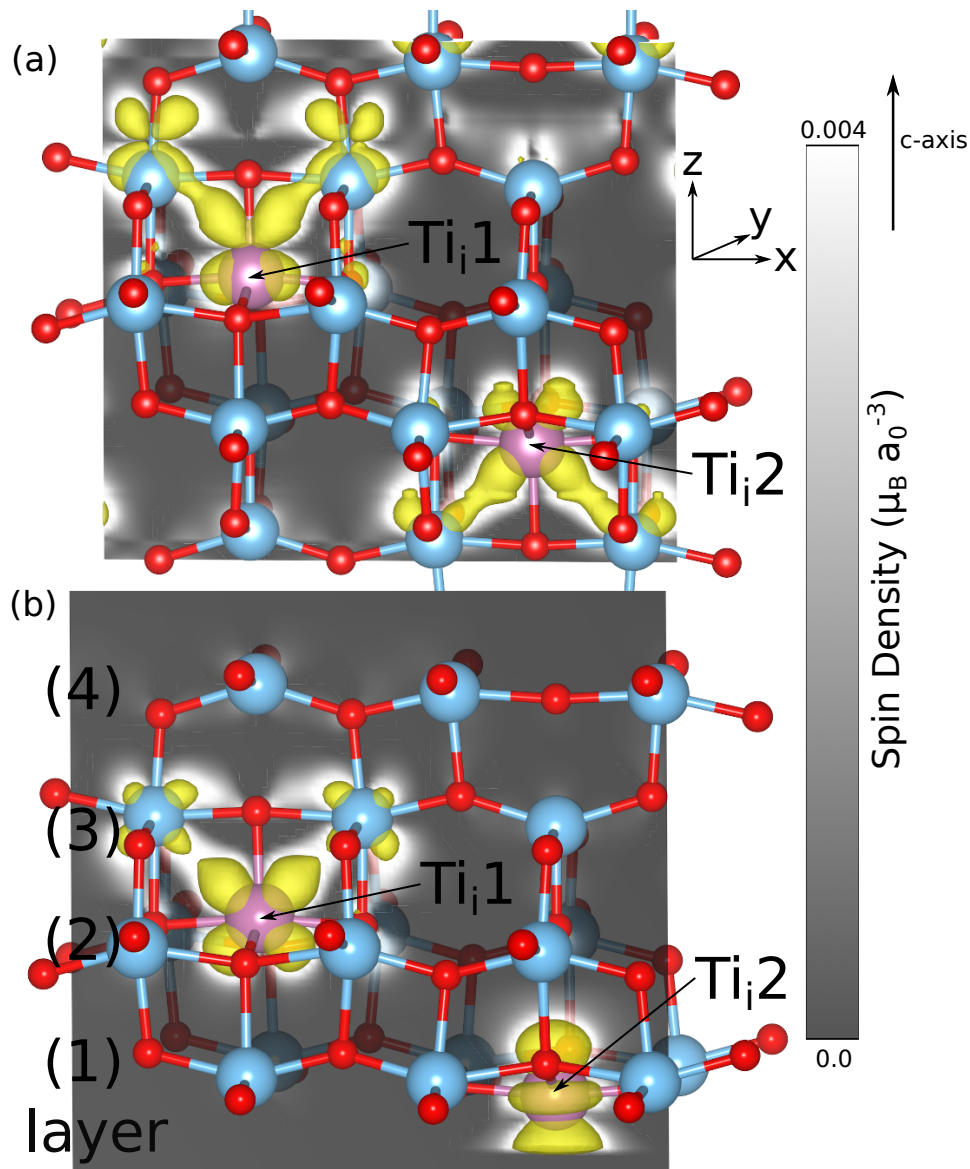


FIGURE 4.5: **Surface spin density** obtained from FLAPW-DFT calculations for (a) a 3x3x1 bulk anatase supercell and (b) a 3x3x1 supercell consisting of four atomic layers (labeled (1)-(4)) below the [001] anatase surface, each containing one dFP defect per supercell. The relaxed atom positions are represented by spheres (blue: Ti, red: O, purple: Ti<sub>i</sub>). The two Ti interstitials are indicated by arrows and labeled Ti<sub>i</sub>1 and Ti<sub>i</sub>2. The isosurface at 0.005 μ<sub>B</sub>a<sub>0</sub><sup>-3</sup> spin density is shown in yellow. The spin density in the [010]-plane through the two interstitials is indicated by shades of gray according to the scale on the right.

in the two structures, one first observes a striking difference at the Ti interstitial in the surface layer ( $\text{Ti}_i2$ ). While in the bulk structure, the symmetry of the spin density around the two interstitials is very similar and has a  $d_{xy}$  orbital character, at the surface ( $\text{Ti}_i2$  in panel (b)), the spin density has a  $d_{z^2}$  character. The Ti interstitial on the inner layer ( $\text{Ti}_i1$  in panel (b)), on the other hand, has a similar structure as in the bulk ( $\text{Ti}_i1$  in panel (a)).

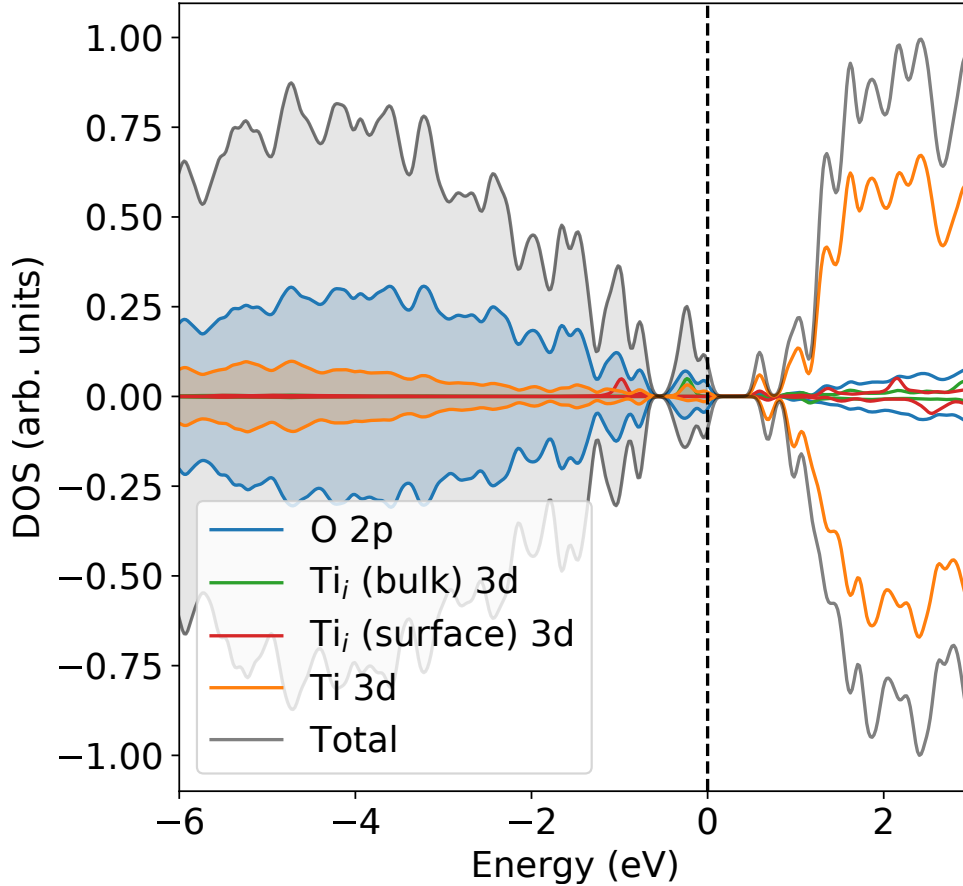


FIGURE 4.6: **Density of states (DOS)** of the anatase  $\text{TiO}_2$  [001]-surface containing 5.5 % dFP defects. The total DOS is shown in gray; the partial DOS (PDOS) projected onto the O 2p states is shown in blue; the PDOS of lattice Ti 3d states in orange; the PDOS of the bulk ( $\text{Ti}_i1$ ) and surface ( $\text{Ti}_i2$ ) interstitials are shown in green and red, respectively.

This difference is reflected in the DOS of the surface system, shown in Figure 4.6. The 3d states of both Ti interstitials are spin polarized, as it was the case in the bulk system (see Figure 2.9). The PDOS of the  $\text{Ti}_i1$  (green line in Figure 4.6), shows a peak at the same position as in the bulk system. The PDOS of the interstitial  $\text{Ti}_i2$  in the surface layer (red line in Figure 4.6) also shows a peak, but its position is shifted towards lower energies.

As we have seen in Section 4.2, the orbital structure of the spin-polarized states is closely related to the magnetocrystalline anisotropy through the spin-orbit interaction. We should therefore expect an effect on the MCA due to the drastic change of orbital symmetry at the surface layer. We calculated the MCA energy of the defective  $\text{TiO}_2$  surface from total energy differences, taking into account SOI as described in Section 4.2, and find the value of

the uniaxial MCA constant  $K_u^{\text{surface}} = -137 \mu\text{eV}/\text{atom}$ . The minus sign indicates an easy axis in the direction normal to the surface.

	MAE ( $\mu\text{eV}/\text{atom}$ )
Shape anisotropy ( $K_{\text{shape}}$ )	+45
Bulk MCA ( $K_u^{\text{bulk}}$ )	+11
Surface MCA ( $K_u^{\text{surface}}$ )	-137

TABLE 4.2: Calculated contributions to the MAE in the anatase  $\text{TiO}_2$  artificial ferromagnet.

Taking into account the geometrical distribution of the emerging ferromagnetic phase within the  $\text{TiO}_2$  host (Figure 2.10), its proximity to the surface and the dependence on the ion energy and fluence, as well as the different contributions to the MAE summarized in Table 4.2, the behavior of the experimentally observed total MAE (Figure 4.4) can be understood. At  $E_{\text{ion}} = 200 \text{ eV}$ , the FM phase first emerges at the surface, which contributes with a negative MCA energy to the total MAE. When the ion fluence is increased, the defects created in lower lying layers reach the percolation threshold and start to contribute to the FM signal with a positive contribution to the MAE. As a result, the total measured MAE decreases in magnitude due to the competing contributions. At higher ion energies, the FM phase emerging in the surface layer still contributes to the total magnetic signal, but the bulk contribution is more important. Due to the amorphization and sputtering processes taking place during the ion irradiation, the strength of each contribution varies in a complicated non-linear way as a function of the ion fluence and hence, we observe fluctuations and even switching between inplane and out of plane anisotropy (Figure 4.4(b)).

The strong perpendicular magnetic anisotropy of the surface allows to stabilize the artificial FM phase down to the 2D limit of the host monolayer. By tuning the irradiation parameters, the thickness and depth of the emerging ordered phase can be controlled and the total MAE can be tailored, favoring an in-plane or out of plane easy axis. The experimental results of this chapter demonstrate the versatility of artificial ferromagnets. Using ion irradiation techniques to introduce certain defects, one can not only induce a strong and robust ferromagnetically ordered phase in a non-magnetic host material, but systematically control its magnetostatic properties and, to some extent, its geometry and location within the host crystal. This amount of fine control makes artificial ferromagnetism due to defects a powerful materials engineering tool. A further advantage of these materials lies in the ability to combine the emerging magnetic properties with the intrinsic properties of the host material. In the next chapter, we combine the electronic properties of the semiconducting oxide ZnO with the spin structure of an emerging ferromagnetic phase induced by ion irradiation to control the spin transport through the material and construct a spin filter device.

## Chapter 5

# Spin transport through artificial ferromagnet interfaces

Although the magnetostatic properties of artificial ferromagnetic materials, such as those discussed in the previous chapters, are interesting on their own and can be engineered to exhibit tunable properties convenient for applications, one of the most exciting prospects of this kind of materials is the ability to induce a ferromagnetic phase while keeping some of the intrinsic properties of the host material. Shortly after artificial ferromagnetism induced by defects, that persists up to room temperature, was first predicted in semiconducting materials [10], possible applications of these materials for spintronic devices [36] attracted many researchers to the field. Especially the ability to generate and control spin currents is of great interest in these materials and for applications. ZnO was one of the first host materials proposed as a room temperature artificial ferromagnetic semiconductor and its magnetic properties are today well understood.

In this last chapter, we provide a short review of the emerging ferromagnetism due to defects in ZnO and investigate the spin dynamics in this artificial ferromagnetic semiconductor experimentally. Exploiting the semiconducting nature of the host and the ability to tune its electronic structure by doping, we show the realization of a spin filter device at magnetic/non-magnetic interfaces in ZnO, allowing to generate highly spin polarized currents.

## 5.1 Artificial ferromagnetism in ZnO hosts

The first reports of magnetic ZnO were based on a prediction of Dietl et al. [10] twenty years ago that a ferromagnetic phase with a Curie temperature above 300 K would emerge in ZnO when doped with magnetic transition metal ions, such as Fe, Co or Mn. Although many different groups started measuring the magnetic properties of these so-called dilute magnetic semiconductors (DMS) [37, 73–85], doubts were soon raised on the origin of the measured signals [86–88], due to inconsistencies in the reported measurements and the realization that samples doped with non-magnetic elements, such as lithium [89, 90], nitrogen [91–93], copper [20, 94], boron [24], potassium [95], aluminum [96] or carbon [18, 97], and even undoped [12, 98] thin film samples showed traces of ferromagnetism under certain growth conditions. It turned out that it were not the magnetic dopants that were at the origin of the emerging ferromagnetic phase in ZnO, but rather lattice defects that carry magnetic moment and interact ferromagnetically upon reaching magnetic percolation. Specifically, the Zn vacancy defect was soon found to play a major role in these materials [12, 89, 99–101]. The search for artificial ferromagnetic ZnO at room temperature is tightly related to another controversial research field, namely the search for p-type ZnO. In the following section, the main results of this research shall be reviewed.

Ueda et al. [73] reported on ZnO films grown by pulsed laser deposition (PLD) techniques and co-doped with Al and 5 at.%–25 at.% of Co. The films showed ferromagnetic behavior up to room temperature and the measured Curie temperature and saturation magnetization varied with the Co concentration. The authors correlated these variations with the carrier concentration, as the ferromagnetism was enhanced in the sample with highest conduction electron density. After several groups measured Mn doped ZnO samples and found no signs of ferromagnetism [73, 75], Sharma et al. [80] reported on ferromagnetic behavior at room temperature of bulk and PLD grown thin film ZnO samples, doped with < 4 at.% of Mn. Theoretical predictions suggested that the transition temperature of artificial ferromagnets based on ZnO hosts strongly depended on the concentration of magnetic defects and holes [10] and co-doping strategies were tested [78]. This requirement turned out to be rather difficult, as acceptor dopants resulting in high hole concentrations in ZnO remained elusive.

Soon after the first reports on ZnO based DMS appeared, doubts were raised on the origin of the magnetic signals. Park et al. [86] measured ZnO samples doped with Co and correlated the ferromagnetic signals appearing at concentrations > 12 at.% to the formation of metallic Co clusters. Lawes et al. [87] and Rao et al. [88] measured bulk ZnO samples with Co and Mn content of 2–15 at.% and both groups reported that the samples showed Curie-Weiss rather than ferromagnetic behavior.

Due to these controversies and the difficulties to disseminate the intrinsic origin of the ferromagnetic signals, samples doped with non-magnetic ions, considered to induce p-type carriers in ZnO were measured. Buchholz et al. [20] studied the magnetic properties of Cu doped ZnO films grown under conditions favoring n-type and p-type conduction and found that the films exhibiting p-type conduction were also ferromagnetic at temperatures in excess of 390 K. Ye et al. [94] performed DFT calculations using the



FLAPW method and found that Cu doping indeed could favor ferromagnetic order up to  $T_c \sim 380$  K, but found no sign of hole carrier mediation of the ferromagnetic coupling. Pan et al. [97] measured ZnO thin film samples doped with carbon and grown by PLD technique and reported on an emerging ferromagnetic phase with  $T_c > 400$  K. The authors performed DFT calculations and found that C substituting O atoms carry a magnetic moment of  $2 \mu_B$  that couples ferromagnetically. Yu et al. [92] measured ferromagnetic signals in nitrogen doped ZnO films grown by PLD with magnetization up to  $10 \text{ emu cm}^{-3}$  at room temperature.

The success in creating artificial ferromagnets based on ZnO doped with all kinds of non-magnetic elements led to the conclusion that the dopants might not play such an essential role in creating the ferromagnetic phase. Hong et al. had already reported on artificial ferromagnetism in other undoped nominally non-magnetic oxides ( $\text{HfO}_2$  and  $\text{TiO}_2$ ) [98]) which they attributed to the presence of oxygen vacancies, when they reported similar results in undoped ZnO thin films grown by laser ablation technique [13] and found that the magnetization depends on the film thickness. A comparison of their results to those obtained in Fe and Mn doped samples suggested that the transition metal doping played no essential role in the emerging ferromagnetic phase. The authors rather attributed the magnetic signals measured in the undoped samples to defects located at the film surface on the Zn sublattice.

In order to explain the magnetic signals found in undoped ZnO samples, Wang et al. [99] performed detailed DFT calculations of the magnetic properties of Zn and O vacancies in ZnO film and nanowire structures. Results of the calculations for the O vacancy indicate that it alone can not create any magnetic structure. The ZnO systems with a Zn vacancy, on the other hand, are magnetic: A Zn vacancy placed at the surface of a ZnO film results in a total magnetic moment of  $1.5 \mu_B$ , while a Zn vacancy in the bulk carries a magnetic moment of  $1.1 \mu_B$ . The main contribution to the magnetic moment comes from the spin polarized 2p states of the three oxygen atoms that are nearest neighbors of the vacancy. The total energy of supercell structures containing a concentration of up to  $\sim 7\%$  Zn vacancies were calculated and the coupling between the magnetic moments localized around each vacancy was determined. The authors found a ferromagnetic state, that is robust against thermal fluctuations at temperatures well above 300 K. Although the calculated formation energies for the two kinds of vacancies were rather high, the results indicated that the formation energy of Zn vacancies were significantly lower at the surface and at the same time, resulted in a higher magnetic moment as in the bulk. Calculations performed in nanowire structures led to similar results.

The results of the calculations pushed the interest in the magnetic properties of the intrinsic point defects formed in pure ZnO nanostructures and triggered a number of theoretical and experimental investigations [12, 102–107]. Khalid et al. [12] showed that ZnO films grown by pulsed laser deposition technique showed ferromagnetic signals, depending on the growth conditions. They observed a dependence of the saturation magnetization of the ferromagnetic signal on the  $\text{N}_2$  partial pressure in the growth chamber. The dependence on the growth conditions were correlated to the creation of Zn vacancy type defects using positron annihilation spectroscopy, in accordance with theoretical predictions. Kim et al. [104] performed electronic



structure calculations of the Zn vacancy defect using the FLAPW method. Their results suggest the importance of lattice distortions for the ferromagnetic order induced by Zn vacancies. In addition, the authors present calculations of x-ray magnetic circular dichroism spectra. Kumar et al. [104] measured the magnetic properties of undoped ZnO nanorods and found ferromagnetic signals at room temperature. Kapilashrami et al. [105] systematically measured the thickness dependence of the ferromagnetic signal in pure ZnO films grown by magnetron sputtering technique and found a maximum of the total magnetization at saturation at a film thickness of 480 nm.

The role of the Zn vacancy in the emerging artificial ferromagnetic phase in undoped ZnO was then widely recognized and the research interest shifted towards finding ways to lower the defect formation energy, in order to enhance their stability and concentration. Yi et al. [89] showed that ZnO films doped with Li and grown in oxygen rich environment could stabilize the formation of Zn vacancies and significantly enhance the ferromagnetic properties of the samples. Under oxygen rich conditions, Li preferentially substitute Zn atoms and act as acceptors in ZnO. At a nominal Li concentration of 8 %, the authors measure a maximum hole concentration of  $5.4 \times 10^{18} \text{ cm}^{-3}$ , coinciding with a maximum saturation magnetization and  $T_c = 525 \text{ K}$ . Similar results were obtained by Ghosh et al. [90, 95] for other alkali-metal substitutions, while Li shows the strongest effect. Khalid et al. [26] showed that a ferromagnetic phase could be induced in non-magnetic ZnO single crystal samples by proton bombardment. The magnetization of the samples increased with irradiation fluence up to 5 emu/g. Mal et al. [108] showed similar results obtained by irradiation of ZnO films with swift heavy ions. Lorite et al. [32] showed that ZnO microwires doped with Li acceptors and irradiated with protons show ferromagnetic signals increasing with the Li content and the proton fluence. They further show measurements of XMCD performed on the irradiated samples with different content of Li dopants. In the sample showing a clear ferromagnetic hysteresis, a XMCD signal appears at the oxygen K-edge of the absorption spectrum, that the authors attribute to the spin polarized 2p states of the oxygen atoms surrounding Zn vacancies, in accordance with theoretical predictions.

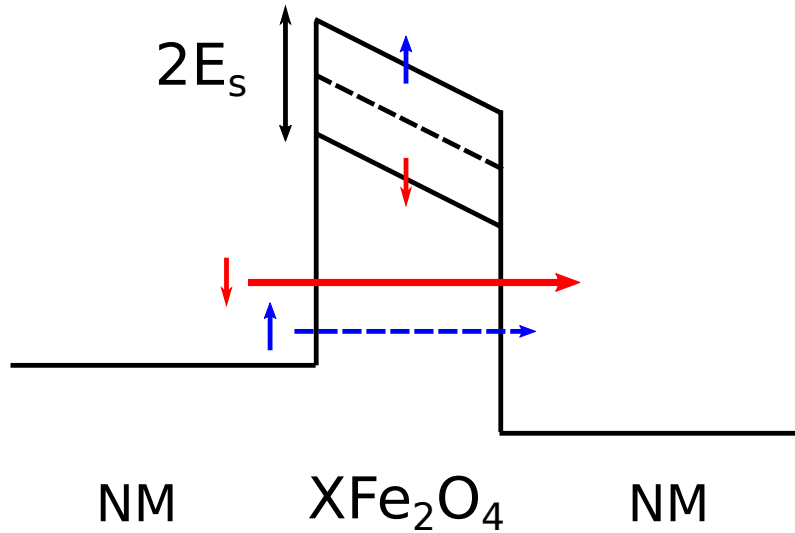


FIGURE 5.1: **Tunneling spin filter.** Sketch of the energy landscape of the tunneling spin filter junction. The non-magnetic (NM) sides of the junction are separated by a thin magnetic potential barrier (made of e.g. a ferrite labeled  $XFe_2O_4$ ), which is spin-split by the energy  $2E_s$ . This spin dependent barrier height leads to a spin-dependent tunneling probability and thereby to the majority spin filter effect.

## 5.2 Spin filter effect at magnetic/non-magnetic interfaces in ZnO

### 5.2.1 The spin filter effect

The spin filter effect or spin filter tunneling usually refers to a phenomenon that allows to generate highly spin-polarized currents using non-magnetic electrodes and magnetic semiconducting tunnel barriers. In the magnetically ordered state, the exchange splitting of the magnetic semiconductor's conduction band leads to a spin dependent tunnel barrier height (see Figure 5.1). As the tunneling probability exponentially depends on the barrier height,  $T(V_b; E) \sim \exp(-\sqrt{V_b - E})$ , even a small splitting of the order of several meV can lead to a substantial spin filtering effect. For an in-depth description of the effect, the reader is referred to the reviews by Moodera et al. [109] and Moussy [110] and references therein.

The spin filter effect was first observed in ferromagnetic Eu-chalcogenides in the 1970s [111–113] and later used to build spin-dependent tunnel barriers that would generate spin currents with a spin polarization approaching 100 % at cryogenic temperatures [114–116]. With the enormous research activity in the field of spintronics in the last two decades, a renewed interest in the spin filter effect appeared, owing to its potential to generate highly polarized spin currents. Notably, the spinel ferrites [110, 117–123] were investigated as spin-dependent tunnel barriers to achieve room temperature spin filtering. Although some results indicate successful spin filtering at room temperature, see Table 5.1, the structures require high quality interfaces and the resulting spin polarization was very low.

In contrast, artificial ferromagnets based on semiconducting host materials such as ZnO and created by ion irradiation provide a very flexible

Barrier Material	Temperature	$P_{sf}$	Reference
BiMnO <sub>3</sub>	3 K	22 %	Gajek 2005 [117]
NiFe <sub>2</sub> O <sub>4</sub>	4 K	22 %	Lüders 2006 [118]
CoFe <sub>2</sub> O <sub>4</sub>	2 K	25 %	Ramos 2007 [119]
CoFe <sub>2</sub> O <sub>4</sub>	290 K	4 %	Ramos 2007 [119]
CoFe <sub>2</sub> O <sub>4</sub>	10 K	44 %	Takahashi 2010 [120]
CoFe <sub>2</sub> O <sub>4</sub>	290 K	4.3 %	Takahashi 2010 [120]
CoFe <sub>2</sub> O <sub>4</sub>	290 K	8 %	Matzen 2012 [121]
MnFe <sub>2</sub> O <sub>4</sub>	0.45 K	6 %	Matzen 2013 [122]
$\gamma$ -Fe <sub>2</sub> O <sub>3</sub>	200 K	30 %	Li 2016 [123]

TABLE 5.1: Spin filter efficiencies measured in tunnel junctions made of different oxide tunneling barriers.

framework to engineer devices making use of interfacial spin transport effects. In the following sections, the influence of lithium and hydrogen doping on the properties of ZnO is discussed, followed by a short review of the magneto-transport properties of magnetic Li-doped ZnO. The spin transport through potential barriers at magnetic/non-magnetic interfaces in ZnO is then investigated experimentally, demonstrating the realization of an efficient minority spin filter at room temperature.

### 5.2.2 Lithium and hydrogen doping in ZnO

Under most growth conditions, ZnO has a tendency to develop intrinsic defects that act as electron donors and therefore, most ZnO samples exhibit n-type conduction. In fact, creating highly p-type ZnO with large hole concentrations is a long standing problem, as efficient acceptor dopants are still missing and most elements that can act as acceptors in ZnO simultaneously introduce donor states that compensate each other. Lithium is one such example, as it acts as an acceptor when substituting a lattice Zn atom and in the interstitial position, it acts as a donor [124, 125]. Although the inability to obtain highly p-type ZnO has been a prohibitive factor in its application in classical semiconductor applications, Li doping can still be used to control the electronic structure of the material.

The incorporation of Li acceptors in the form of Zn substitutionals brings some advantages. First, they allow to compensate the intrinsic donor defects, resulting in semi-insulating or even low density p-type conductive ZnO. This allows to tune the carrier concentration locally using ion implantation methods. As we will show in the next section, the implantation of H<sup>+</sup> ions introduces additional shallow donors and allows to vary the effective electron concentration by controlling the implantation dose. The second benefit of the Li acceptors is the role they play in the emergence of magnetic order in ZnO. The Li acceptors stabilize the formation of Zn vacancies, which are at the origin of the artificial ferromagnetism in ZnO [21, 32, 89, 126].

The same H<sup>+</sup> ion implantation process used to introduce shallow donor states can be used to create Zn vacancies and trigger magnetic order, as demonstrated in Li-doped ZnO microwires, irradiated with low energy H<sup>+</sup> ions [32]. By implanting H<sup>+</sup> ions with a low energy of 300 eV, H-donors as well as Zn vacancies are created in a thin region  $\lesssim 10$  nm below the

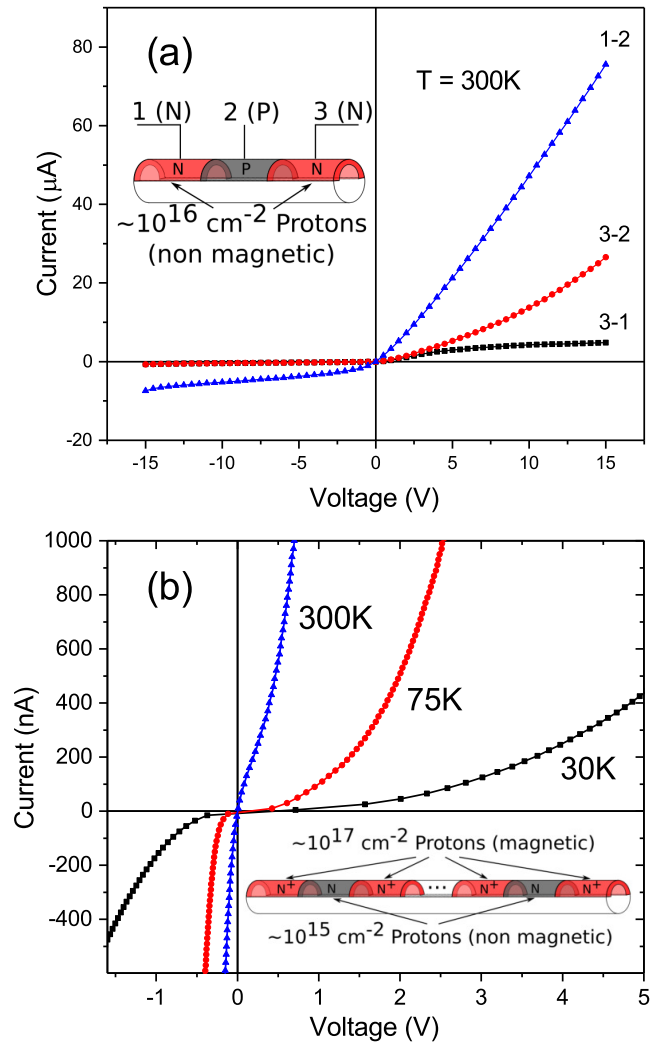


FIGURE 5.2: **Current-voltage characteristics.** (a) I-V-characteristics of a lateral N-P-N diode created at the surface of a Li doped ZnO microwire, measured at  $T = 300\text{ K}$ . Characteristics of the two PN diodes (between contacts 1-2 in blue, and 3-2 in red) and the whole N-P-N device (between contacts 3-1 in black) are shown. The N-regions are implanted with a proton dose of  $10^{16}\text{ cm}^{-2}$ . (b) I-V-characteristics of a magnetic  $\text{N}^+\text{-N-N}^+$  device with 37  $\text{N}^+\text{-N}^+$  junctions, measured at temperatures of 30 K, 75 K and 300 K.

Li:ZnO microwire surface [127]. By varying the implantation dose, the carrier concentration in the implanted region can be controlled within a wide range and the Zn vacancy concentration can be varied in order to control the magnetic percolation and the emergence of an artificial ferromagnetic phase.

For the experimental investigations described in this chapter, we grew Li doped ZnO microwires using a carbothermal reduction process. ZnO powder was mixed with LiOH and graphite powder. The mixed precursor was milled and pressed to a pellet. The pellet was then heated in a tubular furnace to 1200 °C at a rate of 5 °C/min, at which point the following reduction reactions take place [128, 129]:

1.  $\text{ZnO(s)} + \text{C(s)} + \text{CO}_2\text{(g)} \rightarrow \text{ZnO(s)} + 2\text{CO(g)} \rightarrow \text{Zn(g)} + \text{CO}_2\text{(g)}$
2.  $2\text{LiOH} + 2\text{C} \rightarrow 2\text{Li(g)} + \text{H}_2\text{(g)} + \text{CO(g)}$

Under a constant flow of oxygen, the reduced metals were transferred to a cooler region of the furnace and recrystallized, creating Li:ZnO microwires growing preferentially in the (0001) crystal direction. Depending on the oxygen flow, the thickness and length of the wires can vary. The wires used in this work contain a nominal Li concentration of 3 %, have a diameter of  $\simeq 1 \mu\text{m}$  and a typical length ranging from 100  $\mu\text{m}$  to 500  $\mu\text{m}$ .

We demonstrate the ability to control the carrier concentration and prepare a localized high ohmic region along the main axis of a Li:ZnO microwire ( $\parallel$  to the  $c$  axis of the ZnO structure) by creating two diodes at its surface. The left and right side of the wire was implanted with  $\text{H}^+$  ions at a fluence of  $10^{16} \text{ cm}^{-2}$ , as sketched in the inset of Figure 5.2 (a). The central region of the wire was not implanted. Curves 1-2 (measured between contacts 1 and 2) and 3-2 (measured between contacts 3 and 2) in Figure 5.2 (a) show the I-V characteristics of the two PN-diodes, respectively. The current through the diodes is limited by the low hole concentration in the unimplanted, high ohmic central region of the wire. Curve 3-1 (measured between contacts 3 and 1) shows the I-V characteristic of the two diodes measured in series with its diode-leak currents in both bias voltage directions. We note that the electrical resistance of the bulk of the Li:ZnO microwire beneath its irradiated surface has a very high resistance and therefore only this thin near surface region and the localized potential well in-between play a role in the transport properties.

When we implant the P-region at a  $\text{H}^+$  fluence  $< 10^{16} \text{ cm}^{-2}$ , the I-V characteristic changes. Instead of the leak current measured across the N-P-N structure (curve 3-1 in Figure 5.2(a)), we observe a current increasing with the applied bias voltage. The barrier of the P-N diodes is reduced as the P region becomes N-type conducting. Increasing the fluence in the central region, we observe an increasing current until the I-V characteristics become linear at a fluence of  $10^{16} \text{ cm}^{-2}$ . By introducing donor defects in the P-region, we effectively built a  $\text{N}^+ \text{-N-N}^+$  structure, where  $\text{N}^+$  denotes a region with high donor concentration and N one with a lower donor concentration. At the interface between the regions, a potential barrier is built up. Its height is:

$$V_b^0 = k_B T \log \left( \frac{N^+}{N} \right), \quad (5.1)$$

where  $k_B$  is the Boltzmann constant,  $T$  the temperature and  $N^+ > N$  the carrier concentrations at the two sides of the barrier.

Figure 5.2 (b) shows the I-V characteristics of a wire (S1), where we created 37 such  $N^+ \text{-} N \text{-} N^+$  structures along the wire's main axis. We used a fluence of  $10^{17} \text{ cm}^{-2}$  in the  $N^+$  regions and  $10^{15} \text{ cm}^{-2}$  in the  $N$  regions (see inset in Figure 5.2 (b)).

To extract the potential barrier height from the I-V characteristics of the  $N^+/N$  structures, we model our structure as a diode with a series resistance. We take into account the deviation from ideal thermionic behavior by including the ideality factor  $n$ . The I-V characteristics are then described by

$$I = A_{\text{eff}} A^{**} T^2 \exp\left(-\frac{eV_b}{k_B T}\right) \exp\left(\frac{e(V - IR_s)}{nk_B T}\right), \quad (5.2)$$

where  $A_{\text{eff}}$  is the effective diode area,  $A^{**}$  the Richardson constant,  $T$  the temperature,  $e$  the electron charge,  $V_b$  the barrier height,  $k_B$  the Boltzmann constant and  $R_s$  the series resistance. Following the method described by Cheung and Cheung [130], we extract the ideality factor  $n$  from  $d(V)/d(\ln I)$  plots and define the function

$$H(I) = V - \frac{nk_B T}{e} \ln\left(\frac{I}{A_{\text{eff}} A^{**} T^2}\right) = IR_s + nV_b. \quad (5.3)$$

Figures 5.3 and 5.4 show the function  $H(I)/n$  corresponding to I-V characteristics measured at different temperatures and applied magnetic fields. The y-axis intercept gives us the barrier height  $V_b$  and the slope gives us the series resistance  $R_s$ . Figure 5.5 shows the series resistance  $R_s(T)$  as function of temperature. Assuming the series resistance is dominated by the high ohmic  $N$  regions, we can estimate the carrier density in these regions. We define the conductivity in the  $N$  region:

$$\sigma = \frac{l}{AR_s} = en\mu, \quad (5.4)$$

where  $A$  is the cross section area and  $l$  the length of the conduction channel,  $e$  the electron charge,  $n$  the carrier density and  $\mu$  the mobility. The carrier density depends on temperature:

$$n(T) = n_0 T^{3/2} \exp\left(-\frac{\Delta E}{k_B T}\right). \quad (5.5)$$

Using Equation (5.4) and Equation (5.5), we fit the function

$$R_s(T) = l/(Aen(T)\mu) \quad (5.6)$$

shown as a line in Figure 5.5 and obtain  $n_0\mu \simeq 10^{12} \text{ cm}^{-1}/(\text{Vs})$ . Assuming the carrier density  $n_0$  is only due to the H donors introduced by  $H^+$  implantation and ignoring the temperature dependence of the mobility, we obtain a mobility  $\mu \simeq 150 \text{ cm}^2/(\text{Vs})$ .

By analyzing the I-V characteristics in this way, we find a ratio of the carrier concentration  $N^+/N \simeq 100$ , which matches the ratio of  $H^+$  implantation fluences. We will come back to the analysis of the I-V characteristics later when we take a closer look at the potential barrier.

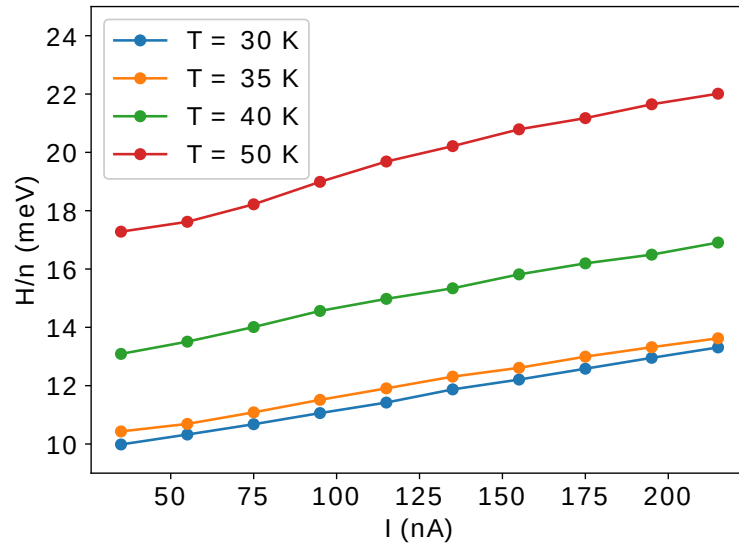


FIGURE 5.3: Function  $H(I)/n$  (Equation (5.3)) at different temperatures in the range 30 – 50 K and zero magnetic field, used to determine the potential barrier height from measurements of the current-voltage characteristics. The solid lines are a guide to the eye.

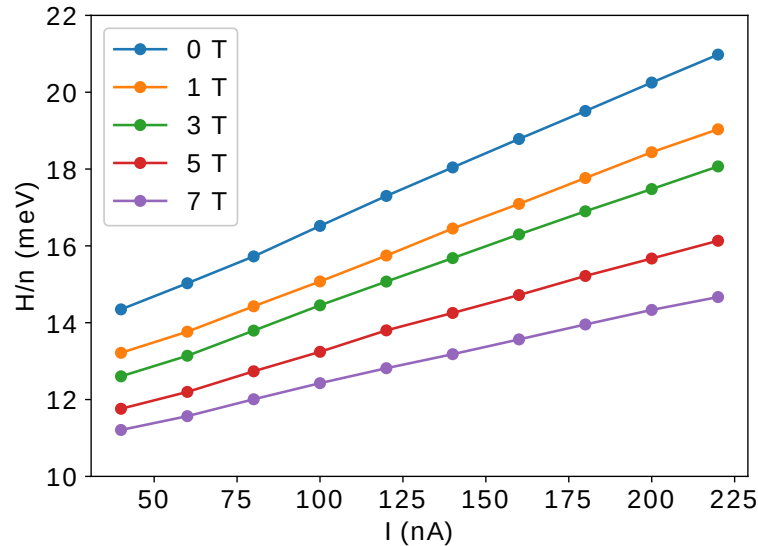


FIGURE 5.4: Function  $H(I)/n$  (Equation (5.3)) at different applied magnetic fields in the range 0 – 7 T and  $T = 35$  K, used to determine the potential barrier height from measurements of the current-voltage characteristics. The solid lines are a guide to the eye.

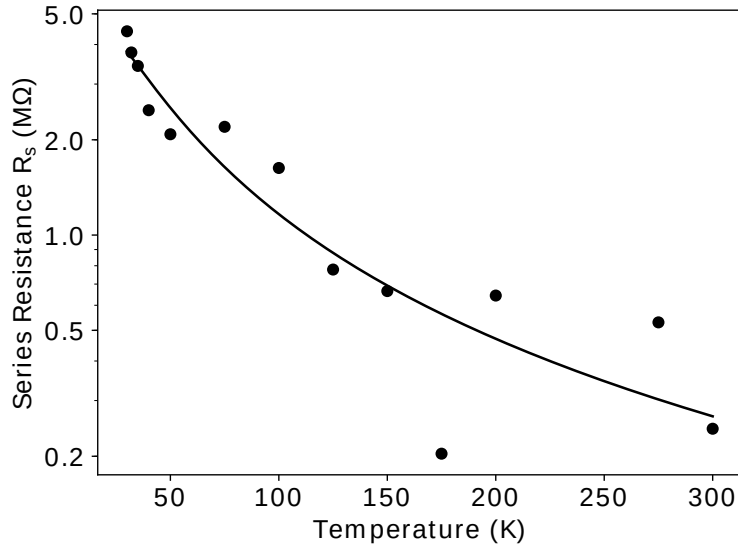


FIGURE 5.5: Series resistance as function of temperature. The line shows the fit of function  $R_s(T) = l/(Aen\mu)$  defined using Equation (5.4) and Equation (5.5).

We should note that ideally, the structures should be symmetric and therefore we would expect the I-V characteristics of the two PN diodes in Figure 5.2 (a) to be equivalent and those of the  $N^+/N$  structures shown in Figure 5.2 (b) to be symmetric, which is clearly not the case. We attribute this to charging effects occurring during the first  $H^+$  implantation. The potential barriers created at both sides of the highly implanted regions by the implantation process are not equal, i.e. the height of the barriers seen at one current polarity is different from that seen at the other polarity. We have seen this difference in every sample prepared in this way. We will therefore treat the two current polarities independently and analyze in detail the positive current polarity (as defined in Figure 5.2(b)) with the higher potential barriers.

An interesting side-effect of the  $H^+$  implantation allows us to visualize the magnetic  $N^+/N$  structures created along the surface of the Li doped ZnO microwires. As shown in Figure 5.6 (a),  $H^+$  implantation affects the photoluminescence emission spectrum of Li:ZnO. The emission spectrum of a Li doped ZnO wire is shown after implanting  $1.0 \times 10^{17} \text{ cm}^{-2}$ ,  $5.0 \times 10^{16} \text{ cm}^{-2}$  and  $2.5 \times 10^{15} \text{ cm}^{-2}$   $H^+$  ions respectively. It is known that ZnO mainly emits in two broad spectral ranges, namely the UV emission around 380 nm attributed to the recombination of free excitons and their phonon replica and the visible green emission between 450 and 600 nm attributed to defect levels, such as Zn vacancies [131].  $H^+$  implantation reduces the visible green emission intensity compared to that of the UV emission. Therefore, the intensity contrast UV/VIS is a good indicator for the  $H^+$  concentration along the implanted wires. Figure 5.6(b) shows the photoluminescence emission spectrum scanned along the axis of a wire prepared with  $N^+/N$  junctions. The different regions are clearly discernible: The magnetic  $N^+$  regions implanted with a fluence of  $10^{17} \text{ cm}^{-2}$  show high emission intensity in the UV range and low intensity in the visible, whereas



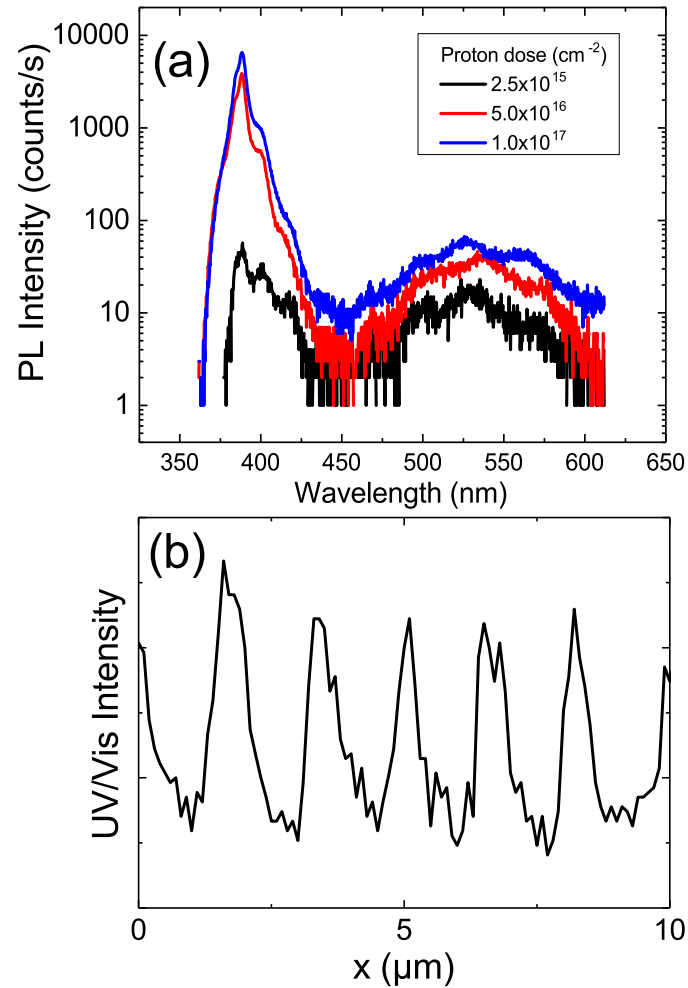


FIGURE 5.6: **Photoluminescence spectra.** (a) Photoluminescence spectra of Li:ZnO microwires after implanting a dose of  $1.0 \times 10^{17} \text{ cm}^{-2}$ ,  $5.0 \times 10^{16} \text{ cm}^{-2}$  and  $2.5 \times 10^{15} \text{ cm}^{-2}$  protons respectively. With increasing proton dose, the contrast between UV- and visible emission increases. (b) Ratio of the UV (380 nm) over the visible (540 nm) photoluminescence intensity scanned along the main axis of a typical microwire with multiple magnetic  $\text{N}^+$ /N junctions. The magnetic  $\text{N}^+$  regions show high UV/Vis contrast, whereas the non-magnetic N regions show low contrast.

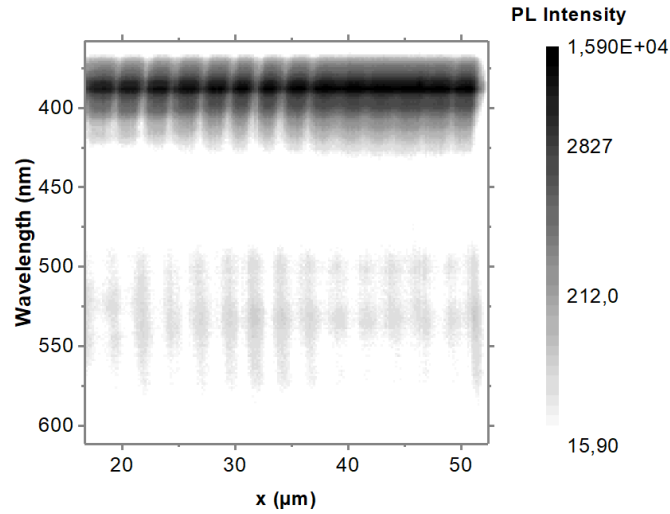


FIGURE 5.7: Photoluminescence map of magnetic interfaces along ZnO microwire.

the non-magnetic N regions implanted with a fluence of  $2.5 \times 10^{15} \text{ cm}^{-2}$  show lower UV and higher visible emission intensity.

### 5.2.3 Magneto-transport in artificial ferromagnetic Li:ZnO microwires

According to several reports in the literature [32, 89, 132–136], the implantation of  $\text{H}^+$  ions in the Li:ZnO microwires creates Zn vacancies that can trigger magnetic order. The dangling O-bonds surrounding a Zn vacancy give rise to a localized magnetic moment  $m \simeq 2\mu_B$ . At Zn vacancy densities  $\gtrsim 3\%$ , these localized magnetic moments can couple ferromagnetically. A fluence of  $\sim 10^{17} \text{ cm}^{-2}$  creates defect concentrations large enough to induce a ferromagnetic phase in Li-doped ZnO microwires, as clearly demonstrated in previous studies, including magnetometric (SQUID), element specific X-Ray absorption (XAS) and magnetic dichroism (XMCD) experiments [32].

When we implant a Li:ZnO microwire with a fluence of  $10^{17} \text{ cm}^{-2}$  and measure its magnetotransport properties, the magnetoresistance response is typically negative, as shown in Figure 5.8. This negative magnetoresistance (defined as  $(R(B) - R(0))/R(0)$ ,  $B$  is the applied magnetic field) is expected for magnetic ZnO [127, 137] and indicates the creation of a magnetic surface along the main microwire axis. This sample shows linear I-V characteristics (not shown here).

### 5.2.4 Spin transport through magnetic/non-magnetic interfaces

Ion implantation gives us the ability to modify the electronic and magnetic properties of the Li:ZnO microwire surface locally, i.e. in selected regions along the wire main axis. By means of a standard lithographic process, we create a mask on top of the microwire to implant  $\text{H}^+$  ions only in selected regions along the wire, as sketched in Figure 5.9. The inset shows a SEM

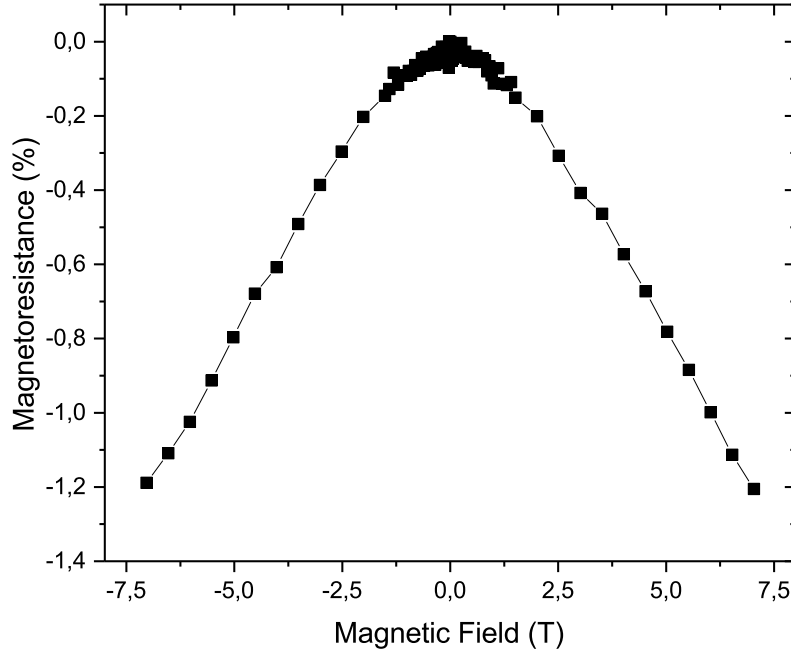


FIGURE 5.8: **Magnetoconductance of magnetic ZnO** Magnetoconductance at a temperature of  $T = 30$  K of a Li:ZnO microwire implanted with a dose of  $10^{17} \text{ H}^+ \text{ cm}^{-2}$  along its whole length. The negative magnetoconductance of  $-1.2\%$  at an applied magnetic field of 7 T is expected for magnetic ZnO.

image of such a mask created at different positions along the length on a Li:ZnO microwire and across its width.

We create magnetic regions using a fluence of  $10^{17} \text{ cm}^{-2}$  in a first implantation step, where parts of the wire remain covered. After removing the mask, we implant the whole wire using a low fluence of  $10^{15} \text{ cm}^{-2}$  in order to tune the carrier concentration. This two-step implantation process creates potential barriers between magnetic  $\text{N}^+$ -doped and non-magnetic N-doped regions, as described above. The I-V characteristics of such a sample with 37 consecutive potential barriers is shown in Figure 5.2 (b). The magnetotransport properties of this microwire (S1) are completely different from those expected of a magnetic wire. Figures 5.10 (a) and 5.10 (b) show the magnetoconductance measured at temperatures ranging from 25 K to 300 K.

We observe that the magnetoconductance is positive in the whole temperature range and its magnitude is up to two orders higher than that shown in Figure 5.8. At low temperatures (Figure 5.10), the magnetoconductance reaches a maximum of 300 % at 30 K and drops to 50 % at 25 K. It increases rather linearly with field and tends to saturate at high fields and at low enough temperatures.

Figure 5.11 (a) (right axis) shows the magnitude of the magnetoconductance at a magnetic field of 7 T applied along the microwire S1, measured in the temperature range 25 K ... 300 K (black squares). Note that the resistance increases exponentially to lower temperatures reaching the resistance resolution limit of standard lab equipment. Although the electrometer used for the resistance measurements in this experiment is able to measure  $10^{12} \Omega$

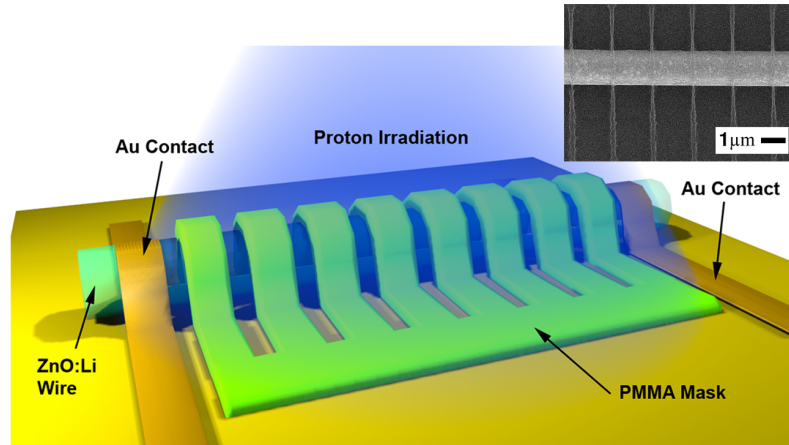


FIGURE 5.9: Sketch of the masked  $H^+$  ion implantation process using a lithographically created mask to cover parts of the wire during implantation. The inset shows a SEM image of such a mask on a Li:ZnO microwire, of 50 nm length and 1  $\mu\text{m}$  spaced along the wire main axis.

with an accuracy of 0.35 %, it is necessary to exclude possible, unknown sources of measurement errors. Therefore, to reduce the resistance of the sample, we implanted an additional fluence of  $5 \times 10^{15} \text{ cm}^{-2}$  at the surface of wire S1. The resistance at zero field was then measured again in the temperature range 20 K ... 50 K as shown in Figure 5.11 (b) (red squares). Now, the resistance stays below 100 M $\Omega$  down to 20 K. We measured the resistance in the same temperature range at a field of 7 T reaching 100 M $\Omega$  at 20 K (red circles). The magnetoresistance calculated from these measurements (black squares, right axis) clearly shows a maximum of 150 % around 30 K.

We note that the magnitude of the magnetoresistance decreased after the additional implantation step. In fact, the magnetoresistance decreases with each additional implantation step. Figure 5.12 (a) shows the magnetoresistance of wire S1 after implanting additional  $H^+$  ions, measured at 30 K in the field range -7 T ... 7 T applied along the wire axis. At a total implantation fluence of  $3.7 \times 10^{16} \text{ cm}^{-2}$ , the magnetoresistance becomes negative. The decrease of the magnetoresistance is accompanied by the I-V characteristics becoming linear after a total implantation fluence of  $3.7 \times 10^{16} \text{ cm}^{-2}$ . This fluence appears to saturate the amount of  $H^+$  dopants that can be incorporated into the ZnO microwires, as further implantation up to a total fluence of  $1 \times 10^{17} \text{ cm}^{-2}$  does not significantly affect the measured characteristics.

The correlation between non-linearity of the I-V characteristics and the observed positive magnetoresistance indicates the importance of the potential barrier built at the boundaries between the regions with high/low  $H^+$  concentration. In fact, the positive magnetoresistance vanishes when the  $H^+$  concentration reaches a saturation level homogeneously distributed along the whole wire.

The importance of the potential barriers becomes even more apparent when we look at the magnetoresistance of other samples, prepared in a similar way, but varying the number of consecutive potential barriers along

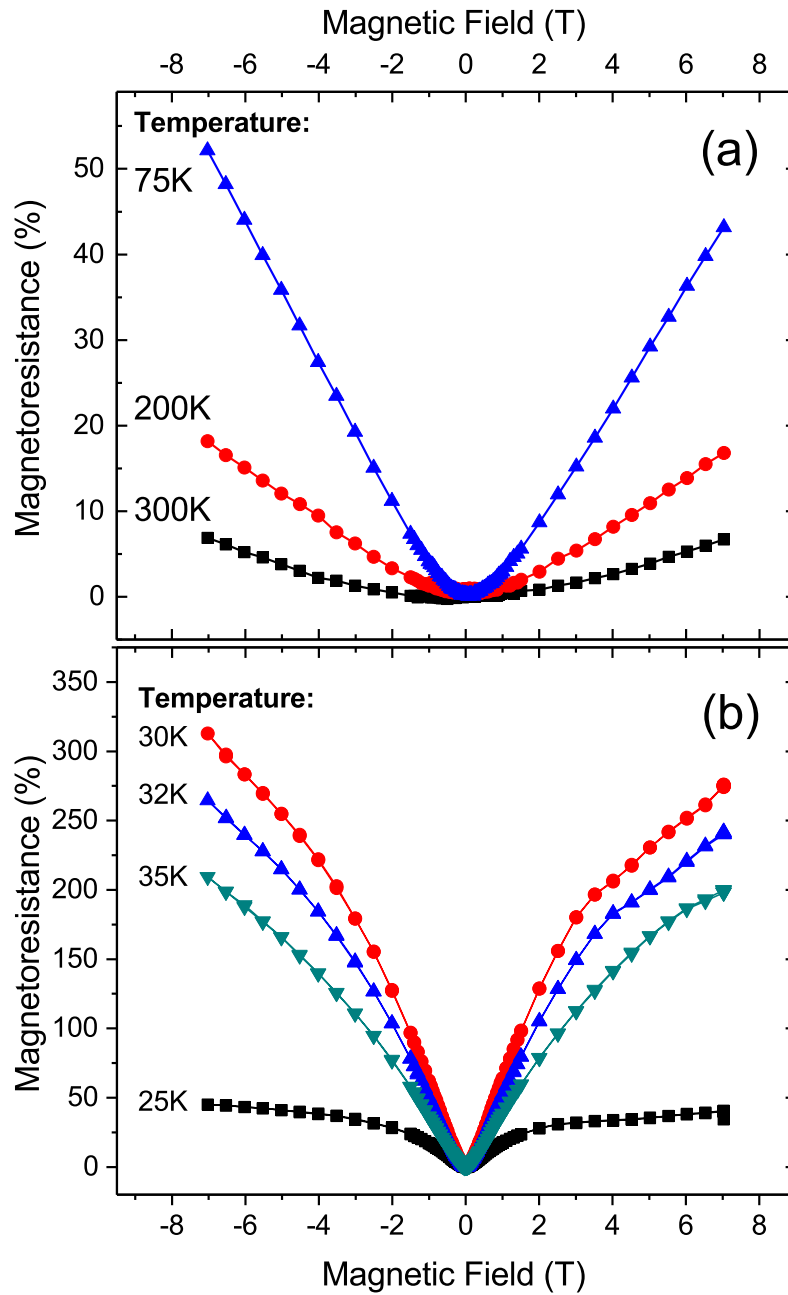


FIGURE 5.10: **Magnetoresistance** of the Li:ZnO microwire S1, with 37 alternating regions implanted with  $10^{17} \text{H}^+ \text{cm}^{-2}$  and  $10^{15} \text{H}^+ \text{cm}^{-2}$  respectively, measured at a temperature of (a) 300 K, 200 K, 75 K and (b) 35 K, 32 K, 30 K, 25 K. The magnetic field was applied along the wire axis in the range of -7 T to 7 T.

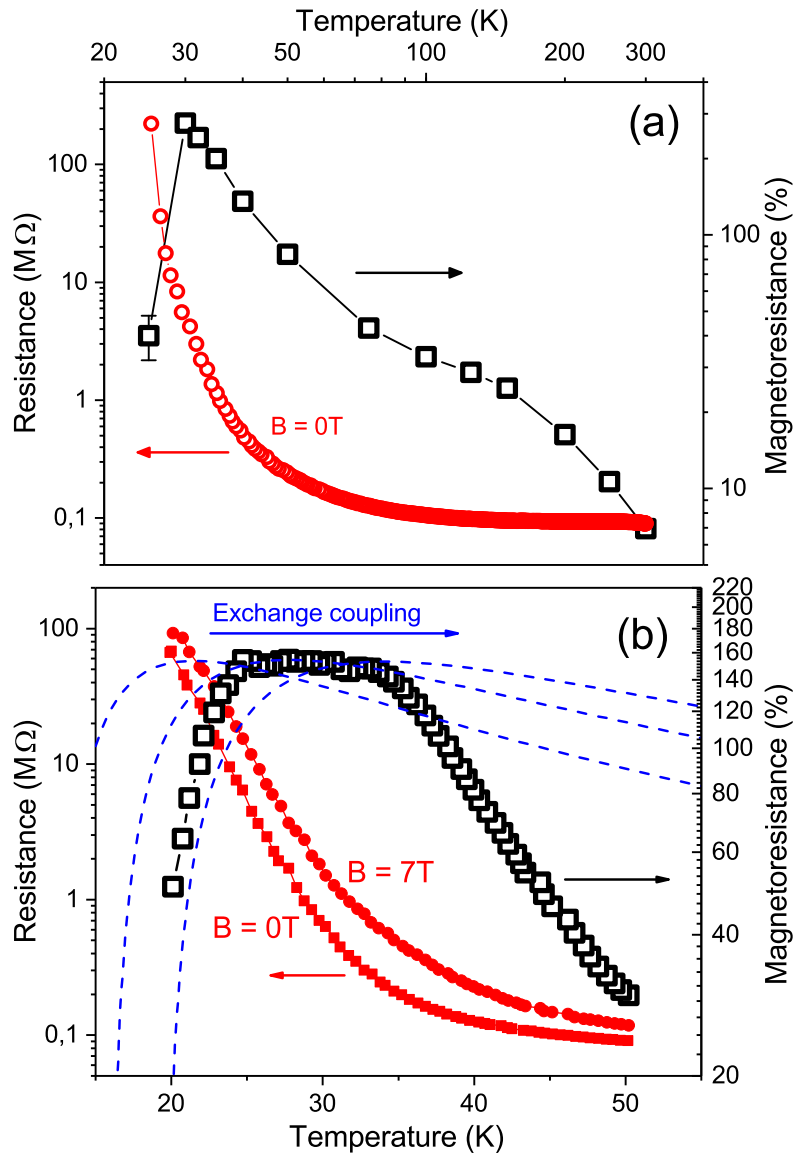


FIGURE 5.11: (a) Resistance of the as-prepared surface layer of wire S1 measured in the temperature range 25 K – 300 K (red circles), magnetoresistance of S1 at a magnetic field of 7 T applied along the wire axis (black squares). (b) Resistance of wire S1 after an additional implantation of  $5 \times 10^{15} \text{ cm}^{-2} \text{ H}^+$  ions, measured in the temperature range 20 K – 50 K at zero applied magnetic field (red squares) and a magnetic field of 7 T applied along the wire axis (red circles). Magnetoresistance at a field of 7 T applied along the wire axis (black squares). The dashed blue lines show the magnetoresistance calculated using the thermionic emission model (Equation (5.12)) explained in Section 5.2.5, for three values of the exchange coupling strength  $E_{ex}$  (1.5 meV, 2 meV and 2.5 meV).

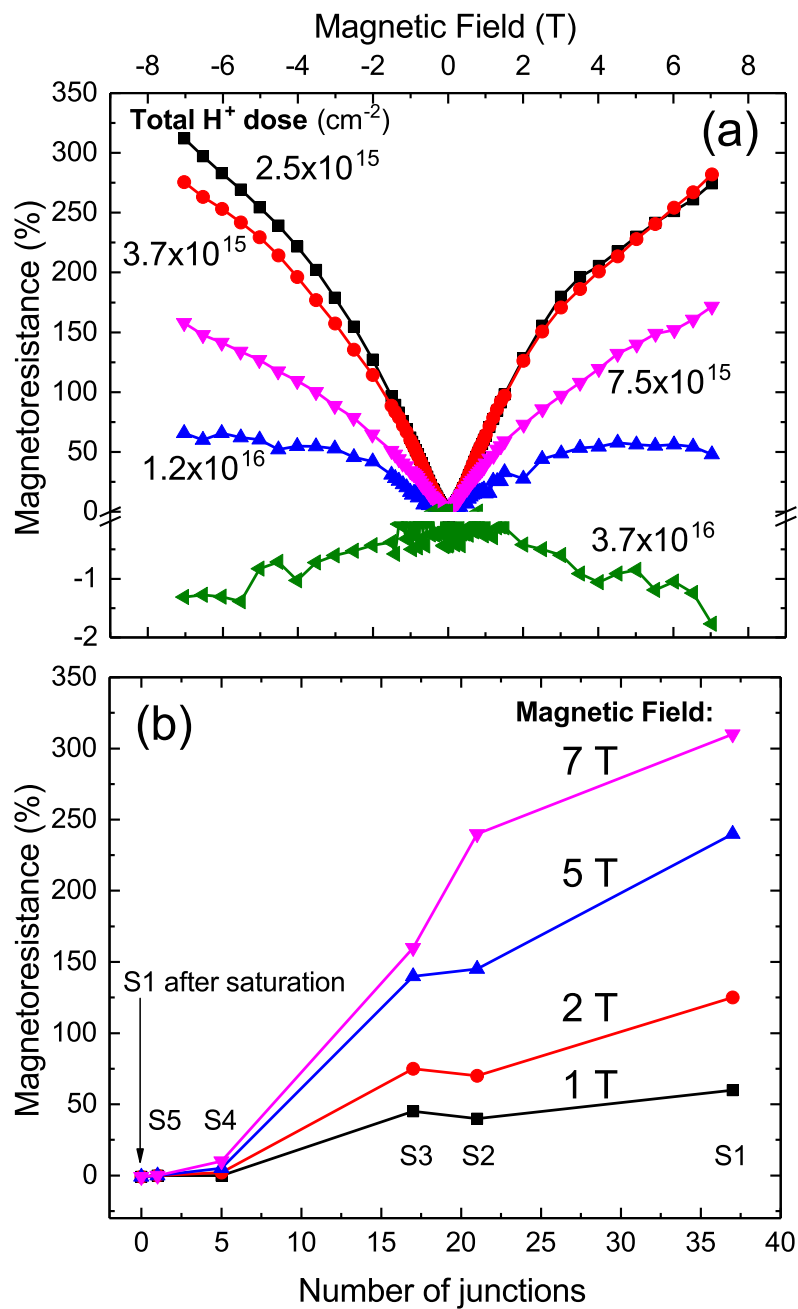


FIGURE 5.12: (a) Magnetoresistance of wire S1 after implanting an additional dose of  $2.5 \times 10^{15} \text{ cm}^{-2}$ ,  $3.7 \times 10^{15} \text{ cm}^{-2}$ ,  $7.5 \times 10^{15} \text{ cm}^{-2}$ ,  $1.2 \times 10^{16} \text{ cm}^{-2}$  and  $3.7 \times 10^{16} \text{ cm}^{-2} H^+$  ions in the whole wire (without any mask), measured at 30 K and magnetic field applied along the wire axis. (b) Magnetoresistance of wires S1-S5, measured at 30 K and magnetic field applied along the wire axis of 1 T, 2 T, 5 T and 7 T. The x-axis indicates the number of consecutive junctions created along the wire main axis in each sample.

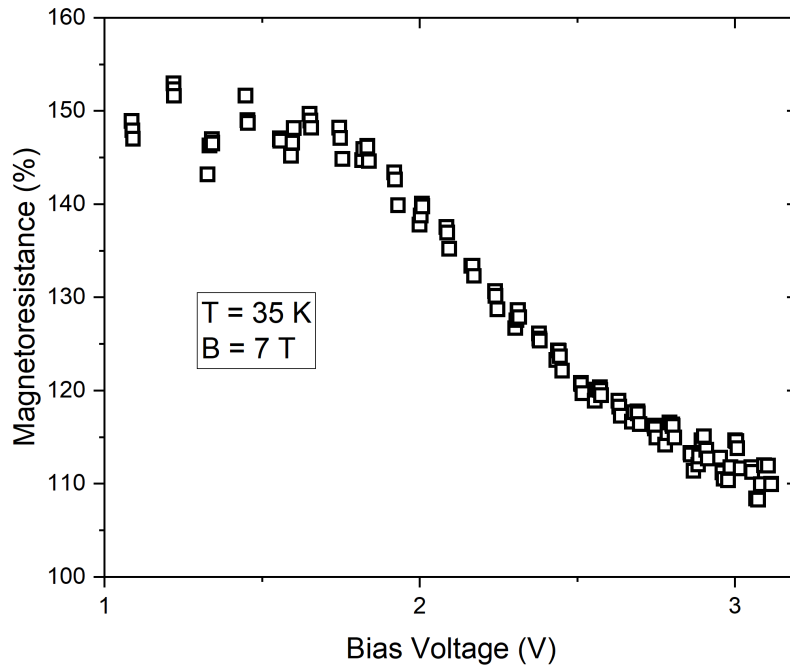


FIGURE 5.13: Magnetoresistance of wire S1 after an additional implantation of  $5 \times 10^{15} \text{ cm}^{-2} \text{ H}^+$  ions, measured by applying a bias voltage in the range 1 – 3 V, a magnetic field of 7 T applied along the wire main axis and at a temperature of 35 K.

the wires axis. Figure 5.12 (b) shows the maximum value of the magnetoresistance of the samples S1-S5 with 37, 21, 17, 5 and 1 potential barriers respectively, measured at 30 K and a magnetic field of 1 T, 2 T, 5 T and 7 T applied along the wires main axis. The wires have a diameter of  $1 \mu\text{m}$  and a distance between the electrodes of  $200 \mu\text{m}$ ,  $180 \mu\text{m}$ ,  $200 \mu\text{m}$ ,  $100 \mu\text{m}$  and  $80 \mu\text{m}$  respectively. We observe that the magnitude of the positive magnetoresistance scales rather linear with the number of potential barriers (see Figure 5.12 (b)).

As indicated in Equation (5.2), the effective barrier height can be tuned by varying the applied bias voltage. Figure 5.13 shows the magnetoresistance of wire S1 after an additional implantation of  $5 \times 10^{15} \text{ cm}^{-2} \text{ H}^+$  ions, measured by applying a bias voltage in the range 1 – 3 V, a constant magnetic field of 7 T and at a temperature of 35 K. The magnetoresistance decreases increasing the bias voltage, which translates to a decrease of the effective barrier height (Equation (5.2)).

Figure 5.14 shows the magnetoresistance of the as-prepared surface layer of sample S1 measured at an applied field of 7 T in the temperature range 25 – 300 K, by applying different bias voltages. At temperatures  $T \geq 30 \text{ K}$ , the magnetoresistance decreases increasing the bias voltage. Below  $T = 30 \text{ K}$ , where we see the maximum of the magnetoresistance, the behaviour is reversed. A bias voltage of 2 V yields a higher magnetoresistance as a bias of 1 V.

We commented about the asymmetry of the I-V characteristics and argued that the two current polarities can be viewed as two different devices



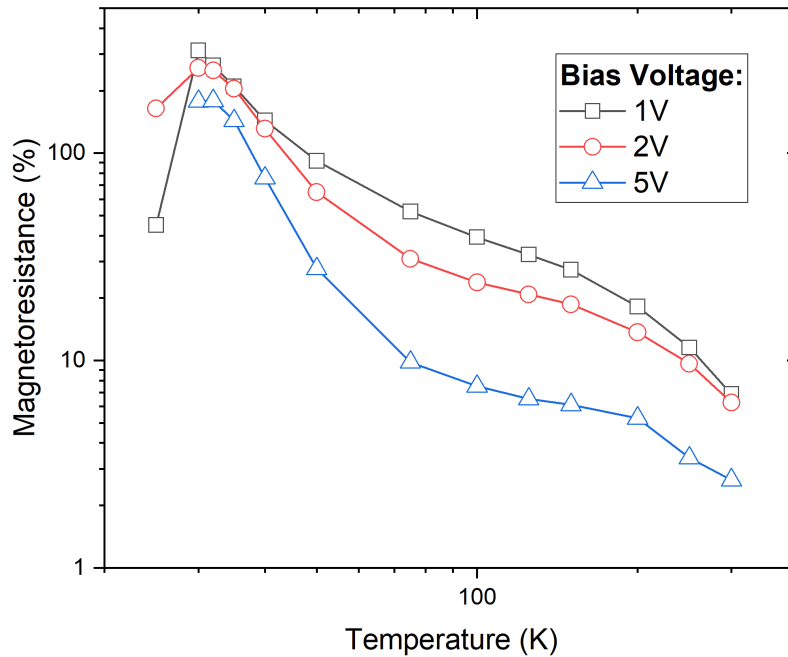


FIGURE 5.14: Magnetoresistance of the as-prepared surface layer of sample S1 measured at an applied field of 7 T in the temperature range 25 – 300 K, by applying a bias voltage of 1 V (black squares), 2 V (red circles) and 5 V (blue triangles).

with different barriers. In fact the magnetoresistance observed at one current polarity is also present in the other current direction, although the effect is much weaker. Figure 5.15 shows the magnetoresistance as a function of applied magnetic field, at  $T = 30\text{K}$  (a) and  $T = 35\text{K}$  (b). The black curves were measured with the positive current polarity described in detail above (see Figures 5.10 and 5.10) and the red curves were measured with inverted current polarity. Although the extraction of the much smaller barrier height at the inverted current polarity from the I-V curves is difficult, analyzing the high temperature I-V curves we estimate it to be three times smaller than at positive polarity.

All these observations call for a more in depth analysis of the potential barrier itself. To extract the potential barrier height from the I-V characteristics of the  $N^+/N$  structures, we use the method outlined above. Figure 5.16 shows the barrier height  $V_b$  extracted from I-V curves measured in the temperature range 30 K ... 300 K at zero applied magnetic field. From Equation (5.1), we see that  $V_b$  linearly increases with temperature  $T$  and depends on the ratio  $N^+/N$  of carrier concentrations on both sides of the barrier. Using a least squares fit (shown as a line in Figure 5.16), we find a ratio  $N^+/N \simeq 100$ . Interestingly, the best fit shows a negative offset of  $V_b(T = 0\text{K}) = -8 \pm 2$  meV. We repeated the same process for the other samples (not shown) and all fits yield a similar negative offset. As we will show later, this offset can be explained by the exchange interaction in the magnetic side of the barrier. Figure 5.17 shows the barrier height extracted from I-V curves measured at a constant temperature  $T = 35$  K while applying a magnetic field in the range 0 T ... 7 T. The barrier height slightly decreases increasing the magnetic field. The linear fit (shown as a line in Figure 5.17) reveals that this decrease is in fact equal to the Zeeman energy

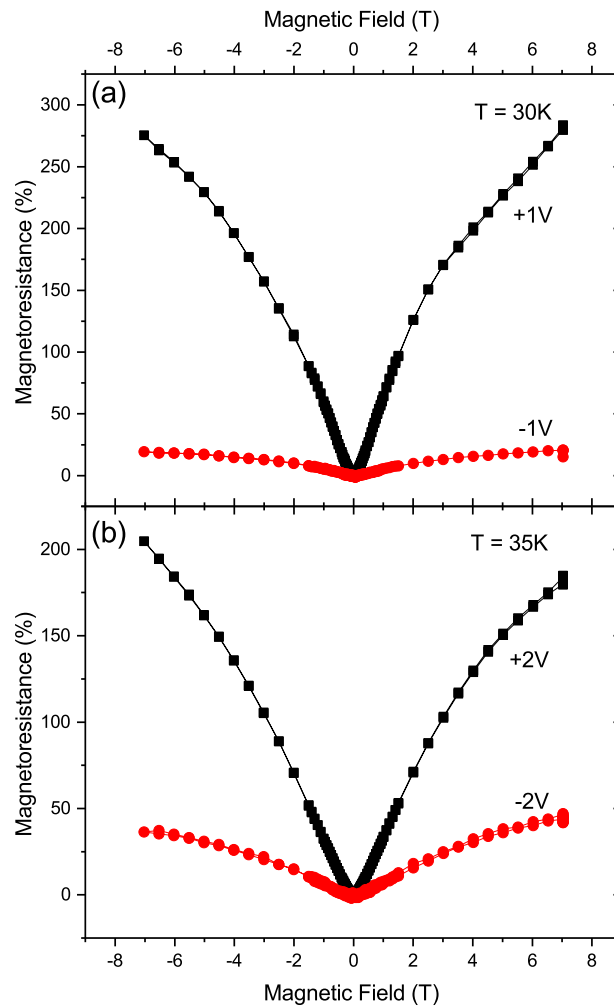


FIGURE 5.15: Magnetoconductance as a function of applied magnetic field, at  $T = 30\text{K}$  (a) and  $T = 35\text{K}$  (b), measured in sample S1. The black curves were measured with the positive current polarity (see Figure 5.2(b)) and the red curves were measured with inverted current polarity with a bias voltage as indicated.

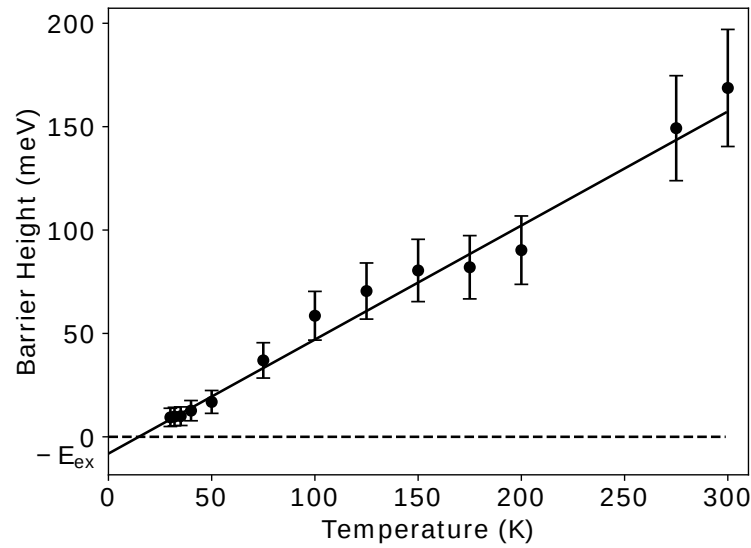


FIGURE 5.16: Potential barrier height, extracted from the I-V characteristics of sample S1 measured at zero magnetic field in the temperature range 30 K ... 300 K. The solid line is a fit to the data. The potential barrier height has a negative offset at  $T = 0$  K, which is equal to the exchange coupling strength  $-E_{ex}$ .

$g\mu_B B$  and yields a  $g$ -factor of 5.4 ( $\mu_B$  is the Bohr magneton).

### 5.2.5 Minority spin filter effect

In summary, we observe a positive magnetoresistance effect which is closely linked to the potential barrier built at the interface of magnetic/non-magnetic  $N^+/N$  junctions. The temperature dependence of the barrier height yields a negative offset at  $T = 0$  K and decreases by an amount equal to the Zeeman energy when a magnetic field is applied. We will now explain this effect.

A positive magnetoresistance effect could potentially have different origins as, for example, the disorder introduced in the samples by ion implantation. It is well known that disorder can give rise to orbital magnetoresistance effects explained by weak localization theory. These effects have been observed in several ZnO samples [138–144]. However, we note that these weak localization effects are observable at very low temperatures. The reported positive magnetoresistance in ZnO related to weak localization usually vanishes at temperatures above 20 K. On the other hand, the positive magnetoresistance effect we observe after creating the non-magnetic potential well between magnetic regions persists up to room temperature. Furthermore, it is very unlikely that the lattice disorder introduced by the ion implantation is by itself the origin of the huge positive magnetoresistance effect we report here, considering that this effect vanishes (and changes sign) increasing the lattice disorder, see Figure 5.12 (a).

On the other hand, we need to consider spin-related mechanisms leading to positive magnetoresistance. Figure 5.18 shows a sketch of the conduction electron energy landscape along a Li:ZnO microwire with a highly

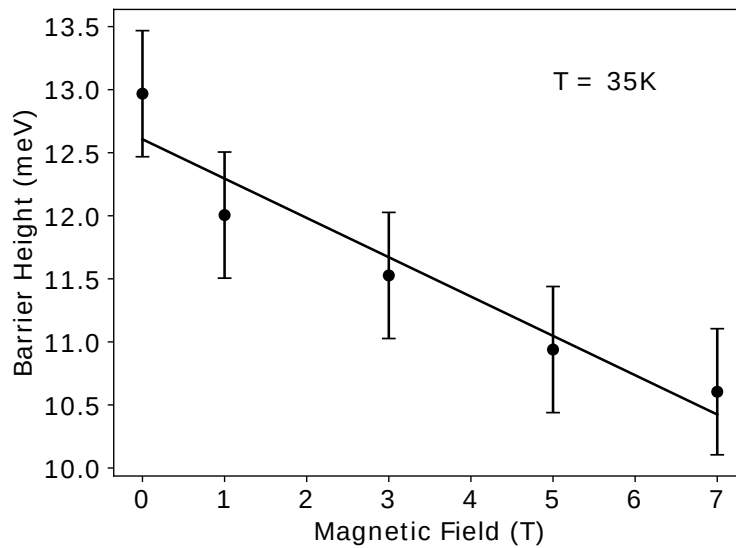


FIGURE 5.17: Potential barrier height, extracted from the I-V characteristics of sample S1 measured at  $T = 35$  K, while applying a magnetic field in the range 0 T ... 7T along the wire main axis. The solid line is a fit to the data. The potential barrier height decreases linearly with the applied magnetic field, with a slope of  $-5.4\mu_B$ .

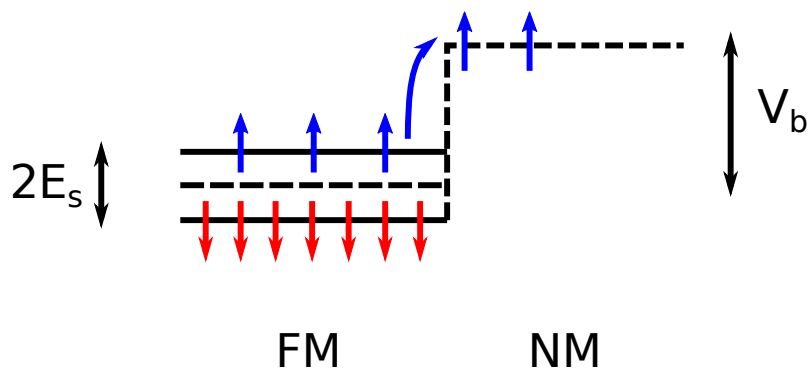


FIGURE 5.18: Sketch of the energy landscape along a Li:ZnO microwire with a highly donor doped magnetic region (FM) on the left hand side and less doped NM region on the right hand side. The dashed line represents the energy of the conduction band minimum along the wire. In the FM region, the conduction band is spin-split, indicated by the solid lines offset by spin-splitting energy  $\pm E_s$ . At the interface between the two regions, the potential barrier of height  $V_b$  is shown as a step. The blue/red arrows symbolize spin up/down electrons.

doped magnetic and less doped non-magnetic region (such as samples S1-S5), denoted FM and NM, respectively. The blue and red arrows symbolize spin-up (minority) and spin-down (majority) electrons respectively.

In the magnetic (FM) regions a spin-polarized defect band exists near the valence band maximum [32], which induces a spin polarization in the conduction band, due to recombination processes. At the boundary between the FM and NM regions, the conduction band has a step. Due to the splitting of the spin sub-bands in the FM region, the step height is spin-dependent. Therefore, the step seen by the minority spins (blue arrows) is smaller than for the majority spins (red arrows). The transmission rate across this spin-dependent potential barrier depends on its height and therefore acts as a filter for the spins.

For comparison, we refer to Figure 5.1 that shows a sketch of a typical spin filter tunneling device using a magnetic ferrite tunneling barrier ( $\text{XFe}_2\text{O}_4$ ) sandwiched between two non-magnetic, usually metallic, electrodes (NM). The conduction band of the magnetic ferrite is spin split by  $2E_s$ , which means the tunneling barrier itself is spin dependent. The tunneling barrier is lower for the majority spins than for the minority spins. As the tunneling probability exponentially depends on the barrier height, the transmission of majority spins across the barrier is higher than that of minority spins, which leads to the spin filtering effect.

As the splitting of the spin sub-bands depends on the magnetic field  $B$ , this translates into a magnetic field dependent transmission probability through the barrier. In our case, the larger the magnetic field the smaller the potential barrier for the minority spins (and the larger for the majority spins). We have seen that the potential barrier height decreases by an amount equal to the Zeeman energy when a magnetic field is applied (Figure 5.17). This only makes sense if the current across the potential barrier consists of minority spins, otherwise one would expect an increase of the barrier height.

In the magnetic regions, the ferromagnetic coupling between spins induces a splitting of the spin sub-bands even in the absence of a magnetic field, related to the magnetic exchange interaction  $E_{ex}$  between the localized defects. This explains the negative zero-field offset of the potential barrier height observed in Figure 5.16. We identify this offset as the magnetic coupling energy  $-E_{ex} = -8$  meV.

We can therefore write the total spin-dependent potential barrier

$$V_b^{\uparrow\downarrow}(B, T) = V_b^0(T) \pm (E_{ex} + g\mu_B|B|) = V_b^0(T) \pm E_s, \quad (5.7)$$

where we call  $V_b^0$  the thermal (defined in Equation (5.1)) and

$$E_s = E_{ex} + g\mu_B|B| \quad (5.8)$$

the magnetic contributions to the potential barrier. Figure 5.19 shows the ratio  $E_s/V_b^0$  of these two contributions as a function of temperature, calculated for different ratios  $N^+/N$  of carrier densities on the two sides of the barrier. We found a ratio  $N^+/N \simeq 100$  for our wire S1, which is shown in red in Figure 5.19, once without applied magnetic field (solid line) and with a field of 7 T (dashed line). At  $T = 30$  K, the magnetic contribution  $E_s$  makes up almost half of the potential barrier. At higher temperatures, the

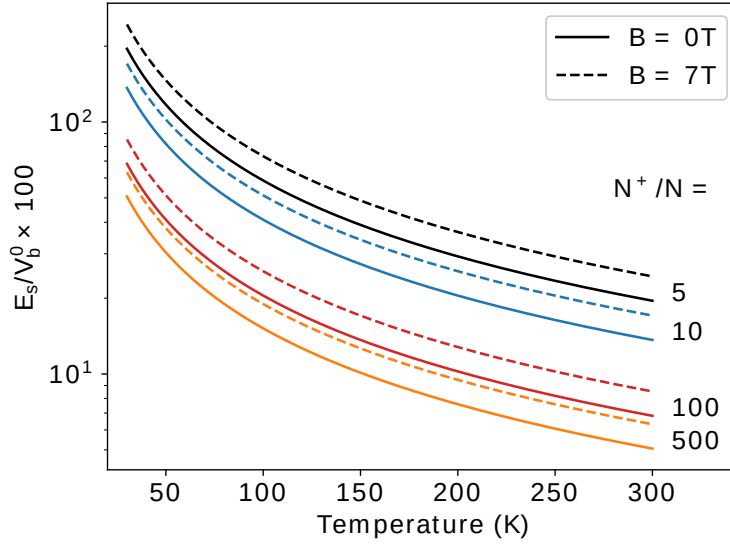


FIGURE 5.19: Ratio between the magnetic contribution ( $E_s$ ) and the thermal contribution ( $V_b^0$ ) to the potential barrier.  $E_s$  was calculated using Equation (5.8), assuming  $E_{ex} = 8$  meV and  $V_b^0$  was calculated using Equation (5.1), assuming the ratios  $N^+/N$  of carrier densities on both sides of the barrier as indicated. The solid lines show the ratios at zero magnetic field and the dashed lines show the ratios at an applied field of  $B = 7$  T.

thermal contribution becomes more important. Decreasing the ratio  $N^+/N$  of carrier concentrations, the magnetic contribution becomes overall more important, but of course the total barrier height decreases, turning the spin filter less effective, as seen in Figure 5.12 (a).

Moreover, the spin polarization in the magnetic regions, given by

$$\alpha = \frac{s_{\downarrow} - s_{\uparrow}}{s_{\downarrow} + s_{\uparrow}} = \tanh\left(\frac{e(E_{ex} + g\mu_B|B|)}{k_B T}\right), \quad (5.9)$$

where  $s_{\downarrow/\uparrow}$  denotes the majority/minority spin densities, also depends on the magnetic field, i.e. the larger the magnetic field, the larger the ratio of majority/minority spin densities and the less minority spins are available to cross the potential barrier. Figure 5.20 shows the spin polarization  $\alpha$  in the magnetic regions, assuming  $E_{ex} = 8$  meV, as a function of temperature at different applied magnetic field strengths. We note that at room temperature the zero-field spin polarization in the magnetic regions is still above 30%. The right hand side axis shows the ratio  $s_{\uparrow}/(s_{\downarrow} + s_{\uparrow}) = (1 - \alpha)/2$  of minority spins available to cross the potential barriers from the magnetic regions. The amount of minority spins clearly decreases increasing the magnetic field. To relate this change of minority spins to the magnetoresistance, we need to take a look at the difference

$$\Delta s_{\uparrow}(B) = \frac{s_{\uparrow}(B) - s_{\uparrow}(0)}{s_{\downarrow} + s_{\uparrow}} = \frac{\alpha(0) - \alpha(B)}{2} \quad (5.10)$$

between the amount of minority spins available when a magnetic field  $B$

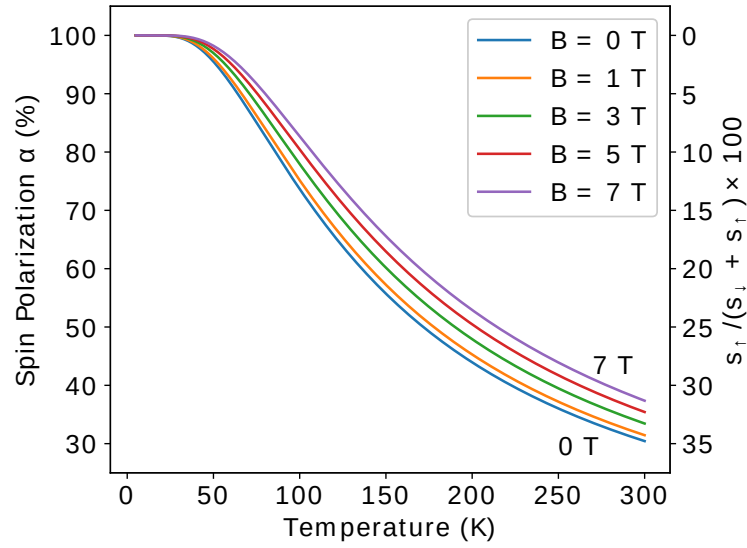


FIGURE 5.20: Spin polarization  $\alpha$  in the magnetic regions as a function of temperature at different applied magnetic field strengths  $B$ , calculated using Equation (5.9), assuming an exchange interaction energy  $E_{ex} = 8$  meV (as obtained from the I-V analysis, see Figure 5.16). The right hand side axis shows the ratio of minority spins ( $s_{\uparrow}$ ) available to cross the potential barrier from the magnetic region (calculated as  $(1 - \alpha)/2$ ).

is applied and the amount available at zero field. Figure 5.21 shows  $\Delta s_{\uparrow}$  as function of temperature for applied magnetic field strengths in the range 1 T ... 7 T. As expected, the difference  $\Delta s_{\uparrow}$  is negative, but most importantly it shows a minimum at a certain temperature that depends on  $|B|$  and  $E_{ex}$ .

These two effects together explain the observed positive magnetoresistance. We note that such minority spin filtering mechanisms have been successfully demonstrated in ferromagnetic metal/graphene heterojunctions in the past [145]. To describe semiquantitatively the transport through such a spin-dependent potential barrier, we take the simple thermionic emission model and calculate the current through the barrier, taking into account the spin polarization.

The spin dependent current density across the barrier due to thermionic emission can be expressed as

$$j_{\uparrow\downarrow} \propto \mu_{\uparrow\downarrow} T^2 \exp\left[-\frac{eV_b \pm E_s}{k_B T}\right] \times \left[\exp\left(\frac{eV_a}{k_B T}\right) - 1\right] \quad (5.11)$$

where the  $\uparrow$  symbolizes the minority spin ensemble and  $\downarrow$  the majority spins (i.e. parallel and anti-parallel to the magnetization direction).  $\mu_{\uparrow\downarrow}$  is the spin dependent electron mobility,  $V_b = k_b T \ln\left(\frac{N^+}{N}\right)$  the height of the barrier,  $N^+$  and  $N$  the carrier densities on the high and low doped side of the barrier respectively,  $V_a$  the applied voltage,  $e$  the electron charge,  $k_b$  the Boltzmann constant and  $T$  the temperature.  $E_s = g\mu_B|B| + E_{ex}$  is the spin splitting energy due to an effective exchange interaction  $E_{ex}$  and to the Zeeman interaction. Note that the barrier height  $V_b$  is of the order of 100 meV at room

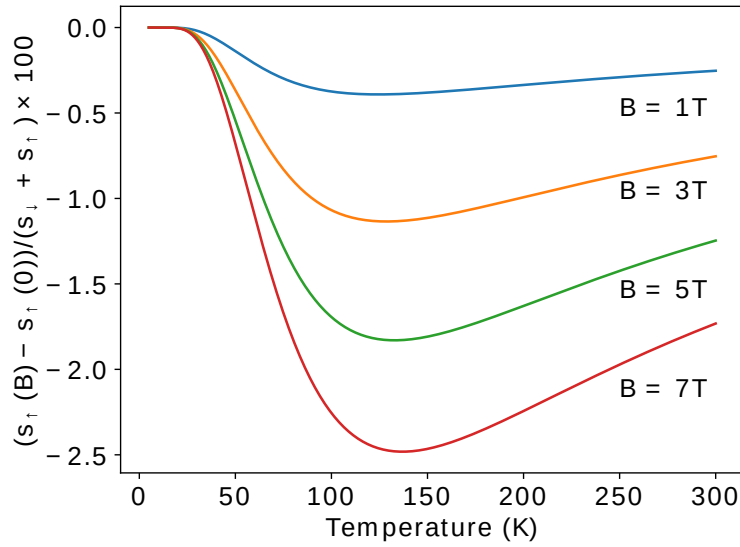


FIGURE 5.21: Change of the minority spin ratio  $(s_{\uparrow}(B) - s_{\uparrow}(0)) / (s_{\downarrow} + s_{\uparrow})$  constituting the total carriers in the magnetic regions at different applied magnetic fields, as a function of temperature. The negative ratio represents the depopulation of the minority spins due to the applied magnetic field.

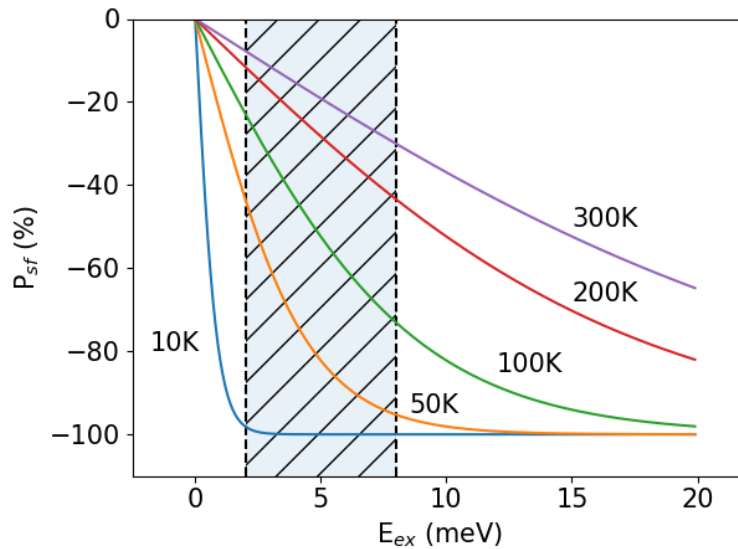


FIGURE 5.22: Spin filter efficiency  $P_{sf}$  as a function of the exchange energy  $E_{ex}$  at different temperatures in the range 10 K...300 K and zero applied magnetic field. The hatched area corresponds to the expected range of  $E_{ex}$ , with a lower bound of 2 meV estimated from the magnetoresistance data and an upper bound of 8 meV estimated from the I-V curves.



temperature assuming  $N^+/N = 100$ . The Zeeman energy is of the order of 0.1 meV/T. Therefore, the above model holds as long as  $E_{ex}$  is small compared to the barrier height. The total charge current across the barrier is then the sum of the two spin channel currents  $j = j_{\uparrow} + j_{\downarrow}$ . From this, we calculate  $MR = (R(B) - R(B = 0))/R(B = 0)$  ( $R = 1/(\partial j/\partial V_a)$  is the differential resistance):

$$MR(B, T) \propto \frac{\mu_{\downarrow}/\mu_{\uparrow}\tau_{ex}^2(\tau_B - \tau_B^2) + \tau_B - 1}{\mu_{\downarrow}/\mu_{\uparrow}\tau_{ex}^2\tau_B^2 + 1} \quad (5.12)$$

with  $\tau_B = \exp\left(\frac{g\mu_B|B|}{k_B T}\right)$  and  $\tau_{ex} = \exp\left(\frac{E_{ex}}{k_B T}\right)$ . Using this model, we calculate the temperature and magnetic field dependence of the magnetoresistance across one such potential barrier.

The dashed blue lines in Figure 5.11 (b) represent the calculated magnetoresistance from this model at different coupling strengths  $E_{ex}$ . From the comparison between the data and the simulations an exchange interaction strength of the order of 2 meV can explain the maximum of the magnetoresistance around 30 K.

This model can also explain the linear in field dependence (at low enough fields) and the linear dependence of the magnetoresistance on the number of consecutive potential barriers in series along the wire (see Figure 5.12 (b)). In the non-magnetic regions, the conduction band is degenerated and the spin polarization is lost on a lengthscale equal or larger than the spin diffusion length. In the next magnetic region, the spin-polarization is re-established due to recombination processes with the polarized defect band. Therefore, each FM/NM homojunction acts as a spin-filter and contributes equally to the magnetoresistance.

Using the thermionic emission model, we calculate the current  $j_{\uparrow\downarrow}$  of spin up/down electrons across the potential barriers and derive the spin filter efficiency

$$P_{sf} = \frac{j_{\downarrow} - j_{\uparrow}}{j_{\downarrow} + j_{\uparrow}}. \quad (5.13)$$

$P_{sf}$  depends on the spin splitting  $E_s$  of the conduction band on the magnetic side of the potential barriers, which is dominated by the exchange interaction energy  $E_{ex}$ . Figure 5.22 shows the spin filter efficiency as a function of exchange interaction energy  $E_{ex}$  at different temperatures in the range 10K...300K and at zero applied magnetic field. The hatched area corresponds to the expected range of  $E_{ex}$ , where the lower bound of 2 meV was estimated from the magnetoresistance data and the upper bound of 8 meV comes from our analysis of the I-V characteristics. At room temperature, this results in an estimated  $P_{sf} = -8\%$  in the pessimistic case and  $P_{sf} = -30\%$  in the optimistic case. The spin filter efficiency of our device is therefore at least as high as the best results obtained in spin filter tunneling devices at room temperature [121]. At 10K, our spin filter device theoretically has perfect spin filtering with  $P_{sf} = 100\%$ . Figure 5.22 clearly shows that the spin filter efficiency is very sensitive to the exchange energy  $E_{ex}$ . Therefore, increasing the exchange energy, either by tuning the defect concentration or by using different semiconducting materials in which artificial ferromagnetism can be induced by defects, would result in a major improvement of the spin filter efficiency.



## **Chapter 6**

# **Conclusions and Outlook**

Since the first prediction of room temperature artificial ferromagnetism due to magnetic ion doping in the semiconducting host material ZnO appeared twenty years ago [10], the field has evolved at a rapid pace. Examples of such artificial ferromagnets were found experimentally in a wide range of different host materials and many thousands of articles, discussing the origin of the effect were published because the magnetic order appears without the need of magnetic ions in the otherwise non-magnetic host. Still, to this day some critical questions remain open, which motivated the investigations reported in this work.

In order to understand the physics underlying this kind of materials, one first has to accept that the set of convenient rules, used to explain intrinsic ferromagnetism, such as Hund's rules or the Stoner criterion taught in undergraduate courses do not apply. Instead, one has to take into account the complex structure of the many electron system of the host material, the perturbations due to defects and the fundamental interactions leading to the ordered ground state. Although calculating this structure exactly is an intractable task, in Chapter 2 we demonstrated techniques based on density functional theory that yield good enough approximations of the charge and spin density from first principles. Combining these calculation techniques with MD simulations of collision cascades, we obtain predictions for potential artificial ferromagnetic materials that can be realized experimentally by ion irradiation.

In the development of the field, mainly two methods have emerged to introduce defects in the nominally non-magnetic host materials. In most reports, the chosen approach was to modify the growth conditions of the host material, with the advantage of obtaining homogeneously distributed defects throughout the samples. But the defect densities reachable in this way are rather limited and therefore, the magnetization reported in such materials is usually small. On the other hand, introducing defects in high quality and pure host samples using particle irradiation techniques has the potential to create much higher defect densities. But, as we showed in this work, the resulting defects are not homogeneously distributed throughout the host. Although this technique has been successfully applied to create artificial ferromagnets in different hosts, the uncertainty of the volume fraction of the resulting magnetic phase within the host sample led to inconsistent reports of the magnetization. Oftentimes, the authors used the whole sample volume to calculate the magnetization or left it out completely. Due to the small magnetization values resulting from the overestimation of the magnetic volume, the results were largely perceived as spurious effects and overlooked in the discussion of the origin of artificial ferromagnetism. One of the achievements of this work is to provide more accurate estimates of the magnetic volume, which allows to correct the reported magnetization values.

The computational results shown in Section 2.5 for the anatase  $\text{TiO}_2$  hosts irradiated with  $\text{Ar}^+$  ions at low energy (Figure 2.10) and in Section 2.6 for the high energy  $\text{Ne}^+$  irradiated 6H-SiC host (Figure 2.12) give a detailed and accurate map of the emerging artificial ferromagnetic phase throughout the parameter space and its distribution within the host sample along the irradiation direction. We showed that this information can successfully be used to explain previous experimental data (see Figure 2.11), taking into account the different kinds of defects and their creation probability due to

the ion irradiation and the amorphization of the host lattice. Furthermore, using these predictions, we provide corrections to the reported magnetization values and find that they compare to those found in typical intrinsic ferromagnetic materials.

In Chapter 3, we used these computational results to find ideal experimental parameters for tailoring the artificial ferromagnet based on  $\text{TiO}_2$  thin film hosts. Tuning the irradiation parameters, in Chapter 4, we show that the ferromagnetic phase emerges in an ultrathin region of the order of a few host lattice layers down to the monolayer limit. The magnetic phase exhibits a strong uniaxial anisotropy with an easy axis depending on the thickness and proximity to the sample surface, switching from an in-plane to out-of-plane anisotropy varying the irradiation parameters. We present DFT electronic structure calculations that explain very well our experimental observations.

The results presented in Chapters 3 and 4 show the versatility of these artificial ferromagnets: Their magnetostatic properties can be tuned and tailored for applications and the ability to induce a ferromagnetic order in a well defined region of a nominally non-magnetic host allows the integration of magnetic applications into existing electronic systems. But the real power of these artificial ferromagnetic materials lies in the combination of engineered magnetic properties with the intrinsic properties of the host material. As we show in Chapter 5, using established semiconductor technology, such as doping with Li and H and lithographic processes allowed us to simultaneously engineer the band structure of the ZnO host and induce a ferromagnetic phase in well defined regions along the microwire samples. We applied the combined effect of the magnetic and electronic conduction properties to control the spin transport dynamics and create an efficient minority spin filter device, which generates highly spin polarized currents even at room temperature. These material engineering techniques could be used to create building blocks for advanced spintronic applications.

Recently, some of the defects involved in the magnetic percolation process leading to the emerging ferromagnetic phase in certain host materials, notably the di-vacancy in SiC or the famous NV center in diamond, have attracted much interest on their own due to their potential use as a building block for future quantum information processing applications. These so-called defect spin qubits show very favorable properties such as room temperature operation conditions, optical readout and manipulation schemes for their spin state and tunable coupling to their environment. Although this field is just starting to develop and to this date, we are still far away from the realization of a functional quantum processing application, the insight gained so far looks promising. In this context, the role of the magnetic coupling between these localized defect spin states, that leads to a macroscopically ordered phase at the percolation transition, has yet to be fully understood and will be important for the future development of this emerging field.



# Bibliography

- <sup>1</sup>A. Hirohata, K. Yamada, Y. Nakatani, I.-L. Prejbeanu, B. Dieny, P. Pirro, and B. Hillebrands, "Review on spintronics: Principles and device applications", *Journal of Magnetism and Magnetic Materials* **509**, 166711 (2020).
- <sup>2</sup>C. Chappert, A. Fert, and F. N. Van Dau, "The emergence of spin electronics in data storage", *Nature Materials* **6**, 813–823 (2007).
- <sup>3</sup>N. Sharma, J. P. Bird, C. Binek, P. A. Dowben, D. Nikonov, and A. Marshall, "Evolving magneto-electric device technologies", *Semiconductor Science and Technology* **35**, 073001 (2020).
- <sup>4</sup>S. Bhatti, R. Sbiaa, A. Hirohata, H. Ohno, S. Fukami, and S. N. Piramanayagam, "Spintronics based random access memory: a review", *Materials Today* **20**, 530 (2017).
- <sup>5</sup>C. Song, B. Cui, F. Li, X. Zhou, and F. Pan, "Recent progress in voltage control of magnetism: Materials, mechanisms, and performance", *Progress in Materials Science* **87**, 33 (2017).
- <sup>6</sup>J. S. Meena, S. M. Sze, U. Chand, and T.-Y. Tseng, "Overview of emerging nonvolatile memory technologies", *Nanoscale Research Letters* **9**, 526 (2014).
- <sup>7</sup>S. Ning, P. Zhan, Q. Xie, W. Wang, and Z. Zhang, "Defects-Driven Ferromagnetism in Undoped Dilute Magnetic Oxides: A Review", *Journal of Materials Science & Technology* **31**, 969–978 (2015).
- <sup>8</sup>P. D. Esquinazi, W. Hergert, M. Stiller, L. Botsch, H. Ohldag, D. Spemann, M. Hoffmann, W. A. Adeagbo, A. Chassé, S. K. Nayak, and H. Ben Hamed, "Defect induced magnetism in non-magnetic Oxides: Basic principles, experimental evidence and possible devices", *Physica Status Solidi B* **257**, 1900623 (2020).
- <sup>9</sup>M.-C. Wang, C.-C. Huang, C.-H. Cheung, C.-Y. Chen, S. G. Tan, T.-W. Huang, Y. Zhao, Y. Zhao, G. Wu, Y.-P. Feng, H.-C. Wu, and C.-R. Chang, "Prospects and Opportunities of 2D van der Waals Magnetic Systems", *Annalen der Physik* **532**, 1900452 (2020).
- <sup>10</sup>T. Dietl, H. Ohno, F. Matsukura, J. Cibert, and D. Ferrand, "Zener Model Description of Ferromagnetism in Zinc-Blende Magnetic Semiconductors", *Science* **287**, 1019–1022 (2000).
- <sup>11</sup>A. Sundaresan, R. Bhargavi, N. Rangarajan, U. Siddesh, and C. N. R. Rao, "Ferromagnetism as a universal feature of nanoparticles of the otherwise nonmagnetic oxides", *Physical Review B* **74**, 161306 (2006).
- <sup>12</sup>M. Khalid, M. Ziese, A. Setzer, P. D. Esquinazi, M. Lorenz, H. Hochmuth, M. Grundmann, D. Spemann, T. Butz, G. Brauer, W. Anwand, G. Fischer, W. A. Adeagbo, W. Hergert, and A. Ernst, "Defect-induced magnetic order in pure ZnO films", *Physical Review B* **80**, 035331 (2009).

- <sup>13</sup>N. H. Hong, J. Sakai, and V. Brize, "Observation of ferromagnetism at room temperature in ZnO thin films", *Journal of Physics - Condensed Matter* **19**, 036219 (2007).
- <sup>14</sup>N. H. Hong, N. Poirot, and J. Sakai, "Ferromagnetism observed in pristine SnO<sub>2</sub> thin films", *Physical Review B* **77**, 033205 (2008).
- <sup>15</sup>S. Zhou, "Defect-induced ferromagnetism in semiconductors: A controllable approach by particle irradiation", *Nuclear Instruments and Methods in Physics Research Section B: Beam Interactions with Materials and Atoms* **326**, 17<sup>th</sup> International Conference on Radiation Effects in Insulators (REI), 55–60 (2014).
- <sup>16</sup>K. Ackland and J. Coey, "Room temperature magnetism in CeO<sub>2</sub>– A review", *Physics Reports* **746**, 1–39 (2018).
- <sup>17</sup>J. M. D. Coey, "Magnetism in d<sup>0</sup> oxides", *Nature Materials* **18**, 652–656 (2019).
- <sup>18</sup>S. Akbar, S. Hasanain, M. Abbas, S. Ozcan, B. Ali, and S. I. Shah, "Defect induced ferromagnetism in carbon-doped ZnO thin films", *Solid State Communications* **151**, 17–20 (2011).
- <sup>19</sup>N. Ali, A. R. Vijaya, Z. A. Khan, K. Tarafder, A. Kumar, M. K. Wadhwa, B. Singh, and S. Ghosh, "Ferromagnetism from non-magnetic ions: Ag-doped ZnO", *Scientific Reports* **9**, 20039 (2019).
- <sup>20</sup>D. B. Buchholz, R. P. H. Chang, J.-Y. Song, and J. B. Ketterson, "Room-temperature ferromagnetism in Cu-doped ZnO thin films", *Applied Physics Letters* **87**, 082504 (2005).
- <sup>21</sup>S. Chawla, K. Jayanthi, and R. K. Kotnala, "Room-temperature ferromagnetism in Li-doped p-type luminescent ZnO nanorods", *Physical Review B* **79**, 125204 (2009).
- <sup>22</sup>B. Choudhury, A. Choudhury, and D. Borah, "Interplay of dopants and defects in making Cu doped TiO<sub>2</sub> nanoparticle a ferromagnetic semiconductor", *Journal of Alloys and Compounds* **646**, 692 (2015).
- <sup>23</sup>S. Duhalde, M. F. Vignolo, F. Golmar, C. Chilotte, C. E. R. Torres, L. A. Errico, A. F. Cabrera, M. Renteria, F. H. Sánchez, and M. Weissmann, "Appearance of room-temperature ferromagnetism in Cu-doped TiO<sub>2</sub> films", *Physical Review B* **72**, 161313 (2005).
- <sup>24</sup>X. G. Xu, H. L. Yang, Y. Wu, D. L. Zhang, S. Z. Wu, J. Miao, Y. Jiang, X. B. Qin, X. Z. Cao, and B. Y. Wang, "Intrinsic room temperature ferromagnetism in boron-doped ZnO", *Applied Physics Letters* **97**, 232502 (2010).
- <sup>25</sup>S. Ghosh and P. M. G. Nambissan, "Evidence of oxygen and Ti vacancy induced ferromagnetism in post-annealed undoped anatase TiO<sub>2</sub> nanocrystals: A spectroscopic analysis", *Journal of Solid State Chemistry* **275**, 174 (2019).
- <sup>26</sup>M. Khalid, P. D. Esquinazi, D. Spemann, W. Anwand, and G. Brauer, "Hydrogen-mediated ferromagnetism in ZnO single crystals", *New Journal of Physics* **13**, 063017 (2011).
- <sup>27</sup>M. Stiller, J. Barzola-Quiquia, P. D. Esquinazi, D. Spemann, J. Meijer, M. Lorenz, and M. Grundmann, "Strong out-of-plane magnetic anisotropy in ion irradiated anatase TiO<sub>2</sub> thin films", *AIP Advances* **6**, 125009 (2016).



- <sup>28</sup>K. Shimizu, S. Kosugi, Y. Tahara, K. Yasunaga, Y. Kaneta, N. Ishikawa, F. Hori, T. Matsui, and A. Iwase, "Change in magnetic properties induced by swift heavy ion irradiation in CeO<sub>2</sub>", *Nuclear Instruments and Methods in Physics Research Section B: Beam Interactions with Materials and Atoms* **286**, Proceedings of the Sixteenth International Conference on Radiation Effects in Insulators (REI), 291–294 (2012).
- <sup>29</sup>L. Li, S. Prucnal, S. D. Yao, K. Potzger, W. Anwand, A. Wagner, and S. Zhou, "Rise and fall of defect induced ferromagnetism in SiC single crystals", *Applied Physics Letters* **98**, 222508 (2011).
- <sup>30</sup>Y. Liu, G. Wang, S. Wang, J. Yang, L. Chen, X. Qin, B. Song, B. Wang, and X. Chen, "Defect-Induced Magnetism in Neutron Irradiated 6H-SiC Single Crystals", *Physical Review Letters* **106**, 087205 (2011).
- <sup>31</sup>H. Liu, G. Li, E. Dejun, N. Xu, Q. Lin, X. Gao, C. Lan, J. Chen, C. Wang, X. Zhan, and K. Zhang, "Room temperature ferromagnetism in D-D neutron irradiated rutile TiO<sub>2</sub> single crystals", *RSC Advances* **10**, 18687 (2020).
- <sup>32</sup>I. Lorite, B. Straube, H. Ohldag, P. Kumar, M. Villafuerte, P. D. Esquinazi, C. E. Rodríguez Torres, S. Perez de Heluani, V. N. Antonov, L. V. Bekenov, A. Ernst, M. Hoffmann, S. K. Nayak, W. A. Adeagbo, G. Fischer, and W. Hergert, "Advances in methods to obtain and characterise room temperature magnetic ZnO", *Applied Physics Letters* **106**, 082406 (2015).
- <sup>33</sup>B. Qi, S. Ólafsson, and H. Gíslason, "Vacancy defect-induced d<sup>0</sup> ferromagnetism in undoped ZnO nanostructures: Controversial origin and challenges", *Progress in Materials Science* **90**, 45–74 (2017).
- <sup>34</sup>M. Stiller, A. T. N'Diaye, H. Ohldag, J. Barzola-Quiquia, P. D. Esquinazi, T. Amelal, C. Bundesmann, D. Spemann, M. Trautmann, A. Chassé, H. B. Hamed, W. A. Adeagbo, and W. Hergert, "Titanium 3d ferromagnetism with perpendicular anisotropy in defective anatase", *Physical Review B* **101**, 014412 (2020).
- <sup>35</sup>D.-S. Park, A. D. Rata, I. V. Maznichenko, S. Ostanin, Y. L. Gan, S. Agrestini, G. J. Rees, M. Walker, J. Li, J. Herrero-Martin, G. Singh, Z. Luo, A. Bhatnagar, Y. Z. Chen, V. Tileli, P. Muralt, A. Kalaboukhov, I. Mertig, K. Dörr, A. Ernst, and N. Pryds, "The emergence of magnetic ordering at complex oxide interfaces tuned by defects", *Nature Communications* **11**, 3650 (2020).
- <sup>36</sup>S. A. Wolf, D. D. Awschalom, R. A. Buhrman, J. M. Daughton, S. von Molnár, M. L. Roukes, A. Y. Chtchelkanova, and D. M. Treger, "Spintronics: A Spin-Based Electronics Vision for the Future", *Science* **294**, 1488–1495 (2001).
- <sup>37</sup>F. Pan, C. Song, X. Liu, Y. Yang, and F. Zeng, "Ferromagnetism and possible application in spintronics of transition-metal-doped ZnO films", *Materials Science and Engineering: R: Reports* **62**, 1–35 (2008).
- <sup>38</sup>W. Heitler and F. London, "Wechselwirkung neutraler Atome und homöopolare Bindung nach der Quantenmechanik", *Zeitschrift für Physik* **44**, 455–472 (1927).
- <sup>39</sup>Y. Sugiura, "Über die Eigenschaften des Wasserstoffmoleküls im Grundzustande", *Zeitschrift für Physik* **45**, 484–492 (1927).

- <sup>40</sup>J. F. Ziegler, M. D. Ziegler, and J. P. Biersack, "SRIM - The stopping and range of ions in matter (2010)", *Nuclear Instruments & Methods in Physics Research Section B - Beam Interactions with Materials and Atoms* **268**, 1818 (2010).
- <sup>41</sup>K. Nordlund, S. J. Zinkle, A. E. Sand, F. Granberg, R. S. Averback, R. E. Stoller, T. Suzudo, L. Malerba, F. Banhart, W. J. Weber, F. Willaime, S. L. Dudarev, and D. Simeone, "Primary radiation damage: A review of current understanding and models", *Journal of Nuclear Materials* **512**, 450–479 (2018).
- <sup>42</sup>A. Liechtenstein, M. Katsnelson, V. Antropov, and V. Gubanov, "Local spin density functional approach to the theory of exchange interactions in ferromagnetic metals and alloys", *Journal of Magnetism and Magnetic Materials* **67**, 65–74 (1987).
- <sup>43</sup>M. Robinson, N. A. Marks, K. R. Whittle, and G. R. Lumpkin, "Systematic calculation of threshold displacement energies: Case study in rutile", *Physical Review B* **85**, 104105 (2012).
- <sup>44</sup>M. Robinson, N. Marks, and G. Lumpkin, "Structural dependence of threshold displacement energies in rutile, anatase and brookite TiO<sub>2</sub>", *Materials Chemistry and Physics* **147**, 311–318 (2014).
- <sup>45</sup>Q. K. Li, B. Wang, C. H. Woo, H. Wang, Z. Y. Zhu, and R. Wang, "Origin of unexpected magnetism in Cu-doped TiO<sub>2</sub>", *Europhysics Letters (EPL)* **81**, 17004 (2007).
- <sup>46</sup>M. Wang, M. Feng, and X. Zuo, "First principles study of the electronic structure and magnetism of oxygen-deficient anatase TiO<sub>2</sub> (001) surface", *Applied Surface Science* **292**, 475–479 (2014).
- <sup>47</sup>E. Finazzi, C. Di Valentin, and G. Pacchioni, "Nature of Ti Interstitials in Reduced Bulk Anatase and Rutile TiO<sub>2</sub>", *The Journal of Physical Chemistry C* **113**, 3382–3385 (2009).
- <sup>48</sup>FLEUR code, [www.flapw.de](http://www.flapw.de).
- <sup>49</sup>J. Coey, "Dilute magnetic oxides", *Current Opinion in Solid State and Materials Science* **10**, 83–92 (2006).
- <sup>50</sup>J. M. D. Coey, M. Venkatesan, and P. Stamenov, "Surface magnetism of strontium titanate", *Journal of Physics: Condensed Matter* **28**, 485001 (2016).
- <sup>51</sup>J. M. D. Coey, M. Venkatesan, and H. Xu, "Introduction to Magnetic Oxides", in *Functional Metal Oxides* (John Wiley & Sons, Ltd, 2013) Chap. 1, pp. 1–49.
- <sup>52</sup>Y. Wang, Y. Liu, G. Wang, W. Anwand, C. A. Jenkins, E. Arenholz, F. Munnik, O. D. Gordan, G. Salvan, D. R. T. Zahn, X. Chen, S. Gemming, M. Helm, and S. Zhou, "Carbon p Electron Ferromagnetism in Silicon Carbide", *Scientific Reports* **5**, 8999 (2015).
- <sup>53</sup>W. Li, L. Wang, L. Bian, F. Dong, M. Song, J. Shao, S. Jiang, and H. Guo, "Threshold displacement energies and displacement cascades in 4H-SiC: Molecular dynamic simulations", *AIP Advances* **9**, 055007 (2019).
- <sup>54</sup>NIST Interatomic Potentials Repository.

- <sup>55</sup>E. B. Tadmor, R. S. Elliott, J. P. Sethna, R. E. Miller, and C. A. Becker, "The Potential of Atomistic Simulations and the Knowledgebase of Interatomic Models", *JOM* **63**, 17 (2011).
- <sup>56</sup>*LXcat cross section database, www.lxcat.net.*
- <sup>57</sup>*Magnetic Property Measurement System, Hardware Reference Manual, Quantum Design* (1996).
- <sup>58</sup>C. Bundesmann, T. Lautenschläger, D. Spemann, A. Finzel, E. Thelander, M. Mensing, and F. Frost, "Systematic investigation of the properties of TiO<sub>2</sub> films grown by reactive ion beam sputter deposition", *Applied Surface Science* **421**, 7<sup>th</sup> International Conference on Spectroscopic Ellipsometry, 331–340 (2017).
- <sup>59</sup>K.-H. Hellwege and A. M. Hellwege, *Magnetic and Other Properties of Oxides and Related Compounds - Part A*, 1st ed., Landolt-Börnstein - Group III Condensed Matter 4a : Condensed Matter (Springer-Verlag Berlin Heidelberg, 1970).
- <sup>60</sup>N. D. Mermin and H. Wagner, "Absence of Ferromagnetism or Antiferromagnetism in One- or Two-Dimensional Isotropic Heisenberg Models", *Physical Review Letters* **17**, 1133–1136 (1966).
- <sup>61</sup>X. L. Matthias Wuttig, *Ultrathin Metal Films: Magnetic and Structural Properties*, 1st ed., Springer Tracts in Modern Physics 206 (Springer-Verlag Berlin Heidelberg, 2004).
- <sup>62</sup>C. A. F. Vaz, J. A. C. Bland, and G. Lauhoff, "Magnetism in ultrathin film structures", *Reports on Progress in Physics* **71**, 056501 (2008).
- <sup>63</sup>J. Barzola-Quiquia, P. D. Esquinazi, M. Rothmel, D. Spemann, T. Butz, and N. Garcia, "Experimental evidence for two-dimensional magnetic order in proton bombarded graphite", *Physical Review B* **76**, 161403 (R) (2007).
- <sup>64</sup>C. Gong and X. Zhang, "Two-dimensional magnetic crystals and emergent heterostructure devices", *Science* **363**, 706 (2019).
- <sup>65</sup>Z. Q. Qiu, J. Pearson, and S. D. Bader, "Magnetic phase transition of ultrathin Fe films on Ag(111)", *Physical Review Letters* **67**, 1646–1649 (1991).
- <sup>66</sup>Y. Li and K. Baberschke, "Dimensional crossover in ultrathin Ni(111) films on W(110)", *Physical Review Letters* **68**, 1208–1211 (1992).
- <sup>67</sup>A. Freeman and R.-Q. Wu, "Electronic structure theory of surface, interface and thin-film magnetism", *Journal of Magnetism and Magnetic Materials* **100**, 497–514 (1991).
- <sup>68</sup>J. Xia, W. Siemons, G. Koster, M. R. Beasley, and A. Kapitulnik, "Critical thickness for itinerant ferromagnetism in ultrathin films of SrRuO<sub>3</sub>", *Physical Review B* **79**, 140407 (2009).
- <sup>69</sup>D. A. Rehn, J. M. Wills, T. E. Battelle, and A. E. Mattsson, "Dirac's equation and its implications for density functional theory based calculations of materials containing heavy elements", *Physical Review B* **101**, 085114 (2020).
- <sup>70</sup>M. T. Johnson, P. J. H. Bloemen, F. J. A. den Broeder, and J. J. de Vries, "Magnetic anisotropy in metallic multilayers", *Reports on Progress in Physics* **59**, 1409–1458 (1996).

- <sup>71</sup>H. Krakauer, M. Posternak, and A. J. Freeman, "Linearized augmented plane-wave method for the electronic band structure of thin films", *Physical Review B* **19**, 1706–1719 (1979).
- <sup>72</sup>E. Araujo-Lopez, L. A. Varilla, N. Seriani, and J. A. Montoya, "TiO<sub>2</sub> anatase's bulk and (001) surface, structural and electronic properties: A DFT study on the importance of Hubbard and van der Waals contributions", *Surface Science* **653**, 187–196 (2016).
- <sup>73</sup>K. Ueda, H. Tabata, and T. Kawai, "Magnetic and electric properties of transition-metal-doped ZnO films", *Applied Physics Letters* **79**, 988–990 (2001).
- <sup>74</sup>Z. Jin, T. Fukumura, M. Kawasaki, K. Ando, H. Saito, T. Sekiguchi, Y. Z. Yoo, M. Murakami, Y. Matsumoto, T. Hasegawa, and H. Koinuma, "High throughput fabrication of transition-metal-doped epitaxial ZnO thin films: A series of oxide-diluted magnetic semiconductors and their properties", *Applied Physics Letters* **78**, 3824–3826 (2001).
- <sup>75</sup>T. Fukumura, Z. Jin, M. Kawasaki, T. Shono, T. Hasegawa, S. Koshihara, and H. Koinuma, "Magnetic properties of Mn-doped ZnO", *Applied Physics Letters* **78**, 958–960 (2001).
- <sup>76</sup>S. W. Jung, S.-J. An, G.-C. Yi, C. U. Jung, S.-I. Lee, and S. Cho, "Ferromagnetic properties of Zn<sub>1-x</sub>Mn<sub>x</sub>O epitaxial thin films", *Applied Physics Letters* **80**, 4561–4563 (2002).
- <sup>77</sup>H.-J. Lee, S.-Y. Jeong, C. R. Cho, and C. H. Park, "Study of diluted magnetic semiconductor: Co-doped ZnO", *Applied Physics Letters* **81**, 4020–4022 (2002).
- <sup>78</sup>D. P. Norton, S. J. Pearton, A. F. Hebard, N. Theodoropoulou, L. A. Boatner, and R. G. Wilson, "Ferromagnetism in Mn-implanted ZnO:Sn single crystals", *Applied Physics Letters* **82**, 239–241 (2003).
- <sup>79</sup>S. J. Pearton, C. R. Abernathy, M. E. Overberg, G. T. Thaler, D. P. Norton, N. Theodoropoulou, A. F. Hebard, Y. D. Park, F. Ren, J. Kim, and L. A. Boatner, "Wide band gap ferromagnetic semiconductors and oxides", *Journal of Applied Physics* **93**, 1–13 (2003).
- <sup>80</sup>P. Sharma, A. Gupta, K. Rao, F. Owens, R. Sharma, R. Ahuja, J. Guillen, B. Johansson, and G. Gehring, "Ferromagnetism above room temperature in bulk and transparent thin films of Mn-doped ZnO", *Nature Materials* **2**, 673–677 (2003).
- <sup>81</sup>S. Ramachandran, A. Tiwari, and J. Narayan, "Zn<sub>0.9</sub>Co<sub>0.1</sub>O-based diluted magnetic semiconducting thin films", *Applied Physics Letters* **84**, 5255–5257 (2004).
- <sup>82</sup>C. Liu, F. Yun, and H. Morkoc, "Ferromagnetism of ZnO and GaN: A review", *Journal of Materials Science - Materials in Electronics* **16**, 555–597 (2005).
- <sup>83</sup>D. Karmakar, S. K. Mandal, R. M. Kadam, P. L. Paulose, A. K. Rajarajan, T. K. Nath, A. K. Das, I. Dasgupta, and G. P. Das, "Ferromagnetism in Fe-doped ZnO nanocrystals: Experiment and theory", *Physical Review B* **75**, 144404 (2007).
- <sup>84</sup>T. Dietl and H. Ohno, "Dilute ferromagnetic semiconductors: Physics and spintronic structures", *Reviews of Modern Physics* **86**, 187–251 (2014).

- <sup>85</sup>L. T. Tseng, A. Suter, Y. R. Wang, F. X. Xiang, P. Bian, X. Ding, A. Tseng, H. L. Hu, H. M. Fan, R. K. Zheng, X. L. Wang, Z. Salman, T. Prokscha, K. Suzuki, R. Liu, S. Li, E. Morenzoni, and J. B. Yi, "Intrinsic and spatially nonuniform ferromagnetism in Co-doped ZnO films", *Physical Review B* **96**, 104423 (2017).
- <sup>86</sup>J. H. Park, M. G. Kim, H. M. Jang, S. Ryu, and Y. M. Kim, "Co-metal clustering as the origin of ferromagnetism in Co-doped ZnO thin films", *Applied Physics Letters* **84**, 1338–1340 (2004).
- <sup>87</sup>G. Lawes, A. S. Risbud, A. P. Ramirez, and R. Seshadri, "Absence of ferromagnetism in Co and Mn substituted polycrystalline ZnO", *Physical Review B* **71**, 045201 (2005).
- <sup>88</sup>C. N. R. Rao and F. L. Deepak, "Absence of ferromagnetism in Mn- and Co-doped ZnO", *Journal of Materials Chemistry* **15**, 573–578 (2005).
- <sup>89</sup>J. B. Yi, C. C. Lim, G. Z. Xing, H. M. Fan, L. H. Van, S. L. Huang, K. S. Yang, X. L. Huang, X. B. Qin, B. Y. Wang, T. Wu, L. Wang, H. T. Zhang, X. Y. Gao, T. Liu, A. T. S. Wee, Y. P. Feng, and J. Ding, "Ferromagnetism in Dilute Magnetic Semiconductors through Defect Engineering: Li-Doped ZnO", *Physical Review Letters* **104**, 137201 (2010).
- <sup>90</sup>S. Ghosh, G. G. Khan, A. Ghosh, S. Varma, and K. Mandal, "Zinc vacancy-induced high-TC ferromagnetism and photoluminescence in group-1 alkali-metal substituted p-type ZnO thin films", *CrystEngComm* **15**, 7748–7755 (2013).
- <sup>91</sup>I. S. Elfimov, A. Rusydi, S. I. Csiszar, Z. Hu, H. H. Hsieh, H.-J. Lin, C. T. Chen, R. Liang, and G. A. Sawatzky, "Magnetizing Oxides by Substituting Nitrogen for Oxygen", *Physical Review Letters* **98**, 137202 (2007).
- <sup>92</sup>C.-F. Yu, T.-J. Lin, S.-J. Sun, and H. Chou, "Origin of ferromagnetism in nitrogen embedded ZnO:N thin films", *Journal of Physics D: Applied Physics* **40**, 6497–6500 (2007).
- <sup>93</sup>K. Y. Wu, Q. Q. Fang, W. N. Wang, C. Zhou, W. J. Huang, J. G. Li, Q. R. Lv, Y. M. Liu, Q. P. Zhang, and H. M. Zhang, "Influence of nitrogen on the defects and magnetism of ZnO:N thin films", *Journal of Applied Physics* **108**, 063530 (2010).
- <sup>94</sup>L.-H. Ye, A. J. Freeman, and B. Delley, "Half-metallic ferromagnetism in Cu-doped ZnO: Density functional calculations", *Physical Review B* **73**, 033203 (2006).
- <sup>95</sup>S. Ghosh, G. G. Khan, B. Das, and K. Mandal, "Vacancy-induced intrinsic d0 ferromagnetism and photoluminescence in potassium doped ZnO nanowires", *Journal of Applied Physics* **109**, 123927 (2011).
- <sup>96</sup>D. Gao, J. Zhang, G. Yang, J. Zhang, Z. Shi, J. Qi, Z. Zhang, and D. Xue, "Ferromagnetism in ZnO Nanoparticles Induced by Doping of a Non-magnetic Element: Al", *The Journal of Physical Chemistry C* **114**, 13477–13481 (2010).
- <sup>97</sup>H. Pan, J. B. Yi, L. Shen, R. Q. Wu, J. H. Yang, J. Y. Lin, Y. P. Feng, J. Ding, L. H. Van, and J. H. Yin, "Room-Temperature Ferromagnetism in Carbon-Doped ZnO", *Physical Review Letters* **99**, 127201 (2007).



- <sup>98</sup>N. H. Hong, J. Sakai, N. Poirot, and V. Brizé, "Room-temperature ferromagnetism observed in undoped semiconducting and insulating oxide thin films", *Physical Review B* **73**, 132404 (2006).
- <sup>99</sup>Q. Wang, Q. Sun, G. Chen, Y. Kawazoe, and P. Jena, "Vacancy-induced magnetism in ZnO thin films and nanowires", *Physical Review B* **77**, 205411 (2008).
- <sup>100</sup>Q. Xu, H. Schmidt, S. Zhou, K. Potzger, M. Helm, H. Hochmuth, M. Lorenz, A. Setzer, P. D. Esquinazi, C. Meinecke, and M. Grundmann, "Room temperature ferromagnetism in ZnO films due to defects", *Applied Physics Letters* **92**, 082508 (2008).
- <sup>101</sup>G. Z. Xing, Y. H. Lu, Y. F. Tian, J. B. Yi, C. C. Lim, Y. F. Li, G. P. Li, D. D. Wang, B. Yao, J. Ding, Y. P. Feng, and T. Wu, "Defect-induced magnetism in undoped wide band gap oxides: Zinc vacancies in ZnO as an example", *AIP Advances* **1**, 022152 (2011).
- <sup>102</sup>D. Kim, J.-H. Yang, and J. Hong, "Ferromagnetism induced by Zn vacancy defect and lattice distortion in ZnO", *Journal of Applied Physics* **106**, 013908 (2009).
- <sup>103</sup>A. L. Schoenhalz, J. T. Arantes, A. Fazzio, and G. M. Dalpian, "Surface magnetization in non-doped ZnO nanostructures", *Applied Physics Letters* **94**, 162503 (2009).
- <sup>104</sup>S. Kumar, Y. Kim, B. Koo, S. Gautam, K. Chae, R. Kumar, and C. Lee, "Room temperature ferromagnetism in chemically synthesized ZnO rods", *Materials Letters* **63**, 194–196 (2009).
- <sup>105</sup>M. Kapilashrami, J. Xu, V. Ström, K. V. Rao, and L. Belova, "Transition from ferromagnetism to diamagnetism in undoped ZnO thin films", *Applied Physics Letters* **95**, 033104 (2009).
- <sup>106</sup>X. J. Wang, L. S. Vlasenko, S. J. Pearton, W. M. Chen, and I. A. Buyanova, "Oxygen and zinc vacancies in as-grown ZnO single crystals", *Journal of Physics D: Applied Physics* **42**, 175411 (2009).
- <sup>107</sup>D. Wang, Z. Q. Chen, D. D. Wang, N. Qi, J. Gong, C. Y. Cao, and Z. Tang, "Positron annihilation study of the interfacial defects in ZnO nanocrystals: Correlation with ferromagnetism", *Journal of Applied Physics* **107**, 023524 (2010).
- <sup>108</sup>S. Mal, S. Nori, J. Narayan, J. Prater, and D. Avasthi, "Ion-irradiation-induced ferromagnetism in undoped ZnO thin films", *Acta Materialia* **61**, 2763–2768 (2013).
- <sup>109</sup>J. S. Moodera, T. S. Santos, and T. Nagahama, "The phenomena of spin-filter tunnelling", *Journal of Physics: Condensed Matter* **19**, 165202 (2007).
- <sup>110</sup>J.-B. Moussy, "From epitaxial growth of ferrite thin films to spin-polarized tunnelling", *Journal of Physics D - Applied Physics* **46**, 10.1088/0022-3727/46/14/143001 (2013).
- <sup>111</sup>N. Müller, W. Eckstein, W. Heiland, and W. Zinn, "Electron Spin Polarization in Field Emission from EuS-Coated Tungsten Tips", *Physical Review Letters* **29**, 1651–1654 (1972).

- <sup>112</sup>E. Kisker, G. Baum, A. H. Mahan, W. Raith, and K. Schröder, "Conduction-Band Tunneling and Electron-Spin Polarization in Field Emission from Magnetically Ordered Europium Sulfide on Tungsten", *Physical Review Letters* **36**, 982–985 (1976).
- <sup>113</sup>G. Baum, E. Kisker, A. H. Mahan, W. Raith, and B. Reihl, "Field emission of monoenergetic spin-polarized electrons", *Applied physics* **14**, 149–153 (1977).
- <sup>114</sup>J. S. Moodera, X. Hao, G. A. Gibson, and R. Meservey, "Electron-Spin Polarization in Tunnel Junctions in Zero Applied Field with Ferromagnetic EuS Barriers", *Physical Review Letters* **61**, 637–640 (1988).
- <sup>115</sup>J. S. Moodera, R. Meservey, and X. Hao, "Variation of the electron-spin polarization in EuSe tunnel junctions from zero to near 100% in a magnetic field", *Physical Review Letters* **70**, 853–856 (1993).
- <sup>116</sup>P. LeClair, J. K. Ha, H. J. M. Swagten, J. T. Kohlhepp, C. H. van de Vin, and W. J. M. de Jonge, "Large magnetoresistance using hybrid spin filter devices", *Applied Physics Letters* **80**, 625–627 (2002).
- <sup>117</sup>M. Gajek, M. Bibes, A. Barthélémy, K. Bouzehouane, S. Fusil, M. Varela, J. Fontcuberta, and A. Fert, "Spin filtering through ferromagnetic BiMnO<sub>3</sub> tunnel barriers", *Physical Review B* **72**, 020406 (2005).
- <sup>118</sup>U. Lüders, M. Bibes, K. Bouzehouane, E. Jacquet, J.-P. Contour, S. Fusil, J.-F. Bobo, J. Fontcuberta, A. Barthélémy, and A. Fert, "Spin filtering through ferrimagnetic NiFe<sub>2</sub>O<sub>4</sub> tunnel barriers", *Applied Physics Letters* **88**, 082505 (2006).
- <sup>119</sup>A. V. Ramos, M.-J. Guittet, J.-B. Moussy, R. Mattana, C. Deranlot, F. Petroff, and C. Gatel, "Room temperature spin filtering in epitaxial cobalt-ferrite tunnel barriers", *Applied Physics Letters* **91**, 122107 (2007).
- <sup>120</sup>Y. K. Takahashi, S. Kasai, T. Furubayashi, S. Mitani, K. Inomata, and K. Hono, "High spin-filter efficiency in a Co ferrite fabricated by a thermal oxidation", *Applied Physics Letters* **96**, 072512 (2010).
- <sup>121</sup>S. Matzen, J.-B. Moussy, R. Mattana, K. Bouzehouane, C. Deranlot, and F. Petroff, "Nanomagnetism of cobalt ferrite-based spin filters probed by spin-polarized tunneling", *Applied Physics Letters* **101**, 042409 (2012).
- <sup>122</sup>S. Matzen, J.-B. Moussy, G. X. Miao, and J. S. Moodera, "Direct evidence of spin filtering across MnFe<sub>2</sub>O<sub>4</sub> tunnel barrier by Meservey-Tedrow experiment", *Physical Review B* **87**, 184422 (2013).
- <sup>123</sup>P. Li, C. Xia, Z. Zhu, Y. Wen, Q. Zhang, H. N. Alshareef, and X.-X. Zhang, "Ultrathin Epitaxial Ferromagnetic  $\gamma$ -Fe<sub>2</sub>O<sub>3</sub> Layer as High Efficiency Spin Filtering Materials for Spintronics Device Based on Semiconductors", *Advanced Functional Materials* **26**, 5679–5689 (2016).
- <sup>124</sup>Y. J. Zeng, Z. Z. Ye, J. G. Lu, W. Z. Xu, L. P. Zhu, B. H. Zhao, and S. Limpijumnong, "Identification of acceptor states in Li-doped p-type ZnO thin films", *Applied Physics Letters* **89**, 042106 (2006).
- <sup>125</sup>C. Rauch, W. Gehlhoff, M. R. Wagner, E. Malguth, G. Callsen, R. Kirste, B. Salameh, A. Hoffmann, S. Polarz, Y. Aksu, and M. Driess, "Lithium related deep and shallow acceptors in Li-doped ZnO nanocrystals", *Journal of Applied Physics* **107**, 024311 (2010).

- <sup>126</sup>X. Guan, N. Cai, C. Yang, J. Chen, and P. Lu, "Magnetic properties of ZnO nanowires with Li dopants and Zn vacancies", *Thin Solid Films* **605**, 273–276 (2016).
- <sup>127</sup>M. Khalid and P. D. Esquinazi, "Hydrogen-induced ferromagnetism in ZnO single crystals investigated by magnetotransport", *Physical Review B* **85**, 134424 (2012).
- <sup>128</sup>H.-K. Chen, "Kinetic study on the carbothermic reduction of zinc oxide", *Scandinavian Journal of Metallurgy* **30**, 292–296 (2001).
- <sup>129</sup>M. Epstein, A. Yogev, C. Yao, and A. Berman, "Carbothermal reduction of alkali hydroxides using concentrated solar energy", *Energy* **26**, 441–455 (2001).
- <sup>130</sup>S. K. Cheung and N. W. Cheung, "Extraction of Schottky diode parameters from forward current-voltage characteristics", *Applied Physics Letters* **49**, 85–87 (1986).
- <sup>131</sup>F. Fabbri, M. Villani, A. Catellani, A. Calzolari, G. Cicero, D. Calestani, G. Calestani, A. Zappettini, B. Dierre, T. Sekiguchi, and G. Salviati, "Zn vacancy induced green luminescence on non-polar surfaces in ZnO nanostructures", *Scientific Reports* **4**, 5158 (2014).
- <sup>132</sup>T. S. Heng, D.-C. Qi, T. Berlijn, J. B. Yi, K. S. Yang, Y. Dai, Y. P. Feng, I. Santoso, C. Sánchez-Hanke, X. Y. Gao, A. T. S. Wee, W. Ku, J. Ding, and A. Rusydi, "Room-Temperature Ferromagnetism of Cu-Doped ZnO Films Probed by Soft X-Ray Magnetic Circular Dichroism", *Physical Review Letters* **105**, 207201 (2010).
- <sup>133</sup>P. D. Esquinazi, W. Hergert, D. Spemann, A. Setzer, and A. Ernst, "Defect-Induced Magnetism in Solids", *IEEE Transactions on Magnetism* **49**, 4668–4674 (2013).
- <sup>134</sup>S. B. Ogale, "Dilute Doping, Defects, and Ferromagnetism in Metal Oxide Systems", *Advanced Materials* **22**, 3125–3155 (2010).
- <sup>135</sup>M. Stoneham, "The strange magnetism of oxides and carbons", *Journal of Physics: Condensed Matter* **22**, 074211 (2010).
- <sup>136</sup>O. F. Schirmer, "O– bound small polarons in oxide materials", *Journal of Physics: Condensed Matter* **18**, R667 (2006).
- <sup>137</sup>I. Lorite, C. Zandalazini, P. D. Esquinazi, D. Spemann, S. Friedländer, A. Pöpl, T. Michalsky, M. Grundmann, J. Vogt, J. Meijer, S. P. Heluani, H. Ohldag, W. A. Adeagbo, S. K. Nayak, W. Hergert, A. Ernst, and M. Hoffmann, "Study of the negative magneto-resistance of single proton-implanted lithium-doped ZnO microwires", *Journal of Physics: Condensed Matter* **27**, 256002 (2015).
- <sup>138</sup>A. Goldenblum, V. Bogatu, T. Stoica, Y. Goldstein, and A. Many, "Weak localization effects in ZnO surface wells", *Physical Review B* **60**, 5832–5838 (1999).
- <sup>139</sup>T. Andrearczyk, J. Jaroszyński, G. Grabecki, T. Dietl, T. Fukumura, and M. Kawasaki, "Spin-related magnetoresistance of *n*-type ZnO:Al and Zn<sub>1-x</sub>Mn<sub>x</sub>O:Al thin films", *Physical Review B* **72**, 121309 (2005).
- <sup>140</sup>E. M. Likovich, K. J. Russell, E. W. Petersen, and V. Narayanamurti, "Weak localization and mobility in ZnO nanostructures", *Physical Review B* **80**, 245318 (2009).



- <sup>141</sup>D. Wang, J. Kim, M. Seo, V. Thuy, Y. Yoo, Y. Lee, and J. Rhee, "Magnetoresistance in ZnO induced by spin-splitting and weak localization", *Materials Chemistry and Physics* **134**, 74–79 (2012).
- <sup>142</sup>Y. J. Zeng, L. M. C. Pereira, M. Menghini, K. Temst, A. Vantomme, J.-P. Locquet, and C. Van Haesendonck, "Tuning Quantum Corrections and Magnetoresistance in ZnO Nanowires by Ion Implantation", *Nano Letters* **12**, 666–672 (2012).
- <sup>143</sup>A. Agrawal, T. A. Dar, and P. Sen, "Weak localization effect in pulsed laser deposited ZnO film", *Journal of Physics: Conference Series* **534**, 012042 (2014).
- <sup>144</sup>O. V. Reukova, V. G. Kytin, V. A. Kulbachinskii, L. I. Burova, A. R. Kaul, and A. G. Ulyashin, "Weak localization in ZnO:Ga and ZnO:Al thin films", *Journal of Physics: Conference Series* **568**, 052025 (2014).
- <sup>145</sup>E. D. Cobas, O. M. J. van 't Erve, S.-F. Cheng, J. C. Culbertson, G. G. Jernigan, K. Bussman, and B. T. Jonker, "Room-Temperature Spin Filtering in Metallic Ferromagnet–Multilayer Graphene–Ferromagnet Junctions", *ACS Nano* **10**, 10357–10365 (2016).



## Appendix A

# List of publications

### To be published

- **L. Botsch**, P. D. Esquinazi, “Modeling the Magnetic Percolation Process in Artificial Ferromagnets”, to be published (2021).  
**Contribution:** Computer simulations; Ion irradiation; SQUID measurements; Data analysis; Figures; Manuscript; Corresponding author
- **L. Botsch**, C. Bundesmann, D. Spemann, and P. D. Esquinazi, “Toward a systematic discovery of artificial functional magnetic materials”, to be published (2021),  
<http://arxiv.org/abs/2103.08045>.  
**Contribution:** Computer simulations; Ion irradiation; SQUID measurements; Data analysis; Figures; Manuscript; Corresponding author

### Peer reviewed publications

- **L. Botsch**, N. Raatz, S. Pezzagna, R. Staacke, R. John, B. Abel, P. D. Esquinazi, J. Meijer, and S. Diziain, “Vectorial calibration of superconducting magnets with a quantum magnetic sensor”, *Review of Scientific Instruments*, **91**, 125003 (2020). DOI: [10.1063/5.0023597](https://doi.org/10.1063/5.0023597)  
**Contribution:** part of measurement setup/programming; contributed to measurements; contributed to manuscript and proof reading
- P. D. Esquinazi, W. Hergert, M. Stiller, **L. Botsch**, H. Ohldag, D. Spemann, M. Hoffmann, W. Adeagbo, A. Chassé, S. K. Nayak, and H. Ben Hamed, “Defect induced magnetism in non-magnetic Oxides: Basic principles, experimental evidence and possible devices”, *Physica Status Solidi B*, **257**, 1900623 (2020). DOI: [10.1002/pssb.201900623](https://doi.org/10.1002/pssb.201900623)  
**Contribution:** Chapter on spin transport in ZnO
- **L. Botsch**, I. Lorite, Y. Kumar, P. D. Esquinazi, J. Zajadacz, and K. Zimmer, “All-Semiconducting Spin Filter Prepared by Low-Energy Proton Irradiation”, *ACS Applied Electronic Materials*, **1**, 1832-1841 (2019). DOI: [10.1021/acsaelm.9b00369](https://doi.org/10.1021/acsaelm.9b00369)  
**Contribution:** Sample preparation; E-beam lithography; Ion irradiation; Transport measurements; Data analysis; Theoretical model; Figures; Manuscript; Corresponding author
- A. Setzer, P. D. Esquinazi, **L. Botsch**, O. Baehre, E. Teblum, A. Itzhak, O. Girshevitz, and G. D. Nessim, “Magnetic phase transitions around

room temperature in Cu<sub>9</sub>S<sub>5</sub>", *Phase Transitions*, **92**, 385-395 (2019). DOI: [10.1080/01411594.2019.1586901](https://doi.org/10.1080/01411594.2019.1586901)

**Contribution:** Transport measurements; Data analysis; Figure; Section in manuscript

- **L. Botsch**, I. Lorite, Y. Kumar, and P. D. Esquinazi, "Indirect experimental evidence of a persistent spin helix in H<sup>+</sup> implanted Li-doped ZnO by photogalvanic spectroscopy", *Physical Review B*, **95**, 201405 (2017). DOI: [10.1103/PhysRevB.95.201405](https://doi.org/10.1103/PhysRevB.95.201405)

**Contribution:** Sample preparation; E-beam lithography; Ion irradiation; Photocurrent measurements; Data analysis; Figures; Manuscript; Corresponding author

## Patent

- **L. Botsch**, P. D. Esquinazi, "Verfahren zur Herstellung eines Elektronen Spin Filters und dessen Anwendung als Magnetfeldsensor" German Patent Office, [DE102017001492A1](https://patent.gov.de/DE102017001492A1) (2018)

**Contribution:** Patent description; Submission process

## Conference contributions

- **L. Botsch**, P. D. Esquinazi, "Toward a systematic discovery of artificial functional magnetic materials", IEEE Intermag Conference (2021).  
**Contribution:** Digest; Oral presentation (prerecorded video)
- S. Dietel, S. Diziain, R. Staacke, **L. Botsch**, B. Abel, J. Meijer, and P. D. Esquinazi, "Fabrication of diamond tips for optical magnetometry", DPG-Frühjahrstagung, Regensburg (2019).  
**Contribution:** E-beam lithography; Contributed poster section
- **L. Botsch**, I. Lorite, Y. Kumar, P. D. Esquinazi, T. Michalsky, J. Zajądacz, and K. Zimmer, "Defect induced magnetism - A framework for all-semiconductor spintronics", DPG-Frühjahrstagung, Berlin (2018).  
**Contribution:** Digest; Oral presentation
- **L. Botsch**, P. D. Esquinazi, I. Lorite, and Y. Kumar, "Defect induced magnetism in ZnO: a first spintronic device application", The European Conference Physics of Magnetism, Poznan (2017).  
**Contribution:** Digest; Oral presentation

## **Appendix B**

# **Computation inputs and codes**

## B.1 DFT electronic structure calculations - Fleur input files

The FLEUR code can be obtained at <http://www.flapw.de/MaX-5.0/>. The input files for the calculations described in Section 2.5.2 and Section 4.4 are reproduced in the following listings.

LISTING B.1: Fleur input file for  $3 \times 3 \times 1$  anatase  $\text{TiO}_2$  bulk system with one dFP defect

---

```

1 TiO2 (Anatase) Bulk dFP
2
3 &input film=f /
4   21.4550055696895647   0.0000000000000000
5   0.0000000000000000   21.4550055696895647
6   0.0000000000000000   0.0000000000000000
7   17.9794212790502890
8   1.0000000000000000
9   1.0000000000000000   1.0000000000000000
10  1.0000000000000000
11  108
12  22   0.9935630000000000   0.9983919999999998
13  22   0.9981830000000000
14  22   0.0027580000000000   0.3375349999999999
15  22   0.9925719999999999
16  22   0.0027560000000000   0.6593279999999999
17  22   0.9925680000000000
18  22   0.3422749999999999   0.9984809999999998
19  22   0.0007500000000000
20  22   0.3339500000000000   0.3399820000000000
21  22   0.0023570000000000
22  22   0.3339260000000000   0.6569780000000000
23  22   0.0023440000000000
24  22   0.6670860000000000   0.9984829999999999
25  22   0.0152790000000000
26  22   0.6611549999999998   0.3391279999999999
27  22   0.0040440000000000
28  22   0.6611339999999999   0.6578399999999999
29  22   0.0040530000000000
30  22   0.1689230000000000   0.1738310000000000
31  22   0.5015080000000000
32  22   0.2101400000000000   0.4984459999999999
33  22   0.4607229999999999
34  22   0.1689750000000000   0.8231139999999999
35  22   0.5014980000000000
36  22   0.4890050000000000   0.1843860000000000
37  22   0.5069180000000000
38  22   0.4890059999999999   0.8125689999999999
39  22   0.5069669999999999

```

---

25	22	0.8460110000000001 0.5060530000000000	0.1770870000000000
26	22	0.8313999999999999 0.4865570000000000	0.4984640000000000
27	22	0.8459779999999999 0.5060039999999999	0.8198029999999999
28	22	0.9873219999999999 0.2439470000000000	0.1770870000000000
29	22	0.0019330000000000 0.2634430000000000	0.4984640000000000
30	22	0.9873550000000000 0.2439960000000000	0.8198029999999999
31	22	0.3443280000000000 0.2430820000000000	0.1843860000000000
32	22	0.3443269999999999 0.2430330000000000	0.8125689999999999
33	22	0.6644110000000000 0.2484920000000000	0.1738310000000000
34	22	0.6231929999999999 0.2892770000000000	0.4984459999999999
35	22	0.6643580000000000 0.2485020000000000	0.8231139999999999
36	22	0.1662470000000000 0.7347210000000000	0.9984829999999999
37	22	0.1721790000000000 0.7459560000000000	0.3391279999999999
38	22	0.1722000000000000 0.7459470000000000	0.6578399999999999
39	22	0.4910579999999999 0.7492500000000000	0.9984809999999998
40	22	0.4993830000000000 0.7476429999999999	0.3399820000000000
41	22	0.4994080000000000 0.7476559999999999	0.6569780000000000
42	22	0.8397700000000000 0.7518169999999998	0.9983919999999998
43	22	0.8305750000000000 0.7574280000000000	0.3375349999999999
44	22	0.8305769999999999 0.7574320000000000	0.6593279999999999
45	8	0.9915410000000000 0.2165180000000000	0.9984129999999999
46	8	0.0026170000000000 0.2074610000000000	0.3334420000000000
47	8	0.0028170000000000 0.2074640000000000	0.6634539999999999
48	8	0.3412140000000000 0.2164730000000000	0.9984459999999998
49	8	0.3304980000000000 0.2029760000000000	0.3358890000000000

---

50	8	0.3304420000000000 0.2029810000000000	0.6610389999999998
51	8	0.6667520000000000 0.2171290000000000	0.9984559999999999
52	8	0.6543099999999999 0.2197810000000000	0.3357059999999999
53	8	0.6542399999999999 0.2198250000000000	0.6612149999999999
54	8	0.1593780000000000 0.7023309999999999	0.1657060000000000
55	8	0.1842170000000000 0.7029529999999999	0.4984640000000000
56	8	0.1594810000000000 0.7023190000000000	0.8312440000000000
57	8	0.4985370000000000 0.7092349999999999	0.1617710000000000
58	8	0.5011540000000000 0.7593099999999999	0.4984720000000000
59	8	0.4984910000000000 0.7092670000000000	0.8351489999999999
60	8	0.8430790000000000 0.7098769999999999	0.1649140000000000
61	8	0.8266979999999999 0.7120090000000000	0.4984300000000000
62	8	0.8430289999999999 0.7098479999999999	0.8319299999999999
63	8	0.0043030000000000 0.4528800000000000	0.1736710000000000
64	8	0.0044110000000000 0.4613099999999999	0.4985209999999999
65	8	0.0042990000000000 0.4529230000000000	0.8231900000000000
66	8	0.3293360000000000 0.4532659999999999	0.1687360000000000
67	8	0.3736390000000000 0.4252940000000000	0.4984310000000000
68	8	0.3293620000000000 0.4532530000000000	0.8283199999999999
69	8	0.6683639999999998 0.4736279999999999	0.1550750000000000
70	8	0.6652120000000000 0.4711150000000000	0.4982650000000000
71	8	0.6683479999999999 0.4735970000000000	0.8419289999999999
72	8	0.1650260000000000 0.9880869999999999	0.9984619999999998
73	8	0.1660820000000000 0.9544339999999999	0.3227210000000000
74	8	0.1660750000000000 0.9543890000000000	0.6742310000000000



---

75	8	0.5074570000000000 0.9558809999999999	0.9985119999999998
76	8	0.5000510000000000 0.9644149999999999	0.3181689999999999
77	8	0.5000409999999998 0.9644149999999999	0.6787960000000000
78	8	0.8277850000000000 0.9547970000000000	0.9983039999999999
79	8	0.8326989999999999 0.9632399999999999	0.3389170000000000
80	8	0.8327019999999999 0.9632680000000000	0.6579369999999999
81	8	0.1665810000000000 0.5328710000000000	0.9984559999999999
82	8	0.1790240000000000 0.5302190000000000	0.3357059999999999
83	8	0.1790930000000000 0.5301750000000001	0.6612149999999999
84	8	0.4921200000000000 0.5335270000000000	0.9984459999999998
85	8	0.5028349999999998 0.5470240000000000	0.3358890000000000
86	8	0.5028910000000000 0.5470189999999999	0.6610389999999998
87	8	0.8417929999999999 0.5334820000000000	0.9984129999999999
88	8	0.8307169999999999 0.5425390000000000	0.3334420000000000
89	8	0.8305159999999999 0.5425359999999999	0.6634539999999999
90	8	0.9902549999999999 0.0401230000000000	0.1649140000000000
91	8	0.0066350000000000 0.0379910000000000	0.4984300000000000
92	8	0.9903039999999999 0.0401520000000000	0.8319299999999999
93	8	0.3347959999999999 0.0407650000000000	0.1617710000000000
94	8	0.3321790000000000 0.9906900000000000	0.4984720000000000
95	8	0.3348420000000000 0.0407330000000000	0.8351489999999999
96	8	0.6739560000000000 0.0476690000000000	0.1657060000000000
97	8	0.6491160000000000 0.0470470000000000	0.4984640000000000
98	8	0.6738529999999999 0.0476810000000000	0.8312440000000000
99	8	0.1649690000000000 0.2763720000000000	0.1550750000000000

```

100  8    0.1681210000000000    0.4982650000000000
      0.2788850000000000
101  8    0.1649860000000000    0.8419289999999999
      0.2764030000000000
102  8    0.5039979999999999    0.1687360000000000
      0.2967340000000000
103  8    0.4596950000000000    0.4984310000000000
      0.3247060000000000
104  8    0.5039709999999998    0.8283199999999999
      0.2967469999999999
105  8    0.8290310000000000    0.1736710000000000
      0.2971199999999999
106  8    0.8289219999999998    0.4985209999999999
      0.2886900000000000
107  8    0.8290339999999999    0.8231900000000000
      0.2970769999999999
108  8    0.0055480000000000    0.9983039999999999
      0.7952030000000000
109  8    0.0006340000000000    0.3389170000000000
      0.7867600000000000
110  8    0.0006310000000000    0.6579369999999999
      0.7867320000000000
111  8    0.3258759999999999    0.9985119999999998
      0.7941190000000000
112  8    0.3332820000000000    0.3181689999999999
      0.7855850000000000
113  8    0.3332919999999999    0.6787960000000000
      0.7855850000000000
114  8    0.6683069999999999    0.9984619999999998
      0.7619120000000000
115  8    0.6672510000000000    0.3227210000000000
      0.7955659999999999
116  8    0.6672580000000000    0.6742310000000000
      0.7956110000000000
117  22   0.6637790000000000    0.9984909999999999
      0.5501039999999999
118  22   0.1695540000000000    0.9984909999999999
      0.1998960000000000
119
120 &end /

```

---

LISTING B.2: surface system with one dFP defect]Fleur input file for  $3 \times 3 \times 1$  anatase  $\text{TiO}_2$  [001] surface system with one dFP defect

---

```

1 TiO2 (Anatase) [001] Surface dFP
2
3 &input film=t /
4    21.4578401588783230    0.0000000000000000
      0.0000000000000000

```

```
5      0.0000000000000000    21.4578401588783230
      0.0000000000000000
6      0.0000000000000000    0.0000000000000000
      25.0499997644943520
7      1.0000000000000000
8      1.0000000000000000    1.0000000000000000
      1.0000000000000000
9
10     135
11  22      0.9928560000000000    0.9995249999999999
      3.4501364675638069
12  22      0.1682450000000000    0.1682900000000000
      -12.4233219332030949
13  22      0.9951080000000000    0.1740840000000000
      8.0292263245138482
14  22      0.1678120000000000    0.9989449999999999
      -8.0138205746586824
15  22      0.0008870000000000    0.9998389999999999
      -3.5344798167708595
16  22      0.0005210000000000    0.3358030000000000
      3.5414687667051532
17  22      0.1746160000000000    0.8309699999999999
      -12.4715181327499813
18  22      0.6650479999999999    0.1683560000000000
      7.9327838254205423
19  22      0.4932329999999999    0.9927389999999999
      -7.9781994749935707
20  22      0.1673620000000000    0.3351850000000000
      -8.0209097245920340
21  22      0.9945830000000000    0.8258850000000000
      8.0608394242166383
22  22      0.4934160000000000    0.1715160000000000
      -12.5117484323717605
23  22      0.6659429999999998    0.9989749999999998
      3.5640638664927287
24  22      0.3410000000000000    0.9988859999999999
      3.4670953174043690
25  22      0.8389689999999999    0.1737920000000000
      12.5194888822989867
26  22      0.8386789999999998    0.9990329999999998
      -7.8946577257789832
27  22      0.3389760000000000    0.1789810000000000
      8.0054288247375780
28  22      0.1713590000000000    0.5010199999999999
      12.4083921333434564
29  22      0.0003330000000000    0.6646040000000000
      3.5460278666622922
30  22      0.0060980000000000    0.5003960000000000
      8.0747171240861668
31  22      0.1678870000000000    0.6658800000000000
      -8.0293766245124338
```

32	22	0.0004060000000000 -3.5463785666589933	0.3337570000000000
33	22	0.6655869999999999 -3.5056222170421623	0.9996950000000000
34	22	0.3334610000000000 -3.5442743666787777	0.9997129999999999
35	22	0.0004320000000000 -3.5528665165979989	0.6663929999999999
36	22	0.3335360000000000 3.6371848158052860	0.3384430000000000
37	22	0.8357289999999998 12.4916833825603977	0.8258659999999999
38	22	0.6606919999999999 8.0656991241709513	0.5008710000000000
39	22	0.4993909999999999 -8.1242660236203363	0.6698890000000000
40	22	0.8331280000000000 -7.9944569248407271	0.3354150000000000
41	22	0.3435859999999999 8.1359894235101216	0.8225129999999999
42	22	0.4960290000000000 12.4498498829536945	0.5052720000000001
43	22	0.6660539999999998 3.5651159664828356	0.6658919999999999
44	22	0.6593940000000000 8.0415008243984474	0.8309690000000001
45	22	0.4995450000000000 -8.0349627744599150	0.3361620000000000
46	22	0.3336209999999999 3.6456517157256836	0.6624510000000000
47	22	0.8328109999999999 12.4759018827087669	0.5008340000000000
48	22	0.6659410000000000 3.5547703165801017	0.3350200000000000
49	22	0.8326290000000000 -8.0020220247696052	0.6653969999999999
50	22	0.3335100000000000 -3.5493595166309704	0.3338090000000000
51	22	0.6655820000000000 -3.5631871165009708	0.6660489999999999
52	22	0.3339850000000000 -3.5620348165118036	0.6664649999999999
53	22	0.6661019999999999 -3.5508124166173101	0.3342149999999999
54	8	0.9985149999999999 7.3454114309426801	0.0003550000000000
55	8	0.1664830000000000 -8.7331062678963729	0.1662160000000000
56	8	0.9990990000000000 11.8368262887169848	0.1661140000000000

---

57	8	0.1661770000000000 -4.1856796106486538	0.0000720000000000
58	8	0.1659690000000000 -11.8657840884447427	0.0016550000000000
59	8	0.0007840000000000 4.2011104105035821	0.1645670000000000
60	8	0.1654750000000000 8.6779962684144873	0.1637170000000000
61	8	0.9998769999999999 -2.6414222751668706	0.1662740000000000
62	8	0.9989889999999999 -7.3288283310985838	0.0001380000000000
63	8	0.9998329999999999 7.3222652311602863	0.3298079999999999
64	8	0.1662460000000000 -8.7129159680861896	0.8343880000000000
65	8	0.6676340000000001 11.8959693381609597	0.1639760000000000
66	8	0.5011350000000000 -4.1786906607143610	0.0002970000000000
67	8	0.1663170000000000 -11.8486999886053574	0.3306769999999999
68	8	0.0007890000000000 4.1929441105803615	0.8357069999999999
69	8	0.5014700000000000 8.7285471679392366	0.1660360000000000
70	8	0.8338210000000000 8.7350100678784734	0.1660800000000000
71	8	0.8327269999999999 -4.1997827605160669	0.0000590000000000
72	8	0.3327440000000000 11.8488252386041797	0.1662320000000000
73	8	0.1662630000000000 -8.6951054182536343	0.4993609999999999
74	8	0.9999070000000000 7.3168544312111532	0.6694919999999999
75	8	0.9999619999999999 4.1705744607906663	0.4997520000000000
76	8	0.1661610000000000 -11.8380036387059189	0.6675309999999999
77	8	0.9998730000000000 -2.6414473251666362	0.8339759999999999
78	8	0.6679029999999999 -7.4085374303492051	0.0005110000000000
79	8	0.3327260000000000 -7.3154516312243434	0.0004150000000000
80	8	0.9999290000000000 -2.6412469251685198	0.4997559999999999
81	8	0.3331789999999999 7.3254215311306137	0.0007080000000000

82	8	0.8324570000000000 -8.7468086177675524	0.1651140000000000
83	8	0.9978279999999999 11.8731487883755058	0.4998349999999999
84	8	0.1661350000000000 -4.1749081107499233	0.6667319999999999
85	8	0.8340520000000000 -11.8729483883773881	0.0010320000000000
86	8	0.3323079999999999 4.1743820607548683	0.1634200000000000
87	8	0.1617420000000000 8.7282465679420600	0.4998430000000000
88	8	0.6667609999999998 4.1899631606083858	0.1658990000000000
89	8	0.5032019999999999 -11.8678632384251959	0.0018120000000000
90	8	0.5009569999999999 -8.7279209179451236	0.1663830000000000
91	8	0.6671230000000000 7.3297301310901055	0.0013530000000000
92	8	0.1663160000000000 -4.1809952606926943	0.3332010000000000
93	8	0.9988740000000000 11.8249024888290908	0.8340580000000000
94	8	0.1642080000000000 8.6467839687079255	0.8367489999999999
95	8	0.3333100000000000 -2.6397439251826502	0.1664320000000000
96	8	0.9994230000000000 -7.3160277812189278	0.6668170000000000
97	8	0.6667940000000000 -2.6434513251477956	0.1656830000000000
98	8	0.9994380000000000 -7.3204866811770071	0.3330509999999999
99	8	0.3331250000000000 7.3157021312219870	0.3274610000000000
100	8	0.8327469999999999 -8.7334569678930762	0.8353340000000000
101	8	0.6695280000000000 11.8716958883891639	0.4995450000000000
102	8	0.5003760000000000 -4.1603540608867515	0.6665969999999999
103	8	0.8331840000000000 -11.8547620885483660	0.3303020000000000
104	8	0.3321130000000000 4.1557198109303179	0.8372049999999999
105	8	0.5045550000000000 8.7086574681262245	0.4998460000000000
106	8	0.6669560000000000 4.1677438108172762	0.8345910000000000

---

107	8	0.5005059999999999 -11.843389388652859	0.3298230000000000
108	8	0.8336420000000000 8.7351102678775323	0.4998589999999999
109	8	0.5010930000000000 -8.6789231184057716	0.8368459999999999
110	8	0.6670519999999999 7.3206870811751230	0.3307520000000000
111	8	0.8335339999999999 -4.1798680107032915	0.6667570000000000
112	8	0.3323680000000000 11.8897068382198352	0.5000570000000000
113	8	0.5003110000000000 -8.6787477684074208	0.4974630000000000
114	8	0.6671039999999999 7.3078113812961742	0.6677459999999998
115	8	0.8333719999999999 -4.1851285106538363	0.3331940000000000
116	8	0.3274210000000000 11.8323924387586707	0.8337459999999999
117	8	0.6666879999999999 4.1645624608471872	0.4995930000000000
118	8	0.5000969999999999 -11.8318162887640881	0.6640750000000000
119	8	0.8352999999999999 8.7157716680593413	0.8339240000000000
120	8	0.8333969999999998 -11.8470717386206665	0.6683850000000000
121	8	0.3333650000000000 4.1354293111210794	0.4995599999999999
122	8	0.5019239999999999 8.6738379684535811	0.8337749999999999
123	8	0.3330629999999999 7.2953865814129841	0.6703740000000000
124	8	0.8334009999999999 -8.7135171680805392	0.4994669999999999
125	8	0.6691800000000000 11.9065654880613376	0.8373269999999998
126	8	0.5003490000000000 -4.1775133107254296	0.3331509999999999
127	8	0.3332670000000000 -2.6394182751857134	0.8340040000000000
128	8	0.6683200000000000 -7.3070598813032390	0.6666460000000000
129	8	0.6668400000000000 -2.6430505251515641	0.8347730000000000
130	8	0.3322630000000000 -7.3039787313322062	0.6665890000000000
131	8	0.6667770000000000 -2.6414222751668706	0.4995650000000000

```
132 8 0.3329889999999999 0.3330130000000000
    -7.3135728812420071
133 8 0.3332660000000000 0.4995729999999999
    -2.6419733751616898
134 8 0.6675990000000001 0.3329589999999999
    -7.3162532312168080
135 8 0.8349169999999999 0.0001250000000000
    2.6466326751178855
136 8 0.4995339999999999 0.0001590000000000
    2.6467328751169452
137 8 0.1660350000000000 0.0001360000000000
    2.7448036241949367
138 8 0.1648010000000000 0.6670610000000000
    2.6386417251930099
139 8 0.5013159999999999 0.6668400000000000
    2.6376898252019627
140 8 0.8339330000000000 0.6669320000000001
    2.6375395252033749
141 8 0.8337859999999999 0.3329469999999999
    2.6381908251972521
142 8 0.5014370000000000 0.3330469999999999
    2.6370635752078497
143 8 0.1648150000000000 0.3328420000000000
    2.6377399252014913
144 22 0.6594169999999999 0.9942959999999998
    -11.4595983422634671
145 22 0.1679370000000000 0.9993549999999999
    6.9093660850421275
146 &end /
```

---



## B.2 Magnetic Percolation simulations

The code used for the magnetic percolation simulations described in Section 2.4 was written in C++ and can be found at <https://github.com/lbotsch/magnetic-percolation-simulation>. Instructions for building the code are given in the README file.

The “sim” program can be used to simulate a magnetic percolation process on a random lattice and collect statistical data. The following command illustrates the usage of the simulation code

---

```
1 ./sim 200 5 200 10 > results.csv
```

---

for a  $200 \times 200 \times 5$  cubic lattice, averaging over 10 random lattice configurations for each of 200 defect probabilities sampled uniformly from the range  $[0, 1]$ . The command will produce a file “results.csv” similar to the following

---

```
1 Defect Probability ,Domain Count (AVG) ,Domain Count (
  STD) ,Max Domain Size (AVG) ,Max Domain Size (STD) ,
  Mean Domain Size (AVG) ,Mean Domain Size (STD)
2 0.005 ,988.6 ,2.8 ,2.3 ,0.42 ,1.01154 ,0.00286393
3 0.01 ,1944.2 ,6.64 ,3.2 ,0.32 ,1.02872 ,0.00350676
4 0.015 ,2873.6 ,11.88 ,3.6 ,0.6 ,1.04401 ,0.00431781
5 0.02 ,3771.7 ,14.36 ,3.9 ,0.36 ,1.06055 ,0.00404553
6 0.025 ,4637.1 ,18.3 ,4.8 ,0.64 ,1.07829 ,0.00426255
7 0.03 ,5476.4 ,23 ,5.1 ,0.36 ,1.09564 ,0.00460043
8 0.035 ,6272.5 ,25.5 ,5.7 ,0.9 ,1.116 ,0.00453779
9 0.04 ,7051.4 ,29.2 ,6.2 ,0.88 ,1.13455 ,0.00469889
10 ...
```

---

listing the mean and standard deviation of “domain count”, “max domain size” and “mean domain size” at each of the 200 defect probabilities.

The “vis” program can be used to create visualizations of the resulting domains (such as those shown in Figure 2.3 (c-e)). The following command

---

```
2 ./vis 200 1 200 domains sc domains_200x200x1
```

---

will produce images of a  $200 \times 200 \times 1$  cubic lattice with percolation domains randomly colorized for 200 defect probabilities uniformly sampled from the range  $[0, 1]$ . The colors are persistent across the images, so that they can be combined to a video showing the evolution of the percolation process as the defect probability increases from 0 to 1.

### B.3 SQUID raw data analysis code

The code used to read and analyze raw SQUID scan data as produced by the Quantum Design MPMS was written in the Julia programming language (see <https://julialang.org/>) and can be found at <https://github.com/lbotsch/SquidData.jl>. The Julia package SquidData.jl includes functions for reading and fitting the raw data, as well as post-processing algorithms for specific measurements (e.g. processing hysteresis loop measurements).

## **B.4 SRIM Monte Carlo binary collision code automation**

The code used to automate and process SRIM Monte Carlo simulations to produce the final magnetic phase diagrams (see Section 2.5) was written in the Python programming language and can be found at <https://github.com/lbotsch/auto-srim>.